

ISTANBUL TECHNICAL UNIVERSITY ★ GRADUATE SCHOOL

**DEVELOPMENT OF AN EARLY INDICATOR INDEX FOR TORNADIC
STORMS IN THE EURO-MEDITERRANEAN REGION**



M.Sc. THESIS

Ömer Kutay MIHLIARDIÇ

Department of Meteorological Engineering

Atmospheric Sciences Programme

FEBRUARY 2023

ISTANBUL TECHNICAL UNIVERSITY ★ GRADUATE SCHOOL

**DEVELOPMENT OF AN EARLY INDICATOR INDEX FOR TORNADIC
STORMS IN THE EURO-MEDITERRANEAN REGION**

M.Sc. THESIS

**Ömer Kutay MIHLIARDIÇ
(511191018)**

Department of Meteorological Engineering

Atmospheric Sciences Programme

Thesis Advisor: Sevinç ASİLHAN SİRDAŞ

FEBRUARY 2023

İSTANBUL TEKNİK ÜNİVERSİTESİ ★ LİSANSÜSTÜ EĞİTİM ENSTİTÜSÜ

**AVRUPA-AKDENİZ BÖLGESİ'NDEKİ TORNADİK FIRTINALAR İÇİN
ERKEN GÖSTERGE ENDEKSİNİN GELİŞTİRİLMESİ**

YÜKSEK LİSANS TEZİ

**Ömer Kutay MIHLIARDIÇ
(511191018)**

Meteoroloji Mühendisliği Anabilim Dalı

Atmosfer Bilimleri Programı

Tez Danışmanı: Sevinç ASİLHAN SİRDAŞ

ŞUBAT 2023

Ömer Kutay MIHLIARDIÇ, a M.Sc. student of İTÜ Graduate School student ID 511191018, successfully defended the thesis/dissertation entitled “DEVELOPMENT OF AN EARLY INDICATOR INDEX FOR TORNADIC STORMS IN THE EURO-MEDITERRANEAN REGION”, which he prepared after fulfilling the requirements specified in the associated legislations, before the jury whose signatures are below.

Thesis Advisor : **Prof. Dr. Sevinç ASİLHAN SIRDAŞ**
Istanbul Technical University

Jury Members : **Prof. Dr. Şükran Sibel MENTEŞ**
Istanbul Technical University

Prof. Dr. Zafer ASLAN
Istanbul Aydın University

Date of Submission : 28 December 2022
Date of Defense : 24 February 2023





To my family,



FOREWORD

First of all, I would like to express my greatest gratitude to my supervisor Prof. Dr. Sevinc Asilhan Sirdas for her guidance, support, reviews, and recommendations through the work of this thesis. I would like to thank all professors during my bachelor and master studies in the department of Meteorological Engineering at Istanbul Technical University. They have been great pathfinder and motivating mentors to me which I feel extremely lucky for. I could not have achieved my current level of success without them. In addition, I am deeply thankful for Dr. Micha Gryschka who has been guiding me every step of the work for accepting me as a working research student at the Institute of Meteorology and Climatology of Leibniz University Hannover and providing me a excellent environment. I am also grateful to him for that he introduced me to the Meteorology research group at the Leibniz University Hannover. It has been a pleasure to work with them. Besides, I would like to thank my friends especially Serkan Kaya, M. Mesut Bozok and Ozgen Kilic for continued support and love along this path. Finally, my sincere and heartfelt gratitude to my family for supporting me throughout my studies and decisions as well as my health problems that accompanied me during the writing of the thesis.

December 2022

Omer Kutay MIHLIARDIC
(Meteorological Engineer)

TABLE OF CONTENTS

| | <u>Page</u> |
|--------------------------------------------------------------------------------------------------------------------------------|--------------|
| FOREWORD | ix |
| TABLE OF CONTENTS | xi |
| ABBREVIATIONS | xiii |
| SYMBOLS | xv |
| LIST OF TABLES | xvii |
| LIST OF FIGURES | xix |
| SUMMARY | xxvii |
| ÖZET | xxxii |
| 1. INTRODUCTION | 1 |
| 1.1 Purpose of Thesis | 2 |
| 1.2 Literature Review | 4 |
| 1.2.1 Research on severe convective storms and related hazards: A brief history | 4 |
| 1.2.2 Types of atmospheric fronts (frontogenesis) & air masses | 5 |
| 1.1.1.1 Cold & warm fronts | 8 |
| 1.1.1.2 Stationary fronts | 12 |
| 1.1.1.3 Occluded fronts | 13 |
| 1.2.3 Inclination of fronts & margules model | 16 |
| 1.1.1.4 Cross-frontal circulations and Q-vector | 19 |
| 1.2.4 Assessment of mesoscale convective systems including supercell tornadic storms & connection with weather fronts | 23 |
| 1.2.5 Characteristics, types and severity of tornadoes | 30 |
| 1.2.6 Formation tornado vortex: tornadogenesis | 32 |
| 1.2.7 Synoptic climatology of the tornadoes in Euro-Mediterranean in particular | 33 |
| 1.2.8 Current understanding of environmental conditions and dynamics of severe convective storms & tornadoes | 39 |
| 1.2.9 SCSs, tornadoes, and their associations with climate change | 44 |
| 1.3 Hypothesis & Necessity of EMEDO Index..... | 47 |
| 2. MATERIAL AND METHODOLOGY | 49 |
| 2.1 Study Area..... | 49 |
| 2.2 Data | 50 |
| 2.3 Methods | 52 |
| 2.3.1 Description of EMEDO index (EMEDO _i)..... | 52 |
| 2.3.1.1 Variations of EMEDO _i | 54 |
| 2.3.1.2 Positive phase..... | 54 |
| 2.3.1.3 Negative phase | 57 |
| 2.3.2 Frontogenesis | 60 |
| 3. RESULTS AND DISCUSSION | 61 |
| 3.1 Assessment of Recent Climatology and Synoptic Outlook | 61 |

| | |
|----------------------------------------------------------------------------------------------------------------------------|------------|
| 3.2 Analysis of Imminent Tornadic Storm Environment in the Scope EMEDO _i & Fronts in Eastern Mediterranean..... | 64 |
| 3.3 Analysis of Statistics | 94 |
| 3.4 Verification..... | 100 |
| 4. CONCLUSION..... | 105 |
| REFERENCES | 111 |
| APPENDICES | 115 |
| Appendix | 115 |
| Appendix A | 116 |
| Appendix B..... | 124 |
| Appendix C..... | 125 |
| CURRICULUM VITAE..... | 127 |



ABBREVIATIONS

| | |
|----------------|------------------------------------------------------------------|
| APAC | : Asia & Pacific |
| AR | : Atlantic Ridge |
| BLO | : Blocking |
| BWD | : Bulk Wind Shear |
| CAPE | : Convective Available Potential Energy |
| EF | : Enhanced Fujita Scale |
| EHI | : Energy Helicity Index |
| EMEA | : Europe, Middle East & Africa |
| EMEDO | : Eastern Mediterranean Oscillation |
| ENSO | : El Niño–Southern Oscillation |
| FFD | : Forward Flank Downdraft |
| FPP | : Fujita–Pearson Scale |
| GDAS | : Global Data Assimilation System |
| GFS | : Global Forecast System |
| LCL | : Lifting Condensation Level |
| LFC | : Level of Free Convection |
| MCC | : Mesoscale Convective Complex |
| MCS | : Mesoscale Convective System |
| MO | : Mediterranean Oscillation |
| NCEP | : National Center for Environmental Prediction |
| NWS | : National Weather Service |
| NAO | : North Atlantic Oscillation |
| NWS | : National Weather Service |
| RFD | : Rear Flank Downdraft |
| RM | : Right Moving Supercell |
| SCP | : Supercell Composite Parameter |
| SCS | : Severe Convective Storm |
| SPC | : Storm Prediction Center |
| SRH | : Storm Relative Helicity |
| STP | : Significant Tornado Parameter |
| TS | : Thunderstorm |
| QG | : Quasigeostrophic |
| ULL | : Upper Level Low |
| WeMO | : The Western Mediterranean Oscillation |
| WRF-ARW | : Weather and Research Forecasting – Advanced Research WRF Model |



SYMBOLS

| | |
|--------------|-------------------------------------|
| dBZ | : Decibel Radar Reflectivity Factor |
| F | : Frontogenesis |
| gpdam | : Geopotential Decameters |
| h | : Hour |
| hPa | : Hectopascal |
| K | : Kelvin |
| km | : Kilometer |
| m | : Meter |
| mb | : Milibar |
| Pa | : Pascal |
| s | : Second |
| UTC | : Universal Time Coordinated |
| Z | : Geopotential Height |
| λ | : Longitude |
| ϕ | : Latitude |
| Φ | : Geopotential |



LIST OF TABLES

| | <u>Page</u> |
|-----------------------------------------------------------------------------------------------------------------------------------------------------------------------------------------------------------------------------------------------------------------------------------------------------------------------------------------------------------------------------------------------------------------------------------------------------------------------------------------------------------------------------------------------------|-------------|
| Table 1.1 : A comparison of the Fujita scale with the enhanced Fujita scale (SPC 2009; SPC 2021)..... | 31 |
| Table 2.1 : Geospatial Points (Locations)..... | 49 |
| Table 2.2 : Description of model configuration and utilized data..... | 51 |
| Table 2.3 : Selected tornado/waterspout events for training in Turkiye and their features (ESWD, 2021)..... | 51 |
| Table 2.4 : Selected tornado/waterspout events for stability test in Turkiye and their features (ESWD, 2021)..... | 52 |
| Table 3.1 : Performance statistics of tendency metrics for the differences of EMEDO indices in Turkiye during the period of tornadic storm event. | 97 |
| Table 3.2 : Performance statistics of accuracy metrics according to the EMEDO-Oper=-0.75 during the period of tornadic storm (including local minimum time & tornado time) for all events in Turkiye. Values indicate Mean Bias Error (MBE), Mean Absolute Error (MAE), Mean Squared Error (MSE), Root Mean Square Error (RMSE), Root Mean Square Logarithmic Error (RMSLE), Mean Percentage Error (MPE), and Mean Absolute Percentage Error (MAPE), which are statistically significant positive correlations at 95% confidence level. | 99 |
| Table 3.3 : Correlation statistics of cumulative minimum of EMEDO-Oper indices during the period of tornadic storm (including local minimum time & tornado time) for all events in Turkiye. Values indicate Correlation coefficient (CC), Coefficient of Determination (CD), adjusted version of Coefficient of Determination (CD _{adj}), which are statistically significant positive correlations at 95% confidence level. | 100 |
| Table B. 1 : Selected hail event in Turkiye and its features (ESWD, 2021) | 124 |



LIST OF FIGURES

| | <u>Page</u> |
|------------------------------------------------------------------------------------------------------------------------------------------------------------------------------------------------------------------------------------------------------------------------------------------------------------------------------------------------------------------------------------------------------------------------------------------------------------------------------------------------------------------------------------------------------------------------------|-------------|
| Figure 1.1 : Number of SCS events that caused at least USD500 million insured loss. Europe, Middle East & Africa (EMEA) indicates Europe, Middle East & Africa continents and Asia & Pacific (APAC) represents Asia & Pacific regions (AON, 2021). | 2 |
| Figure 1.2 : A tornado forecast by Cassandra Forecasting Model valid for August 3, 2022, 11:00 UTC (WeatherX, 2022). | 3 |
| Figure 1.3 : Common pressure patterns and fronts in USA and air masses classification in accordance with region (NOAA, 2021). | 6 |
| Figure 1.4 : Four main types of weather fronts and their demonstrations for a weather map (Mentes, 2020). | 7 |
| Figure 1.5 : 3-D Schematics of the warm and cold fronts (Mentes, 2020). | 9 |
| Figure 1.6 : a) indicates a planar view looking down on the system while part b) indicates a vertical cross section (Holton, 2004). | 10 |
| Figure 1.7 : Vertical profile of the fronts (Ahrens, 2001). | 11 |
| Figure 1.8 : The idealized life cycle of a wave cyclone in six steps by Norwegian Cyclone Model. (a) Stationary (b) Frontal Wave (c) Open Wave (d) Mature (Initial Occlusion) (e) Advanced Occlusion (f) Cut-off cyclone (Ahrens, 2001). | 12 |
| Figure 1.9 : The depiction of stationary fronts (Mentes, 2020). | 13 |
| Figure 1.10 : Cross sectional views of warm-occluded (left) and cold-occluded (right) (Lackmann, 2011). | 14 |
| Figure 1.11 : Cross sectional view of the cold-occluded front (Mentes, 2020). | 15 |
| Figure 1.12 : Idealized depiction of a coastal front along a north– south-oriented coastline. Green dashed arrows indicate the near-surface flow associated with a land-breeze circulation; black solid arrows represent a synoptic-scale northeasterly flow (left). North–south cross section through an upper-level jet-front system, based on a short-term NAM forecast valid 18 UTC 25 Aug 2004. PV (shaded as in legend at bottom of panel), isentropes (black solid contours every 5K), and isotachs (red contours every 20 kt) (right) (Lackmann, 2011). | 16 |
| Figure 1.13 : Idealized horizontal plot of near-surface wind vectors (black arrows), isotherms (red dashed contours), and frontal zones for (a) initial time, and (b) the same front-relative view at a later time (24 h later). The rotated front-relative coordinate axes are shown. | 16 |
| Figure 1.14 : Diagnostic summary for 0000 UTC 17 Nov 2009, based on North American Mesoscale (NAM) analysis: (a) sea level pressure and subjective frontal analysis, bold line shows orientation of cross section shown in (d); (d) cross section of wind and potential temperature (interval 5K, red contours); orientation shown in (a) (Lackmann, 2011). | 17 |

| | |
|-------------------------------------------------------------------------------------------------------------------------------------------------------------------------------------------------------------------------------------------------------------------------------------------------------------------------------------------------------------------------------------------------------------------------------------------------------------------|----|
| Figure 1.15 : Frontal structure as depicted by a front analyzed for 0200 UTC April 26, 1979: (a) Surface temperature (8C, dashed), relative vorticity (contour interval $2 \times 10^{-5} \text{ s}^{-1}$, solid). Radar echoes at 0235 UTC April 26, 1979 are shaded. (c) Transverse circulation relative to the movement of the front (Adapted after Ogura and Poris 1982). | 17 |
| Figure 1.16 : Idealized cross-sectional diagrams demonstrating frontogenetical tilting. Dashed lines are isentropes and red arrows represent vertical motion for (a) an initial time and (b) a later time (Lin, 2007). | 18 |
| Figure 1.17 : Typical inclination of atmospheric cold (top) and warm (bottom) fronts (Penn State, n.d.). | 19 |
| Figure 1.18 : Schematic cross section of isentropes (dashed sloped lines) and ageostrophic circulation (thick arrows) (Lackmann, 2011). | 19 |
| Figure 1.19 : Idealized comparison of (a),(b) quasigeostrophic frontogenesis with (c),(d) semigeostrophic frontogenesis. Green arrows show primary geostrophic flow, red arrows represent ageostrophic frontal circulation, and dashed black lines are isentropes. Adapted from Bluestein (1986). Warm air mass (left), cold air mass (right) (Lackmann, 2011). | 20 |
| Figure 1.20 : Diagnosis of North Pacific front with GFS analysis valid 1200 UTC 14 Nov 2008: (a) 10-m wind barbs, 1000-mb isentropes (red, interval is 2 K); (d) as in (a), but with 850-mb omega (contour interval is $2 \times 10^{-2} \text{ Pa s}^{-1}$, dashed for ascent, solid for descent, and shaded as in legend). | 21 |
| Figure 1.21 : Vertical view of Q-Vector in Frontogenesis (Steenburgh, n.d.). | 22 |
| Figure 1.22 : Q-Vector Analysis on upper level systems (top) and surface systems (bottom) (Bluestein, 1993). | 22 |
| Figure 1.23 : Examples of near-surface horizontal frontogenesis function (shear and confluence terms): (a) sea level pressure, subjectively analyzed fronts, and frontogenesis (shaded as in legend, beginning at $3 \text{ K (100 km)}^{-1} (3 \text{ h})^{-1}$) (c) 10-m wind (barbs) and 1000-mb potential temperature and frontogenesis (shaded as in legend) from Global Forecast System (GFS) analysis valid 0000 UTC 14 Nov 2008 (Lackmann, 2011). | 23 |
| Figure 1.24 : Normalized losses from thunderstorms have increased in Europe (WMO, 2021). | 24 |
| Figure 1.25 : Determining thunderstorm classification (Commonwealth of Australia, Bureau of Meteorology, n.d.). | 25 |
| Figure 1.26 : Mesoscale radar signatures of storm cells (Schumacher & Rasmussen, 2020). | 26 |
| Figure 1.27 : Typical horizontal pattern of a bow echo (Goulet, 2015). | 27 |
| Figure 1.28 : Typical supercell structure (top) (Stull, 2015). Tornado location in near-fronts and typical supercell (bottom left), radar reflectivity data relation with supercell and fronts (bottom right) (Weingart, 2016). | 28 |
| Figure 1.29 : Radar Detection of a mesocyclone by reflectivity data (dBZ) dragging by supercell storm (top) and velocity data retrieved through radar sight line (bottom left/right) (Watch Chris Chase, 2019). | 29 |
| Figure 1.30 : Tornado rating classifications of NOAA's SPC and are used by the NWS. | 31 |
| Figure 1.31 : A visible mesocyclone and a F3 tornado in Alabama, US (Sutter, 2017). | 32 |
| Figure 1.32 : Kernel smoothed ESWD tornado reports per 100 years and 10,000 km ² based on (a) all recorded tornadoes, (b) tornadoes recorded in the period 2005–2019 (Grieser & Haines, 2021). | 34 |

| | |
|--------------------------------------------------------------------------------------------------------------------------------------------------------------------------------------------------------------------------------------------------------------------------------------------------------------------------------------------------------------------------------------------------------------------------------------------------------------------------------------|-----------|
| Figure 1.33 : Month of maximum number of tornado days (Groenemeijer & Kühne, 2014)..... | 34 |
| Figure 1.34 : Mid-Latitude Cyclogenesis Regions. The five primary zones of cyclogenesis are (1) the Atlas Mountains, (2) the Eastern Mediterranean, (3) the western Black Sea, (4) the southern Caspian Sea, and (5) the Western Mediterranean (Walters et al. 1991). Primary (short, solid arrow) and Secondary (dashed arrow) Mid-Latitude Storm Tracks: December, January, and February (left bottom). March, April, and May (middle bottom). November (bottom right)..... | 36 |
| Figure 1.35 : Typical paths of cyclones and their directions over Turkiye (green arrows), and locations of upper level low (blue contour) and through (red contour) for weather phase categories. Turkiye is shaded as light green (Kahraman, 2020). | 37 |
| Figure 1.36 : Major convective storm events in 2019 (ESWD, 2021)..... | 38 |
| Figure 1.37 : A tornado incident on January 26, 2019, Antalya Airport, Turkiye.... | 39 |
| Figure 1.38 : Typical hodograph and the motion of the mean wind represents possible supercell storm, the left- and right-moving storms plotted on it as well a shaded area corresponding to 0-3 km storm-relative helicity for a right-moving storm (ESTOFEX, n.d.) | 40 |
| Figure 1.39 : A supercell forecast based on Supercell Composite Parameter (SCP) valid for July 27, 2017, 15 UTC..... | 42 |
| Figure 1.40 : Composite parameter thresholds for hail and tornado events in Turkiye: (a) EHI for the 0–3-km layer, (b) EHI for the 0–1-km layer, (c) SCP, and (d) STP (Kahraman et al. 2017)..... | 43 |
| Figure 1.41 : Mid and long-term change of annual mean surface temperature according to different SSP scenarios (IPCC, 2021). | 45 |
| Figure 1.42 : Changes in extratropical storm track density in Northern Hemisphere (left) and Southern Hemisphere (right) (IPCC, 2021)..... | 46 |
| Figure 1.43 : (c) changes in average number of days with SupERHI for 2060– 2079, (d) changes in average number of days with SupERHI for 2080. SupERHI indicates Supercell environment with convective rain and high instability (Kahraman et al. 2020). | 47 |
| Figure 2.1 : Representation of oscillation points in analysis domain over Eastern Mediterranean Basin (Inclined Satellite Projection). | 50 |
| Figure 2.2 : Representation of oscillation points in analysis domain (Lambert Projection) and pressure placements indicates positive EMEDO index (left) and negative EMEDO index (right)..... | 52 |
| Figure 2.3 : Geopotential height [gpdam] at 300 hPa (isohypses) and geopotential height [gpdam] difference between 500hPa and 1000hPa (shaded color contours) - 27.01.2016 – 12 UTC..... | 56 |
| Figure 2.4 : Geopotential height [gpdam] at 300 hPa (isohypses) and geopotential height [gpdam] difference between 500hPa and 1000hPa (shaded color contours) - 16.02.2017 – 18 UTC..... | 56 |
| Figure 2.5 : Geopotential height [gpdam] at 300 hPa (isohypses) and geopotential height [gpdam] difference between 500hPa and 1000hPa (shaded color contours) - 21.03.2020 – 00 UTC..... | 57 |
| Figure 2.6 : Geopotential height [gpdam] at 300 hPa (isohypses) and geopotential height [gpdam] difference between 500hPa and 1000hPa (shaded color contours) - 21.04.2017 – 12.00 UTC..... | 58 |

Figure 2.7 : Geopotential height [gpdam] at 300 hPa (isohypses) and geopotential height [gpdam] difference between 500hPa and 1000hPa (shaded color contours) - 23.03.2018 – 18 UTC. **59**

Figure 2.8 : Geopotential height [gpdam] at 300 hPa (isohypses) and geopotential height [gpdam] difference between 500hPa and 1000hPa (shaded color contours) - 22.03.2021 – 18 UTC. **59**

Figure 3.1 : Diagrams depict the Euro-Atlantic sector around which the regime definitions of geographical patterns of Euro-Atlantic climatological regimes (both anomalies and full fields) as used at ECMWF. North Atlantic Oscillation, positive phase (NAO+), North Atlantic Oscillation, negative phase (NAO–), Blocking (BLO+), The Atlantic Ridge (AR) circulation pattern is a particular case of Anti-blocking (BLO–), in which the important feature is the trough over Scandinavia. Geopotential anomalies (color shading) and geopotential (contours) at 500 hPa are shown (Cassou, 2010). **63**

Figure 3.2 : The values of EMEDO-Oper indices in 6-h temporal resolution during based on the years of 2015-2021 climatological period, percentage distributions of EMEDO_i during the years (upper center), and adjusted Fisher-Pearson standardized moment coefficients (upper left). **64**

Figure 3.3 : 10-days all EMEDO member oscillations (the vertical axis) surrounding tornado incidents in daily period (the horizontal axis) (17.01.2016). The lightest shaded areas indicate 1 to 3 days before the tornado event of EMEDO_i members, whereas the darkest shaded parts indicate the days when EMEDO_i members begin developing negatively. The area with the most opaque color depicts the day of the tornado (top). Geopotential height [gpdam] at 300 hPa (isohypses) and geopotential height [gpdam] difference between 500hPa and 1000hPa (shaded color contours) (middle). Near-surface (925 hPa) horizontal frontogenesis function [K/100km/3h] (bottom). **65**

Figure 3.4 : 10-days all EMEDO member oscillations (the vertical axis) surrounding tornado incidents in daily period (the horizontal axis) (05.02.2016). The lightest shaded areas indicate 1 to 3 days before the tornado event of EMEDO_i members, whereas the darkest shaded parts indicate the days when EMEDO_i members begin developing negatively. The area with the most opaque color depicts the day of the tornado (top). Geopotential height [gpdam] at 300 hPa (isohypses) and geopotential height [gpdam] difference between 500hPa and 1000hPa (shaded color contours) (middle). Near-surface(925 hPa) horizontal frontogenesis function[K/100km/3h] (bottom). **67**

Figure 3.5 : 10-days all EMEDO member oscillations (the vertical axis) surrounding tornado incidents in daily period (the horizontal axis) (03.03.2016). The lightest shaded areas indicate 1 to 3 days before the tornado event of EMEDO_i members, whereas the darkest shaded parts indicate the days when EMEDO_i members begin developing negatively. The area with the most opaque color depicts the day of the tornado (top). Geopotential height [gpdam] at 300 hPa (isohypses) and geopotential height [gpdam] difference between 500hPa and 1000hPa (shaded color contours) (middle). Near-surface(925 hPa) horizontal frontogenesis function[K/100km/3h] (bottom). **69**

- Figure 3.6 :** 10-days all EMEDO member oscillations (the vertical axis) surrounding tornado incidents in daily period (the horizontal axis) (13.11.2017). The lightest shaded areas indicate 1 to 3 days before the tornado event of EMEDO_i members, whereas the darkest shaded parts indicate the days when EMEDO_i members begin developing negatively. The area with the most opaque color depicts the day of the tornado (top). Geopotential height [gpdam] at 300 hPa (isohypses) and geopotential height [gpdam] difference between 500hPa and 1000hPa (shaded color contours) (middle). Near-surface (925 hPa) horizontal frontogenesis function [K/100km/3h] (bottom). 71
- Figure 3.7 :** 10-days all EMEDO member oscillations (the vertical axis) surrounding tornado incidents in daily period (the horizontal axis) (21.11.2018). The lightest shaded areas indicate 1 to 3 days before the tornado event of EMEDO_i members, whereas the darkest shaded parts indicate the days when EMEDO_i members begin developing negatively. The area with the most opaque color depicts the day of the tornado (top). Geopotential height [gpdam] at 300 hPa (isohypses) and geopotential height [gpdam] difference between 500hPa and 1000hPa (shaded color contours) (middle). Near-surface (925 hPa) horizontal frontogenesis function [K/100km/3h] (bottom). 73
- Figure 3.8 :** 10-days all EMEDO member oscillations (the vertical axis) surrounding tornado incidents in daily period (the horizontal axis) (24.01.2019). The lightest shaded areas indicate 1 to 3 days before the tornado event of EMEDO_i members, whereas the darkest shaded parts indicate the days when EMEDO_i members begin developing negatively. The area with the most opaque color depicts the day of the tornado (top). Geopotential height [gpdam] at 300 hPa (isohypses) and geopotential height [gpdam] difference between 500hPa and 1000hPa (shaded color contours) (middle). Near-surface (925 hPa) horizontal frontogenesis function [K/100km/3h] (bottom). 75
- Figure 3.9 :** 10-days all EMEDO member oscillations (the vertical axis) surrounding tornado incidents in daily period (the horizontal axis) (26.01.2019). The lightest shaded areas indicate 1 to 3 days before the tornado event of EMEDO_i members, whereas the darkest shaded parts indicate the days when EMEDO_i members begin developing negatively. The area with the most opaque color depicts the day of the tornado (top). Geopotential height [gpdam] at 300 hPa (isohypses) and geopotential height [gpdam] difference between 500hPa and 1000hPa (shaded color contours) (middle). Near-surface (925 hPa) horizontal frontogenesis function [K/100km/3h] (bottom). 77
- Figure 3.10 :** 10-days all EMEDO member oscillations (the vertical axis) surrounding tornado incidents in daily period (the horizontal axis) (06.01.2020). The lightest shaded areas indicate 1 to 3 days before the tornado event of EMEDO_i members, whereas the darkest shaded parts indicate the days when EMEDO_i members begin developing negatively. The area with the most opaque color depicts the day of the tornado (top). Geopotential height [gpdam] at 300 hPa (isohypses) and geopotential height [gpdam] difference between 500hPa and 1000hPa (shaded color contours) (middle). Near-surface (925 hPa) horizontal frontogenesis function [K/100km/3h] (bottom). 79

- Figure 3.11** : 10-days all EMEDO member oscillations (the vertical axis) surrounding tornado incidents in daily period (the horizontal axis) (08.10.2020). The lightest shaded areas indicate 1 to 3 days before the tornado event of EMEDO_i members, whereas the darkest shaded parts indicate the days when EMEDO_i members begin developing negatively. The area with the most opaque color depicts the day of the tornado (top). Geopotential height [gpdam] at 300 hPa (isohypses) and geopotential height [gpdam] difference between 500hPa and 1000hPa (shaded color contours) (middle). Near-surface (925 hPa) horizontal frontogenesis function [K/100km/3h] (bottom). **81**
- Figure 3.12** : 10-days all EMEDO member oscillations (the vertical axis) surrounding tornado incidents in daily period (the horizontal axis) (27.01.2021). The lightest shaded areas indicate 1 to 3 days before the tornado event of EMEDO_i members, whereas the darkest shaded parts indicate the days when EMEDO_i members begin developing negatively. The area with the most opaque color depicts the day of the tornado (top). Geopotential height [gpdam] at 300 hPa (isohypses) and geopotential height [gpdam] difference between 500hPa and 1000hPa (shaded color contours) (middle). Near-surface (925 hPa) horizontal frontogenesis function [K/100km/3h] (bottom). **83**
- Figure 3.13** : 10-days all EMEDO member oscillations (the vertical axis) surrounding tornado incidents in daily period (the horizontal axis) (11.02.2021). The lightest shaded areas indicate 1 to 3 days before the tornado event of EMEDO_i members, whereas the darkest shaded parts indicate the days when EMEDO_i members begin developing negatively. The area with the most opaque color depicts the day of the tornado (top). Geopotential height [gpdam] at 300 hPa (isohypses) and geopotential height [gpdam] difference between 500hPa and 1000hPa (shaded color contours) (middle). Near-surface (925 hPa) horizontal frontogenesis function [K/100km/3h] (bottom). **85**
- Figure 3.14** : 10-days all EMEDO member oscillations (the vertical axis) surrounding tornado incidents in daily period (the horizontal axis) (12.10.2021). The lightest shaded areas indicate 1 to 3 days before the tornado event of EMEDO_i members, whereas the darkest shaded parts indicate the days when EMEDO_i members begin developing negatively. The area with the most opaque color depicts the day of the tornado (top). Geopotential height [gpdam] at 300 hPa (isohypses) and geopotential height [gpdam] difference between 500hPa and 1000hPa (shaded color contours) (middle). Near-surface (925 hPa) horizontal frontogenesis function [K/100km/3h] (bottom). **87**
- Figure 3.15** : 10-days all EMEDO member oscillations (the vertical axis) surrounding tornado incidents in daily period (the horizontal axis) (07.12.2021). The lightest shaded areas indicate 1 to 3 days before the tornado event of EMEDO_i members, whereas the darkest shaded parts indicate the days when EMEDO_i members begin developing negatively. The area with the most opaque color depicts the day of the tornado (top). Geopotential height [gpdam] at 300 hPa (isohypses) and geopotential height [gpdam] difference between 500hPa and 1000hPa (shaded color contours) (middle). Near-surface (925 hPa) horizontal frontogenesis function [K/100km/3h] (bottom). **89**

- Figure 3.16 :** 10-days all EMEDO member oscillations (the vertical axis) surrounding tornado incidents in daily period (the horizontal axis) (19.12.2021). The lightest shaded areas indicate 1 to 3 days before the tornado event of EMEDO_i members, whereas the darkest shaded parts indicate the days when EMEDO_i members begin developing negatively. The area with the most opaque color depicts the day of the tornado (top). Geopotential height [gpdam] at 300 hPa (isohypses) and geopotential height [gpdam] difference between 500hPa and 1000hPa (shaded color contours) (middle). Near-surface (925 hPa) horizontal frontogenesis function [K/100km/3h] (bottom). **91**
- Figure 3.17 :** The all EMEDO indices (the vertical axis) in the Whisker-Box plots represent the time period interval (the horizontal axis) of 42 hours before to 30 hours after tornado events initiated. In addition, the EMEDO values at the moment of the tornado are also shown specifically to reveal statistical connection between the events. The boxes extend to the 25th and 75th percentiles, while the whiskers to the 10th and 90th percentiles. Median values are shown as horizontal line within the boxes and mean values are demonstrated as triangle within the boxes. **95**
- Figure 3.18 :** Error distributions between the EMEDO-Oper indice values (the vertical axis) of -0.75 and -3.0 for time period (the horizontal axis) of 42 hours before to 30 hours after for selected tornado events. Mean Absolute Error (left) and Mean Square Error (right). **98**
- Figure 3.19 :** During the 72 hours preceding the tornado (the horizontal axis), all versions of EMEDO_i (top) and EMEDO-Oper (bottom) were analysed for 09.01.2022 event (the vertical axis). The lightly colored regions reflect the sixth to forty-second hours following the local minimum peak of the EMEDO-Oper index. The opaque inner regions indicate the 12th to 30th hours following the local minimum peak of the same index. The vertical black line depicts the instant the tornado occurred. **102**
- Figure 3.20 :** During the 72 hours preceding the tornado (the horizontal axis), all versions of EMEDO_i (top) and EMEDO-Oper (bottom) were analysed for 02.03.2022 event (the vertical axis). The lightly colored regions reflect the sixth to forty-second hours following the local minimum peak of the EMEDO-Oper index. The opaque inner regions indicate the 12th to 30th hours following the local minimum peak of the same index. The vertical black line depicts the instant the tornado occurred. **102**
- Figure 3.21 :** During the 72 hours preceding the tornado (the horizontal axis), all versions of EMEDO_i (top) and EMEDO-Oper (bottom) were analysed for 19.04.2022 event (the vertical axis). The lightly colored regions reflect the sixth to forty-second hours following the local minimum peak of the EMEDO-Oper index. The opaque inner regions indicate the 12th to 30th hours following the local minimum peak of the same index. The vertical black line depicts the instant the tornado occurred. **103**
- Figure 3.22 :** During the 72 hours preceding the tornado (the horizontal axis), all versions of EMEDO_i (top) and EMEDO-Oper (bottom) were analysed for 15.10.2022 event (the vertical axis). The lightly colored regions reflect the sixth to forty-second hours following the local minimum peak of the EMEDO-Oper index. The opaque inner regions indicate the 12th to 30th hours following the local minimum peak of the same index. The vertical black line depicts the instant the tornado occurred. **103**

| | |
|---------------------------------------------------------------------------------------------------------------------------------------------------------------------------------------------------------------------------------------------------------------------------------------------------------------------------------------------------------------------------------------------------------------------------------------------------------------------------------------------------------------------------------|------------|
| Figure 3.23 : During the 72 hours preceding the tornado (the horizontal axis), all versions of EMEDO _i (top) and EMEDO-Oper (bottom) were analysed for 07.11.2022 event (the vertical axis). The lightly colored regions reflect the sixth to forty-second hours following the local minimum peak of the EMEDO-Oper index. The opaque inner regions indicate the 12th to 30th hours following the local minimum peak of the same index. The vertical black line depicts the instant the tornado occurred..... | 104 |
| Figure A. 1 : 17.01.2016 | 116 |
| Figure A. 2 : 03.03.2016 | 116 |
| Figure A. 3 : 13.11.2017 | 117 |
| Figure A. 4 : 21.11.2018 | 118 |
| Figure A. 5 : 24.01.2019 | 118 |
| Figure A. 6 : 26.01.2019 | 119 |
| Figure A. 7 : 08.10.2020 | 119 |
| Figure A. 8 : 07.12.2021 | 120 |
| Figure A. 9 : 19.12.2021 | 120 |
| Figure A. 10 : 07.11.2022 | 121 |
| Figure A. 11 : 15.10.2022 | 122 |
| Figure A. 12 : 19.04.2022 | 123 |
| Figure B. 1 : Geopotential height [gpdam] at 300 hPa (isohypsies) and geopotential height [gpdam] difference between 500hPa and 1000hPa (shaded color contours) 27.07.2017 – 12 UTC | 124 |
| Figure C. 1 : Number of tornado events and (b) strong–violent (F2 and stronger) tornado events per 10000 km ² . The density was computed by dividing the number of events within (a) 100 and (b) 200 km of a point by the surface area of a circle with the respective radius (Groenemeijer & Kühne, 2014). | 125 |

DEVELOPMENT OF AN EARLY INDICATOR INDEX FOR TORNADIC STORMS IN THE EURO-MEDITERRANEAN REGION

SUMMARY

Tornadoes are the most violent and destructive of all the severe weather phenomena that localized convective storms produce. Supercells in particular and severe convective storms in principle are among the primarily responsible section for the global losses in both lives and properties caused by tornadoes. A tornado is a narrow and violently rotating column of air, in contact with the ground, either pendant from a cumuliform cloud or underneath a cumuliform cloud, and often (but not always) visible as a funnel cloud around wall cloud. For a vortex to be classified as a tornado, it must be in contact with both the ground (or sea surface) and the cloud base.

The movement, type, strength, and influence of fronts on clouds and precipitation must be accounted for in weather forecasts. Fronts can produce severe, structured convective storms, depending on the air's static stability in the presence of a frontal system. When the temperature and humidity gradients across the front become stronger, leading to the development of a more distinct and well-defined frontogenesis.

It is revealed that as one of the main phenomena in severe weather in meteorology, thunderstorms are the most common source of hazardous weather at local scales including large hail, strong winds, and tornadoes. Known as mesoscale convective systems (MCS), these thunderstorm clusters are smaller than low-pressure systems with cold and warm fronts, but larger in scale than any single thunderstorm. Supercells or bow echoes may be embedded within MCSs and also coexist with multicells. Strong tornadoes are mostly produced by these persistent severe thunderstorms which known as mesocyclone supercell storms or bow-echo storms in terms of storm type in radar echo.

In order to understand how a tornado occurs, it is necessary to examine the dynamics of mid-latitude front systems and mesoscale convective storm mechanisms (thunderstorms) very well. The middle latitudes between about 30° and 50° North or South, climatologically provide the most favorable environment for tornado-genesis and sometimes in land-falling tropical cyclones, nevertheless, common in US and Canada. Likewise, Europe is also intriguing continent for occurrence of severe convective storms and tornadoes. The highest density of tornado reports is in western and central Europe. In fact, the southern and southwestern coastline of Turkiye is likely among the most tornado-prone regions of Europe and it has a potential to produce non-mesocyclonic waterspouts.

The upper-level lows (ULLs) and troughs are responsible for 47% of tornado days and 55% of very large hail days in Turkiye, in addition to that, nearly a quarter of all synoptic patterns are covered by Mediterranean cyclones with both central and eastern origins, which are well-known and common wintertime events. Nonmesocyclonic

tornadoes (mostly waterspouts) are most common in the winter along the (southern) Mediterranean coast and in the fall along the (northern) Black Sea coast.

Principally, a convective storm requires four main ingredients to form with mesocyclones; low-level moisture, instability, lifting trigger mechanism, wind shear. In previous studies, numerous composite parameters that incorporate measures of tornadoes have been developed such as Significant Tornado Parameters (STP), Supercell Composite Parameters (SCP), Significant Hail Parameter (SHIP), and so forth. However, these are useful to identify tornadic storm environments for a specific location based on probabilistic forecasts which currently utilized by national weather services and private companies. The fact that high sea water temperature anomalies around Mediterranean increase the number of tornado/waterspouts in non-mesocyclonic structure indicates that formulas such as STP and SCP cannot perpetually be pioneer guides. Understanding and progressing mesoscale model studies becomes important at this point in order to predict tornado formation and dynamical concepts. Due to this reason, high-resolution modeling is a must a few days in advance for mesocyclonic supercell thunderstorms capable of producing F2+ tornadoes in particular. Unfortunately, to predict where and when tornadoes may occur, computational costs of constantly operating high-resolution numerical weather prediction models are hard to afford financially even for these institutes. Moreover, if the spatial and temporal resolution of the modeling is insufficient, these composite parameters make it unlikely where the tornado will occur.

The purpose of the study is to produce an index which allows to reduce the uncertainty of severe convective storms and tornadoes in the scope of climate change adaptation strategies. The main intention is not to replace or substitute these modeling approaches, or composite indexes mentioned above, but to warn operationally to draw attention to the Eastern Mediterranean and Turkiye in particular a few days in advance. The development of some indicators using atmospheric variables can undertake a crucial role by enabling such numerical models to be run only at certain time intervals, thus enduring lower costs.

In this study, Eastern Mediterranean Oscillation Index (EMEDO_i) has been developed in order to be able to detect the presence of ULLs and frontogenesis approach is employed for selected tornadic storm events in Turkiye. EMEDO_i has 7 different its variations (members). These members have been developed to detect differences depending on the entry directions of cyclones and storms affecting Turkiye from the west of the country. In line with the GDAS data analysis, values of geopotential height are derived for the requirement of EMEDO_i in a limited area.

The formation of a front on the Eastern Mediterranean is crucial for these devastating tornadic storms and the sweep mechanism in upper-level towards Turkiye by this front should support the environmental conditions of these storms. This is because for occurring a tornadic storm activity, there is a contribution of sweeping mechanism at jet-streak level in order to allow updraft air to move upward as a necessity of conservation of air mass law in the atmosphere (Equation of Continuity). High level jet streaks and their fields can be identified thanks to isobaric temperatures and isobaric geopotential height levels. Just before the imminent of the tornado events, it is revealed that geopotential thickness difference values decrease at P1-3 and C points covering Italy, Greece, and Albania. At the same time, across the index poles, the difference between isohypse values increases due to the high temperature gradient of 300 hPa. As the spread of all members of EMEDO_i expanded with forecast time, it took on

different values than EMEDO-Ens or EMEDO-Oper, making it more difficult to explain the consequences of modifying or determining nonmesocyclonic waterspouts and mesocyclonic supercell tornado structures. Consequently, it may also be claimed that the amplitude of the EMEDO perturbations may have been either small or too large for a severe weather warning, and that the EMEDO spatial variability (noisy patterns) may have diminished the signal. Therefore, it is not obviously seems that the stronger the trend due to the change of this phase, the greater the damage of the storms. However, the stronger the negative EMEDO phase, the higher the geopotential gradient between the trough and the ridge, so the conditions are more favorable for frontogenesis in the eastern Mediterranean. In this way, the strength of fronts were generally observed as strong classification which is defined as more than 8K per 110km. In a few cases of events which are reported as waterspout, the strength and the presence of the fronts can be considered moderate classification (4K/110km).

A few of the results from the study are as in the following: 86% of the trained tornado events revealed that the EMEDO-Oper index was in negative phase at the time a tornado was reported, regardless of whether the events featured a supercell mesoscale convective storm or a frontal movement. The time required to reach the local minimum varies based on the tornado occurrence. Based on the tornadic storm scenario in the test cluster in 2022 and the train cluster, this timeframe is predicted to be roughly 33,2 hours on average. In western Turkiye, there is a 79% chance of a tornado occurring between six and forty-two hours after the EMEDO-Oper index reaches its local minimum. In particular, the projected chance for this period is 63% between 12 and 30 hours after the local minimum is obtained. Besides, the majority of the tornado incidents with EMEDO-Oper values below -0.75 were evaluated. After an EMEDO-Oper index value falls below that threshold, it is likely to forecast the risk period of a tornado in Turkiye with a probability of 79% and the local minimum point must be identified.

To sum up, tornadic SCS activities increase in Turkiye during the first few days of sudden ascents from negative EMEDO_i phase to neutral EMEDO_i phase. The findings may contribute to researches for numerical weather prediction modeling in terms of low-level moisture, instability, lifting trigger mechanism and wind shear transport sensitivity into the Euro-Mediterranean, and its relation with the tornadic storm activities over the Eastern Mediterranean region.



AVRUPA-AKDENİZ BÖLGESİ'NDEKİ TORNADİK FIRTINALAR İÇİN ERKEN GÖSTERGE ENDEKSİNİN GELİŞTİRİLMESİ

ÖZET

Hortumlar, lokal konvektif fırtınaların ürettiği şiddetli hava olaylarının en şiddetlisi ve yıkıcısıdır. Özellikle süper hücreler ve prensip olarak şiddetli konvektif fırtınalar, hortumların neden olduğu küresel can ve mal kayıplarının birincil sorumluları arasındadır. Bir hortum, ya bir kümülüs bulutundan sarkan ya da bir kümülüs bulutunun altında yerle temas halinde olan ve genellikle (ancak her zaman değil) duvar bulutunun etrafında bir huni bulutu olarak görülebilen, dar ve şiddetle dönen bir hava sütunudur. Bir girdabın hortum olarak sınıflandırılabilmesi için hem yer (veya deniz yüzeyi) hem de bulut tabanı ile temas halinde olması gerekir.

Cephelerin hareketi, türü, gücü ve bulutlar ve yağış üzerindeki etkisi hava tahminlerinde hesaba katılmalıdır. Cepheler, bir cephe sisteminin mevcudiyetinde havanın statik kararlılığına bağlı olarak şiddetli, yapılandırılmış konvektif fırtınalar üretebilir. Ön kısımdaki sıcaklık ve nem gradyanları daha güçlü hale geldiğinde, daha belirgin ve iyi tanımlanmış bir cephe oluşumunun gelişmesine yol açar.

Meteorolojide şiddetli hava koşullarındaki ana olaylardan biri olan gök gürültülü fırtınaların, büyük dolu, kuvvetli rüzgarlar ve hortumlar dahil olmak üzere yerel ölçekte en yaygın tehlikeli hava kaynağı olduğu ortaya çıkarılmıştır. Orta ölçekli konvektif sistemler (MCS) olarak bilinen bu fırtına kümeleri, soğuk ve sıcak cephelere sahip düşük basınçlı sistemlerden daha küçüktür, ancak herhangi bir tek fırtınadan daha büyüktür. Süper hücreler veya yay ekoları, MCS'lerin içine gömülebilir ve ayrıca çok hücrelilerle bir arada bulunabilir. Güçlü hortumlar çoğunlukla, radar yankısındaki fırtına tipi açısından mezosiklon süper hücreli fırtınalar veya yay yankılı fırtınalar olarak bilinen bu sürekli şiddetli gök gürültülü fırtınalar tarafından üretilir.

Bir hortumun nasıl oluştuğunu anlamak için orta enlem cephe sistemleri ve orta ölçekli konvektif fırtına mekanizmalarının (gökgürültülü fırtına) dinamiklerini çok iyi incelemek gerekir. Yaklaşık 30° ile 50° Kuzey veya Güney arasındaki orta enlemler, klimatolojik olarak hortum oluşumu için ve bazen karaları vurabilen tropikal siklonlar için en uygun ortamı sağlar, ve bunlar ABD ve Kanada'da yaygındır. Aynı şekilde Avrupa da şiddetli konvektif fırtına ve hortumların meydana gelmesi açısından ilgi çekici bir kıtadır. Hortum raporlarının en yüksek yoğunluğu batı ve orta Avrupa'dadır. Aslında, Türkiye'nin güney ve güneybatı kıyı şeridi muhtemelen Avrupa'nın hortumlara en yakın bölgeleri arasındadır ve mezosiklonik olmayan su hortumları üretme potansiyeline sahiptir.

Türkiye'deki hortum günlerinin %47'sinden ve çok büyük dolu günlerinin %55'inden yukarı seviye siklonları (ULL) ve oluklar sorumludur, buna ek olarak, tüm sinoptik patern örüntülerinin yaklaşık dörtte biri, hem orta hem de doğu kökenli Akdeniz siklonları tarafından kapsamaktadır ve bunlar iyi bilinen ve yaygın kış sezonu meteorolojik olaylardır. Mezosiklonik olmayan hortumlar (çoğunlukla su hortumları)

en çok kışın (güney) Akdeniz kıyılarında ve (kuzey) Karadeniz kıyılarında sonbaharda yaygındır.

Prensip olarak, bir konvektif fırtınanın mezosiklonlarla oluşması için dört ana bileşen gerekir; aşağı seviyedeki nem, kararsızlık, kaldırma tetikleme mekanizması, rüzgâr makaslama. Önceki çalışmalarda, Önemli Hortum Parametresi (STP), Süper Hücre Bileşik Parametresi (SCP), Önemli Dolu Parametresi (SHIP) ve benzeri gibi hortum üretebilen fırtına ölçümlerini içeren çok sayıda bileşik parametre geliştirilmiştir. Ancak bunlar, şu anda ulusal hava servisleri ve özel şirketler tarafından kullanılan olasılık tahminlerine dayalı olarak belirli bir konum için hortum üretebilen fırtına ortamlarını belirlemek için kullanışlıdır. Akdeniz çevresindeki yüksek deniz suyu sıcaklık anomalilerinin mezosiklonik olmayan yapıda hortum/su hortumu sayısını artırması, STP ve SCP gibi formüllerin her zaman öncü rehber olamayacağını göstermektedir. Hortum oluşumu ve dinamik kavramların tahmin edilebilmesi için mezo ölçekli model çalışmalarının anlaşılması ve ilerletilmesi bu noktada önem kazanmaktadır. Bu nedenle, özellikle F2+ hortumları üretebilen mezosiklonik süperhücreli fırtınalar için birkaç gün önceden yüksek çözünürlüklü modelleme şarttır. Ancak ne yazık ki, hortumların nerede ve ne zaman meydana gelebileceğini tahmin etmek için, sürekli çalışan yüksek çözünürlüklü sayısal hava tahmin modellerinin hesaplama maliyetlerini bu enstitüler için bile finansal olarak karşılamak zordur. Ayrıca, modellemenin mekansal ve zamansal çözünürlüğü yetersizse, bu bileşik parametreler hortum nerede oluşacağını bilmenizi imkansız hale getirir.

Çalışmanın amacı, iklim değişikliğine uyum stratejileri kapsamında şiddetli konvektif fırtına ve hortumların belirsizliğini azaltmaya olanak sağlayan bir endeks üretmektir. Asıl amaç, bu modelleme yaklaşımlarını veya yukarıda belirtilen bileşik endeksleri değiştirmek veya ikame etmek değil, özellikle birkaç gün önceden Doğu Akdeniz ve Türkiye'ye dikkat çekmek için operasyonel olarak uyarıda bulunmaktır. Atmosferik değişkenler kullanılarak bazı göstergelerin geliştirilmesi, bu tür sayısal modellerin yalnızca belirli zaman aralıklarında çalıştırılmasını ve böylece daha düşük maliyetlere dayanmasını sağlayarak kritik bir rol oynayabilir.

Bu çalışmada, ULL'lerin varlığını tespit edebilmek için Doğu Akdeniz Salınım İndeksi (EMEDO_i) geliştirilmiş ve Türkiye'deki seçilmiş hortum fırtına olayları için cephe oluşumu yaklaşımı kullanılmıştır. EMEDO_i'nin 7 farklı varyasyonu (üyesi) vardır. Bu üyeler, ülkenin batısından Türkiye'yi etkileyen siklon ve fırtınaların giriş yönlerine bağlı olarak farklılıkları tespit etmek için geliştirilmiştir. GDAS veri analizi doğrultusunda, sınırlı bir alanda EMEDO_i gereksinimi için jeopotansiyel yükseklik değerleri türetilmiştir.

Bu yıkıcı hortumlar için Doğu Akdeniz'de bir cephe oluşması çok önemlidir ve bu cephenin üst seviyede Türkiye'ye doğru süpürme mekanizması bu fırtınaların çevre koşullarını desteklemelidir. Bunun nedeni, hortumlu bir fırtına faaliyetinin meydana gelmesinde, atmosferdeki hava kütle yasasının (Süreklilik Denklemi) korunumu gereği yukarı yönlü havanın yukarı doğru hareket etmesini sağlamak için jet çizgisi seviyesinde süpürme mekanizmasının katkısının olmasıdır. İzobarik sıcaklıklar ve izobarik jeopotansiyel yükseklik seviyeleri sayesinde yüksek seviyeli jet rüzgarı alanları belirlenebilir. Yaklaşan hortum olaylarından hemen önce İtalya, Yunanistan ve Arnavutluk'u kapsayan P1-3 ve C noktalarında jeopotansiyel kalınlık farkı değerlerinin düştüğü ortaya çıkmıştır. Aynı zamanda endeks kutupları arasında 300 hPa'lık yüksek sıcaklık gradyanı nedeniyle izohips değerleri arasındaki fark artmaktadır. Sonuç olarak, mezosiklonik olmayan su hortumlarını ve mezosiklonik

süper hücreli hortum yapılarını değiştirmenin veya belirlemenin sonuçlarını açıklamayı zorlaştırırsa da, EMEDO üyelerinin genliğinin şiddetli bir hava uyarısı için küçük veya çok büyük olabileceği ve EMEDO uzamsal değişkenliğinin (gürültülü modeller) sinyali azaltmış olabileceği de iddia edilebilir. Bu nedenle, bu fazın değişmesinden kaynaklanan eğilim ne kadar güçlüyse, fırtınaların verdiği zararın o kadar büyük olduğu açıkça görülmemektedir. Bununla birlikte, negatif EMEDO fazı ne kadar güçlü olursa, oluk ve sırt arasındaki jeopotansiyel gradyan o kadar yüksek olur ve bu nedenle Doğu Akdeniz'de cephe oluşumu için koşullar daha elverişlidir. Bununla birlikte, cephelerin gücü genel olarak 110km'de 8K'den fazla olarak tanımlanan güçlü cephe sınıflandırması olarak gözlemlendi. Su hortumu olarak bildirilen birkaç olay özelinde ise, cephelerin gücü ve varlığı orta dereceli sınıflandırma olarak kabul edilebilir (4K/110km).

Çalışmadan elde edilen sonuçlardan birkaçı aşağıdaki gibidir: Test edilmiş hortum olaylarının %86'sı, olayların bir süper hücre mezo ölçekli konvektif özelliğine veya cephesel hareket özelliğine sahip olup olmadığına bakılmaksızın, bir hortum rapor edildiğinde EMEDO-Oper indeksinin negatif fazda olduğunu ortaya çıkardı. Yerel minimuma ulaşmak için gereken süre, hortum oluşumuna bağlı olarak değişir. 2022'deki test veri kümesindeki hortum fırtınası senaryosuna ve eğitilmiş veri kümesine dayanarak, bu zaman diliminin ortalama olarak yaklaşık 33,2 saat olabileceği tahmin edilmektedir. Türkiye'nin batısında, EMEDO-Oper endeksi yerel minimum değerine ulaştıktan sonraki 6 ile 42 saat arasında %79 oranında bir hortum meydana gelme olasılığı vardır. Özellikle, yerel minimuma ulaşıldıktan sonraki 12 ila 30 saat arasında bu süre için öngörülen şans %63'tür. Ayrıca, EMEDO-Oper değerleri -0,75'in altında olan hortum olaylarının çoğu değerlendirildi. Bir EMEDO-Oper indeks değeri bu eşik altına düştükten sonra, Türkiye'de bir hortumun risk dönemini %79 olasılıkla tahmin etmesi muhtemeldir ve yerel minimum noktanın belirlenmesi gerekir.

Özetlemek gerekirse, negatif EMEDO_i fazından nötr EMEDO_i fazına ani yükselişlerin ilk birkaç gününde Türkiye'de hortumlu SCS faaliyetleri artmaktadır. Bulgular, Avrupa-Akdeniz'e aşağı seviyedeki nem, kararsızlık, kaldırma tetikleme mekanizması, rüzgâr makaslaması taşıma hassasiyeti ve bunun Doğu Akdeniz bölgesindeki hortumlu fırtına aktiviteleri ile ilişkisi açısından sayısal hava tahmin modellemesi araştırmalarına katkıda bulunabilir.



1. INTRODUCTION

Severe convective storms worldwide inflict damage to property and crops, disrupt air, sea, and ground travel and outdoor activity, and, in the most extreme cases, inflict injuries and even death. In terms of defining a convective storm as severe/non-violent, measurable or calculable parameters associated with important weather events, which often exceed certain local threshold values (Doswell, 2001). Regardless of whether or not there is actual damage; the Storm Prediction Center (SPC) of the National Weather Service (NWS) in the U.S. describes "severe" weather associated with local storms (as opposed to storms that are much larger in scale such as extratropical and tropical cyclones) as having one or more of the following: tornadoes, winds equal to or exceeding 25.8 ms^{-1} , or hail 2.5 cm or greater in diameter (Bluestein, 2013).

Tornadoes are the most violent and destructive of all the severe weather phenomena that localized convective storms produce, and they can associate with super-cells as mother of all storms. Severe Convective Storms (SCS) are responsible from an important section of the meteorological hazards causing losses of lives and property worldwide. Tornadoes, severe hail, excessive rains resulting in flash flooding and heavy rain flood, and severe wind gusts are all associated with the development of severe convective storms. They are all the result of mesoscale to microscale processes based primarily on deep moist convection. In recent years, there are proofs for specific regions around the world that tornadic storms often accompany severe convective weather getting increased day by day (Fig.1.1).

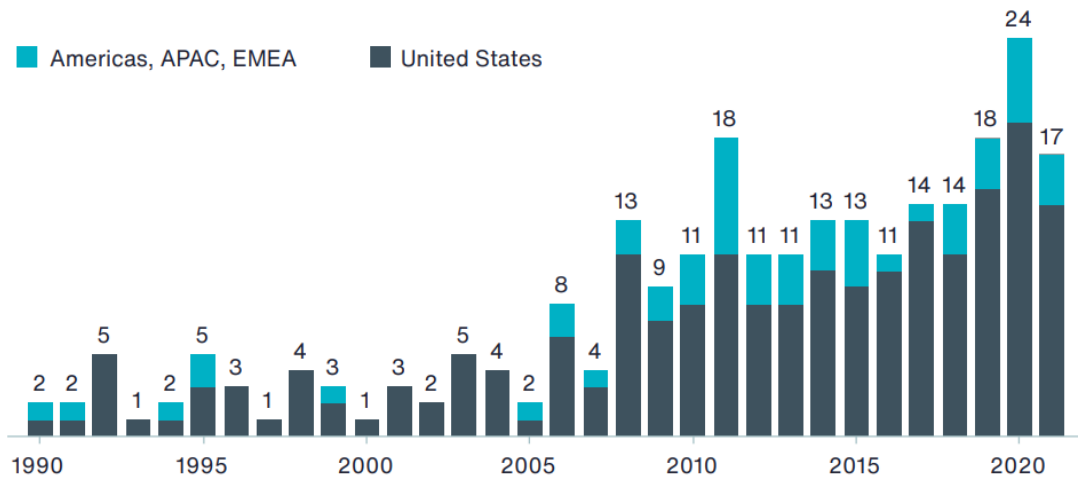


Figure 1.1 : Number of SCS events that caused at least USD500 million insured loss. Europe, Middle East & Africa (EMEA) indicates Europe, Middle East & Africa continents and Asia & Pacific (APAC) represents Asia & Pacific regions (AON, 2021).

In the past decade, tornadoes have caused more than \$14.1 billion in total damage across the United States (US). Besides, from 2010 through 2020, tornadoes resulted in \$2.5 million in property damage per storm in US. According to another report, storm-related loss has a share of \$171B of \$476B in total economic losses due to meteorological damages in the last 50 years only in Europe (WMO, 2021). It is known that tornadoes and convective/frontal storms take on a major role in a significant part of these. Nevertheless, economic losses due to only hail, tornado and lightning in 21st century is \$11B only in Europe (WMO, 2021).

1.1 Purpose of Thesis

In the past four decades, much has been discovered various atmospheric circulations on a local scale that relevant to tornado formation and structure from observations, laboratory models, and numerical-simulation experiments. Nowadays, one of the global climate crisis and adaptation process is to minimize the impacts the severe weather events may cause by utilizing warning systems. At this point, the comprehending and advancing of mesoscale models studies become particularly crucial in order to predict the formation and dynamical concepts of tornadoes.

Forecasting convective storms and their attendant hazards, such as tornadoes or large hail, requires knowledge of the characteristics of the environments in which the phenomena tend to occur. Tornadoes have been blamed for at least %4 number of reported economic losses by hazard type around the world (WMO, 2021).

Nowadays, government agencies such as NOAA's SPC and some private companies operationally publish probabilistic tornado forecasts for a few days in advance. The various kinematic or thermodynamic indices that have been developed to provide local insight into storms and associated supercell mesocyclonic convective systems, but it is very costly to get a sharp and exact geospatial location result of where tornadoes may occur. In today's world, except for nowcasting predictions, companies or institutions have the technology to issue a warning by identifying risk areas for tornadoes, typically only a few days in advance (Fig. 1.2).

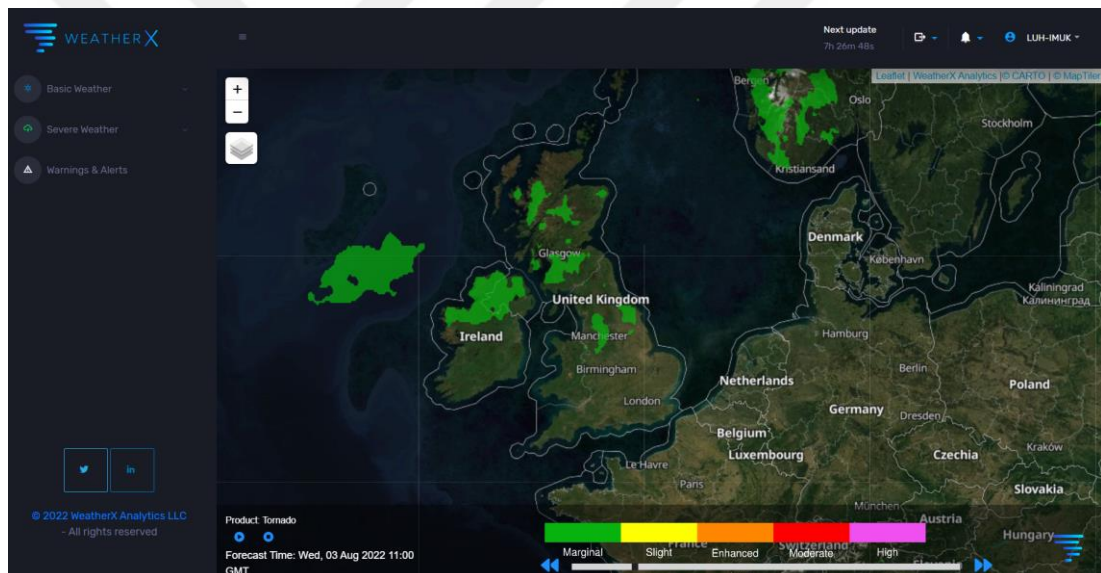


Figure 1.2 : A tornado forecast by Cassandra Forecasting Model valid for August 3, 2022, 11:00 UTC (WeatherX, 2022).

For this reason, institutions can get rid of high computing costs of numerical modeling if limited area models such as WRF are run for a few days before starting instead of all days to monitor these convective systems operationally. In order to predict these atmospheric conditions, the EMEDO index is developed by using synoptic (or mesoscale) patterns in the Eastern Mediterranean.

Understanding severe weather environments of tornadic storms in Turkiye will lead to determining mesoscale mechanisms favoring tornadic storms and tornadoes, and these

will be some key outcomes of the study not only for researchers, but also for operational forecasters a few days in advance.

The purpose of this study is to evaluate and to reveal the connection between a new Mediterranean Index and tornadic storms.

1.2 Literature Review

1.2.1 Research on severe convective storms and related hazards: A brief history

In the scope of early development of weather forecasting, the first ever daily weather forecasts were published in *The Times* on August 1, 1861, and the first weather maps were produced later in the same year. In 1911, the Met Office began issuing the first marine weather forecasts via radio transmission. These included gale and storm warnings for areas around Great Britain. Concerning severe weather, USA is the country which suffers most from severe convective storms. One can begin with Benjamin Franklin's kite flight experiments in the 18th century, John Park Finley's gathering of tornado reports in the United States in the late 1800s, and Alfred Wegener's collection of tornado reports in Germany in the early 1900s (Doswell, 2007). However, The Thunderstorm Project of the 1940s is typically regarded as the beginning of current research on extreme thunderstorms, which has served as the base for contemporary scientific understanding.

In the early days of severe weather forecasting in the U. S. in the 1950s and 1960s, synoptic conditions associated with severe convection in the Great Plains and to the east were identified. By atmospheric sciences community, tornadoes are of greatly interested to explain the processes involved in the genesis, development, and decay of tornadoes within supercells remains an active research topic since they are capable of inflicting extreme and intense damage, injuries, and loss of life.

In the 1970s and 1980s, numerical simulations of supercell thunderstorms were conducted out, and these simulations served as the basis for the development of scientific hypotheses regarding the formation, strength, and evolution of supercells (Wilhelmson and Wicker 2001). The foundation of this knowledge has been expanded upon by more recent model-based research, which have accomplished so by introducing increasingly sophisticated and realistic simulations of the storm's dynamics and physics. To explore the dynamics of analytically forced, fully resolved

tornadoes in the absence of an explicitly resolved parent storm, highly idealized numerical models have been run at extremely high resolution over relatively small domains. These models have been used to run at extremely high resolution. Because of advances in computing technology, it has now become possible to run simulations of supercells to resolutions at which tornadoes may be explicitly resolved (Orf et al. 2017).

1.2.2 Types of atmospheric fronts (frontogenesis) & air masses

A crucial aspect of understanding weather is knowing about air masses and the transitions between them. This is particularly important in the temperate zones where transitions between warm and cold air masses create zones of precipitation called fronts. Fronts can strongly impact local weather conditions, and forecasts must account for their movement, type, intensity, and influence on cloud and precipitation. Depending on the static stability of air in the vicinity of a frontal system, fronts can trigger severe, organized convective storms. In order to comprehend the notion of fronts, a surface weather analysis which is a special type of weather map is necessary. Dynamic features of an atmospheric front can be identified with the relevant variables such as sea-level pressure, temperature, humidity, and cloud cover, and precipitation area. In addition to these variables, fronts are generally guided by winds aloft. In the scope of the Margules Model, the inclination of the weather fronts can be determined. Especially, atmospheric fronts have unique cross-frontal circulations in the surrounding environment.

The Bergeron classification is the most widely recognized form of air mass classification. In Fig. 1.3, there is a general classification scheme for air masses based on the climate region where they originate. The first letter is based on whether the air mass originates over land or water. Air masses originating over land are called continental and are dry, while air masses that form over water are called maritime and are moist (Holton, 2004).

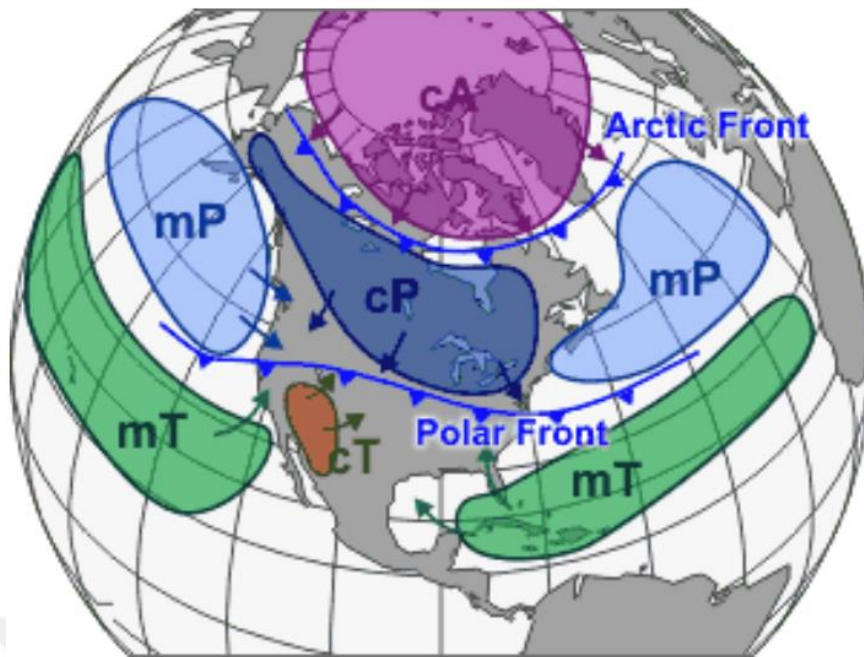


Figure 1.3 : Common pressure patterns and fronts in USA and air masses classification in accordance with region (NOAA, 2021).

The classifications of the many types of air masses are characterized by three letters. The initial letter is based on whether the air mass originates over land or water. Air masses originating over land are called continental and are dry, while air masses that form over water are called maritime and are moist (Holton, 2004). The consistency of the environment is represented by the third letter. Fronts are placed along troughs of lower pressure and serve to separate air masses that are of various sorts or originate from different places. It is clear that the various air masses that are responsible for the weather in North America, as well as on other continents, tend to be divided by frontal borders (Bluestein, 1993). In this example, the Arctic front is responsible for separating the Arctic air mass from the Polar air mass, while the Polar front is responsible for separating the Polar air mass from the warm air mass. (The continental arctic, the continental polar, the maritime polar, the continental tropic, and the maritime tropic are all abbreviated as cA, cP, and mP, respectively.)

Fronts can be defined as regions of enhanced horizontal temperature or potential temperature gradient. It is proposed to classify temperature gradients of 8K per 220 km as “moderate” and 8K per 110 km as “strong.” It is proposed for the atmospheric front term as baroclinic zones exhibiting a strong cyclonic wind shift at their warm edge (Lackmann, 2011). The Glossary of Meteorology (AMS) defines a front as the “interface or transition zone between two air masses of different density”. This

requires the use of a density variable, such as virtual temperature, virtual potential temperature, or density, to identify a front. Therefore, it should be briefly considered that a weather front is a boundary separating air masses of several characteristics such as air density, wind, and humidity. Perhaps the simplest definition of a front is that it represents an air mass boundary. This definition should contain the terminology for boundaries such as drylines, and so forth.

Local weather conditions can be greatly affected by fronts, and forecasts must account for frontal movement, type (Fig 1.4), intensity, and influence on cloud and precipitation. Depending on the static stability of air in the vicinity of a frontal system, fronts can trigger severe, organized convective storms. The presence of enhanced vertical wind shear in frontal zones, as required by thermal wind balance, contributes to the organization and severity of mesoscale convective storms that form in their vicinity. In some situations, convective storms can develop in succession along frontal boundaries, resulting in flashflooding as sequential cells move over the same areas repeatedly.

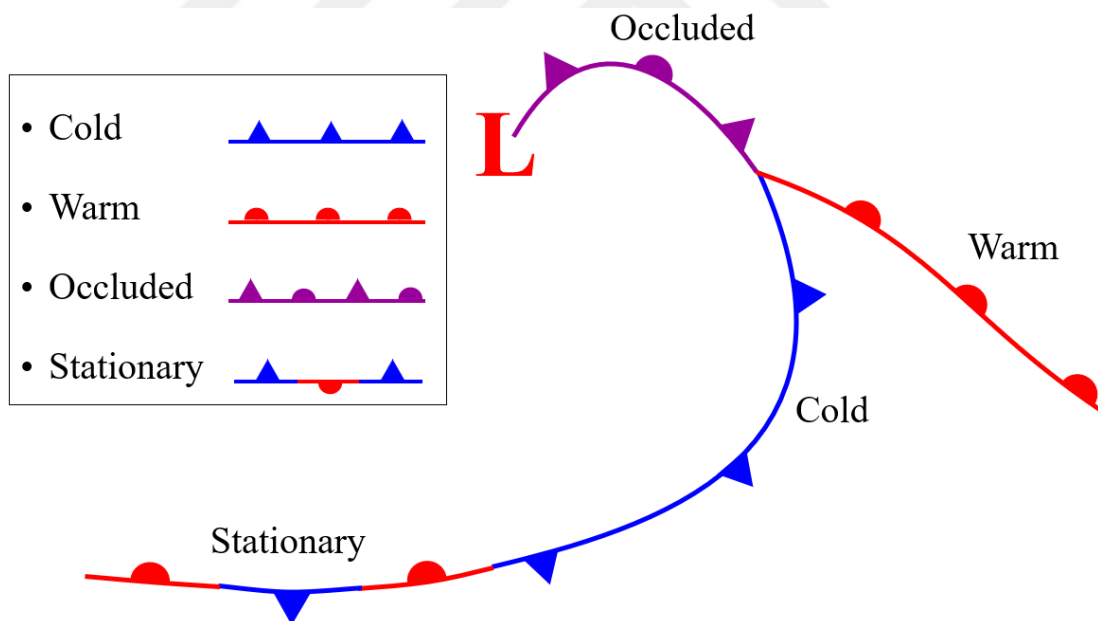


Figure 1.4 : Four main types of weather fronts and their demonstrations for a weather map (Mentes, 2020).

Both the horizontal wind shift and vertical wind shear accompanying frontal zones have important implications for forecasting in various sectors. The timing of fronts can be critical to determining the amount and type of precipitation in a given location. The

shelf clouds and cumulonimbus clouds can be a sign that a squall line is imminent (Bluestein, 1993).

1.1.1.1 Cold & warm fronts

On weather maps, the surface position of the cold front is marked by a blue line with triangles pointing in the direction of cold air travel and it is placed at the leading edge of the cooler air mass. Therefore, cold front occurs when a mass of cold, dry air displaces a mass of warm, moist air. In the process of this displacement, a lot of latent heat energy is released, often creating thunderstorms. The profile of a cold front is very different from the wedge-like shape of warm front. Because the cold air is denser than the warm air it's displacing. Also because of its density, cold fronts move faster than warm fronts, as it's easier for the cold, dense air to displace the warm air. One feature of cold fronts that's important to know is that the warm surface air ahead of the advancing front gets drawn in toward the frontal boundary. Surface winds are actually feeding the storm. However, the steering winds aloft are still coming from the west.

The cold air moves and it pushes warm, moist air up into the atmosphere (Fig 1.5). As this air rises, it condenses into droplets. The act of condensation releases heat to the surrounding air. This heat causes the surrounding air to become buoyant and rise. In turn, this draws in still warmer, moist air along the surface ahead of the front, which again condenses, and again releases heat. This process goes on and on, creating a runaway feedback effect. This is one of the reasons that the storms associated with cold fronts are so violent. In the northern hemisphere, there is a clockwise pattern named veering, meaning that for the observer, it starts from the east, or southeast, or south, as it's being drawn toward the storm. Then, it shifts into the southwest as the front moves through and then finally to the west after the storm has passed (Holton, 2004). They often bring rain, and sometimes heavy thunderstorms as well. They can produce sharper changes in weather and they move at a rate that is up to twice as fast as warm fronts, since cold air is denser than warm air. If there is sufficient humidity, the lifting mechanism may either cause a line of showers and thunderstorms to form along a certain path. The idea that colder, denser air "wedges" under warmer, less dense air is overly simplistic because the upward motion is truly part of a mechanism that maintains geostrophic equilibrium on a revolving Earth in response to frontogenesis (Huth, 2013). In the field of meteorology, a cold front can be described

using one of three distinct subtitles when it is located near a frontal zone. The term "anafront" is used to refer to a border that exhibits instability, which means that air rises fast along and over the boundary, causing substantial changes in the weather. A "katafront" is a less powerful weather system that brings more moderate shifts in temperature and humidity, in addition to less precipitation. In the spring time, it is mostly observed at the northeastern part of US due to the influence of relatively cold arctic water in the North Atlantic (Lackmann, 2011).

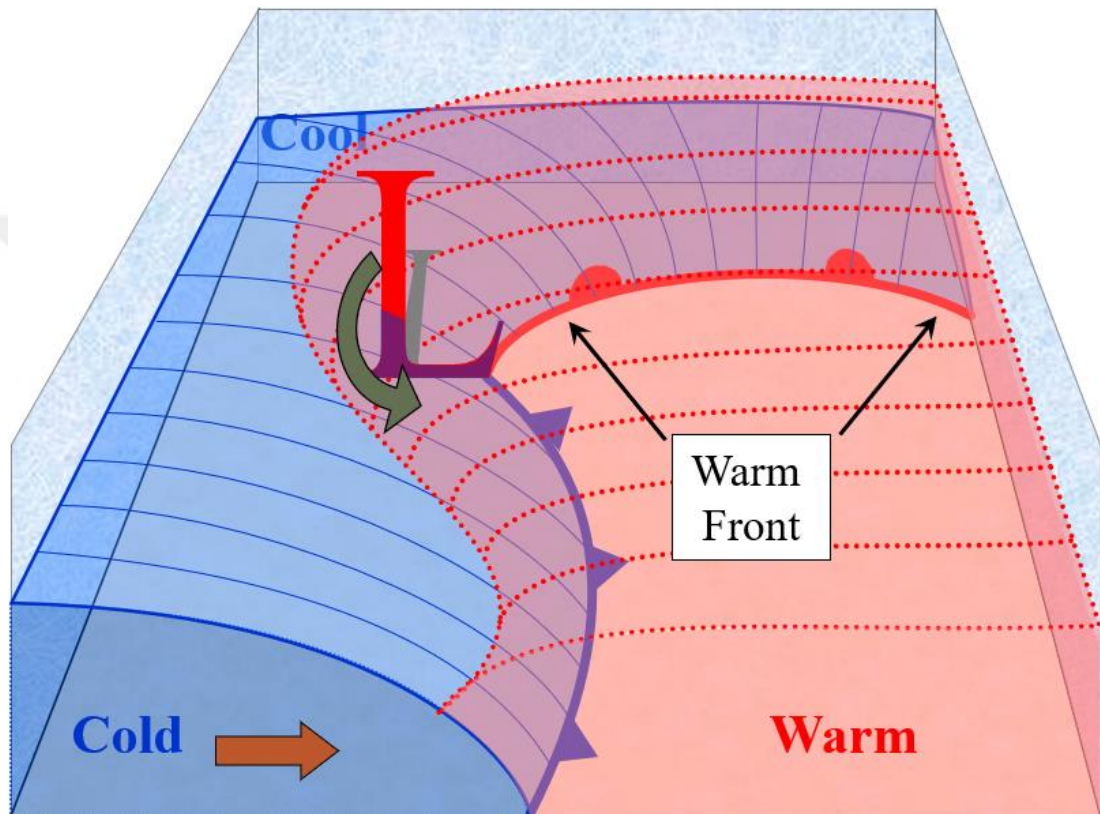


Figure 1.5 : 3-D Schematics of the warm and cold fronts (Mentes, 2020).

Warm fronts are positioned within larger troughs and are at the leading edge of a homogenous warm air mass that is located on the equatorward edge of the gradient in isotherms. A warm front is created when a warm, moist air mass replaces a cold, dry air mass. The shape of the front looks like a wedge. It starts out with a warm air at high altitude, and then gradually decreases in altitude until it reaches the surface. The front is often accompanied by precipitation as it nears the surface (Fig 1.6). As warm air is less dense than cold air, it's difficult for the warm air to displace the cold air mass, giving rise to the wedge shape. As a result, the warm front moves more slowly than a cold front. Cloud formations associated with an incoming warm front have a distinctive pattern that reflects the wedge shape with clouds of high altitude appearing

first, for example, cirrus clouds. This is followed by lower cloud formations, like altocumulus, and then stratus clouds. It should be emphasized that clouds ahead of the warm front are mostly stratiform, and rainfall gradually increases as the front approaches. Fog can also occur preceding a warm frontal passage (Huth, 2013).

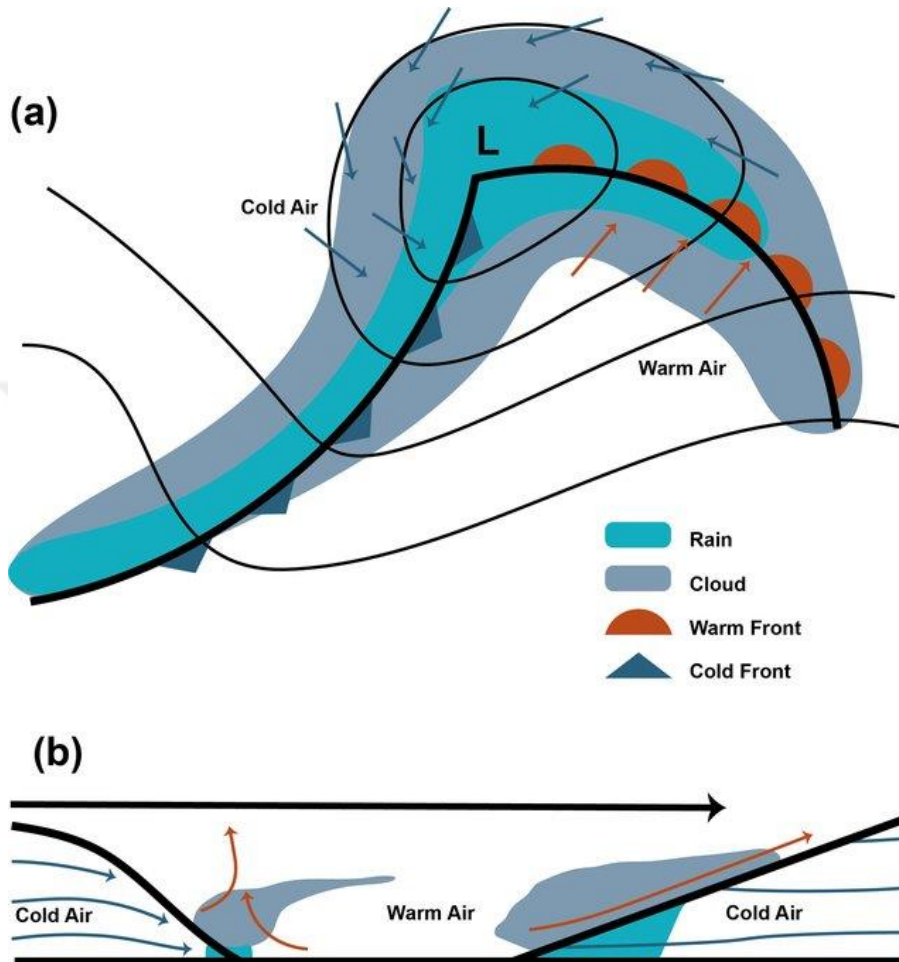


Figure 1.6 : a) indicates a planar view looking down on the system while part b) indicates a vertical cross section (Holton, 2004).

Therefore, it might be argued that squall lines or bands of thunderstorms may precede a cold front, but stratiform precipitation and fog typically immerse in a warm front before it arrives.

It is worthy of note that upward vertical motion means ascending air with the presence of convergence is at the surface level. Divergence is at the placed upper level. If downward vertical motion (Large Scale Subsidence) is occurrence of divergence at the surface level, convergence is located at the upper level. Besides, tilting of cold core can be considered as a reason of pressure displacements (Fig 1.7).

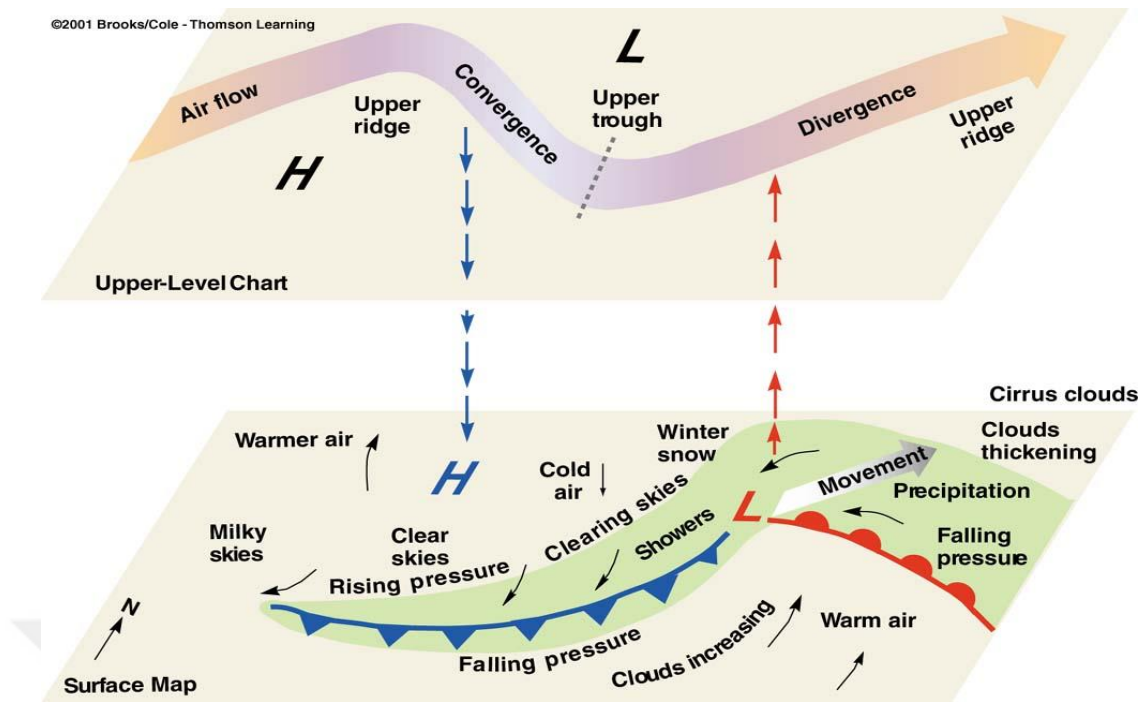


Figure 1.7 : Vertical profile of the fronts (Ahrens, 2001).

In brief, schematics of the cold fronts generally move from west to east, whereas warm fronts move poleward. Occluded fronts are hybrids, whereas stationary fronts are stagnant. Cold fronts and occlusions migrate more quickly than warm fronts and warm occlusions because the dense air behind them can both lift and push the warmer air. In terms of vertical structure of the wind direction, there is a backing wind mechanism in cold sector, and veering wind mechanism in warm sector, typically (Holton, 2004).

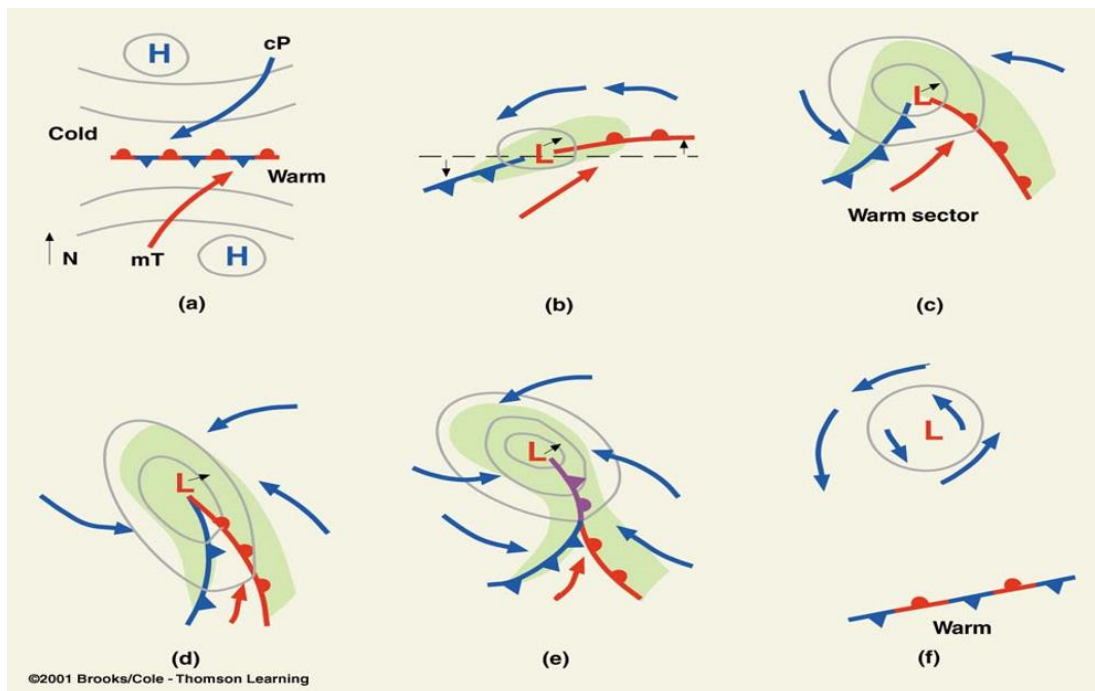


Figure 1.8 : The idealized life cycle of a wave cyclone in six steps by Norwegian Cyclone Model. (a) Stationary (b) Frontal Wave (c) Open Wave (d) Mature (Initial Occlusion) (e) Advanced Occlusion (f) Cut-off cyclone (Ahrens, 2001).

1.1.1.2 Stationary fronts

There are two other main types of fronts named as occluded and stationary fronts. A stationary front is a boundary between warm and cold air masses that doesn't move or moves very slowly (Fig 1.9). For example, a weak cold air mass may not have enough power to push away a warm air mass. There may be extended periods of cloudy weather and periodic rain, possibly for days on end. Sometimes, however, intense localized storms can arise from stationary fronts. Eventually, one of the air masses displaces the other or another air mass comes along (Lackmann, 2011).

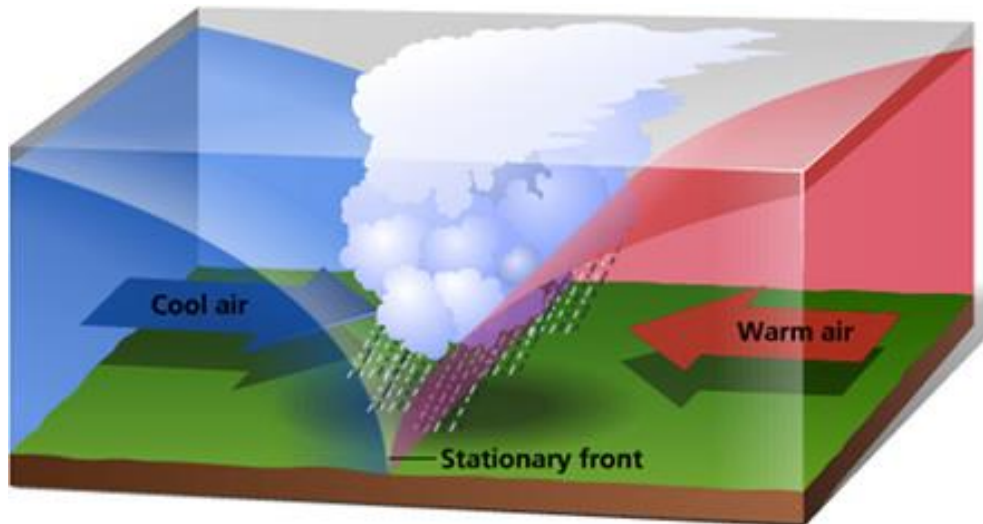


Figure 1.9 : The depiction of stationary fronts (Mentes, 2020).

1.1.1.3 Occluded fronts

These fronts typical variants of cold and warm fronts. Cold fronts move faster than warm fronts, because the higher density of the cold air allows it to readily displace warm air. Every so often, a cold air mass will move so fast that it overruns a warm air mass and connects to another cold front ahead of it. The fast-moving second cold air mass in the west pushes the warm air mass upward and physically connects to the eastern cold air mass (Huth, 2013). The warm air mass occupies a trough between two cold air masses. This creates a situation called an occluded front. As the warm, moist air gets pushed upward, it cools, often resulting in rain or snow. Occasionally, the occluded front is associated with rotation around a low-pressure region known as a cyclone. Since an occluded front is formed with a warm front high up and a cold front overrunning it, the signs of an occluded front look like a combination of both cold and warm fronts (Fig. 1.10)

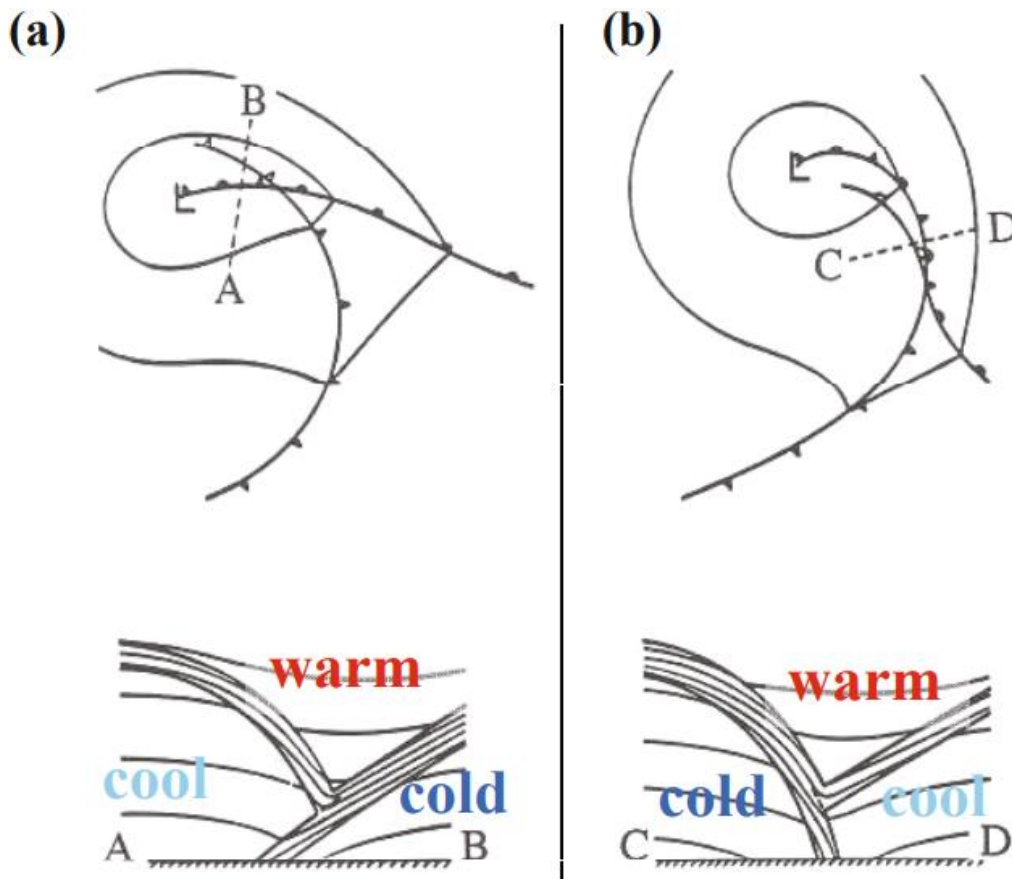


Figure 1.10 : Cross sectional views of warm-occluded (left) and cold-occluded (right) (Lackmann, 2011).

Sometimes, the towering cumulus clouds overshoot the tropopause and develop an anvil head structure. In either case, it can be expected precipitation and possibly lightning. After the occluded front passes, the wind shifts into the west like the passing of a cold front (Fig 1.11). Clouds dissipate, and can be anticipated clear blue skies. Occluded fronts move with the speed of the second cold airmass, which can vary between 15 to 25 miles per hour, or 25 to 40 kilometers per hour (Holton, 2004).

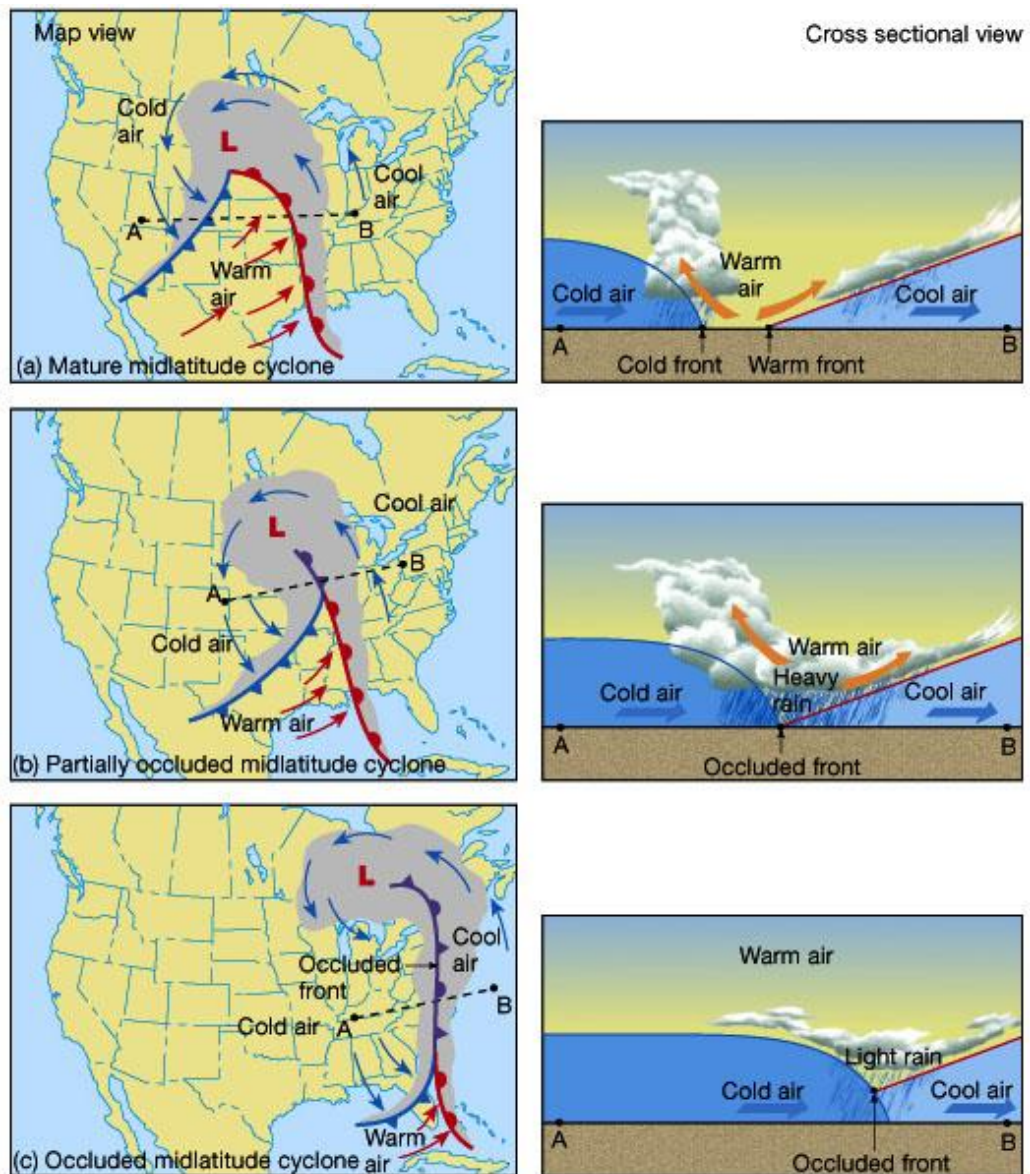


Figure 1.11 : Cross sectional view of the cold-occluded front (Mentes, 2020).

There are two other sub-types of fronts named as coastal and middle-upper fronts. These fronts form in place along the zone of strong temperature contrast between land and water and can play an important role in a variety of weather phenomena (Lackmann, 2011). The mechanisms that favor the development of coastal fronts are in part related to the gradient in surface properties found at the coastline. Cool air damming should be presented on the left side in Fig. 1.12 (left). Intense frontal zones are not only found at the surface; observational and theoretical studies have documented the formation of strong fronts near the tropopause as well

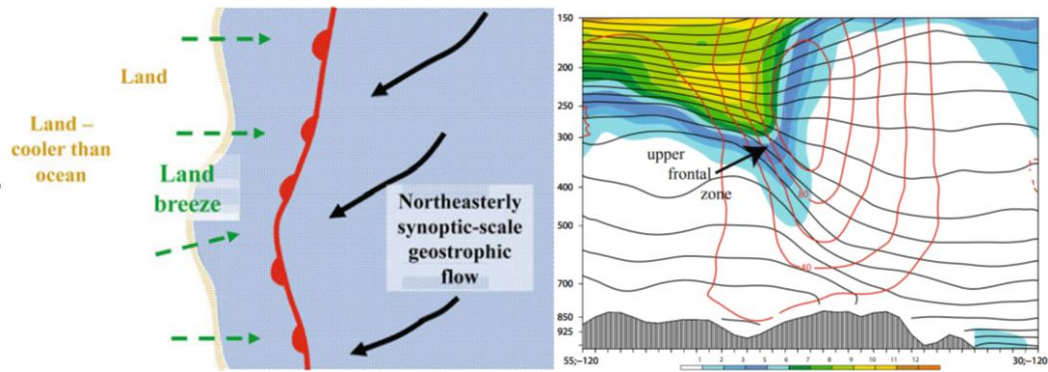


Figure 1.12 : Idealized depiction of a coastal front along a north– south-oriented coastline. Green dashed arrows indicate the near-surface flow associated with a land-breeze circulation; black solid arrows represent a synoptic-scale northeasterly flow (left). North–south cross section through an upper-level jet-front system, based on a short-term NAM forecast valid 18 UTC 25 Aug 2004. PV (shaded as in legend at bottom of panel), isentropes (black solid contours every 5K), and isotachs (red contours every 20 kt) (right) (Lackmann, 2011).

1.2.3 Inclination of fronts & margules model

In this section, it will be discussed inclination of fronts & Margules Model with their kinematic properties of surrounding air in the vicinity of the atmospheric fronts. First of all, we need to understand the near surface wind vectors. The rotated front-relative axes are significant in Fig 1.13.

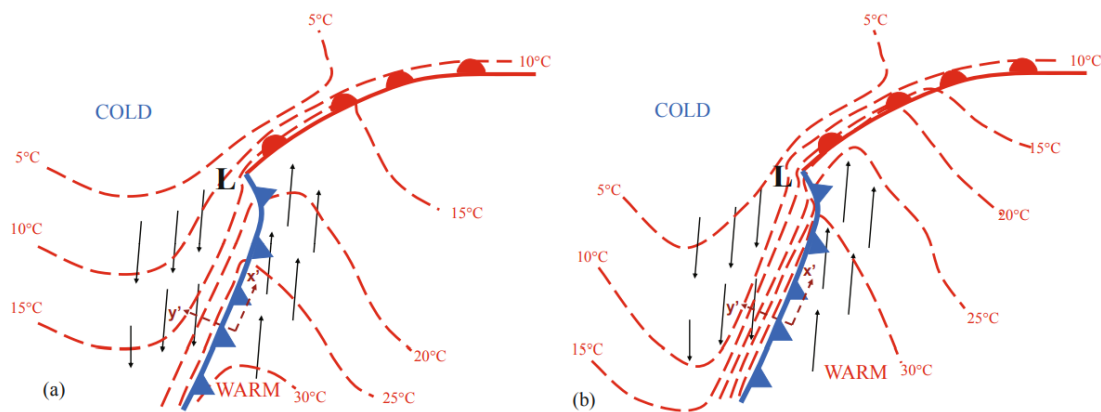


Figure 1.13 : Idealized horizontal plot of near-surface wind vectors (black arrows), isotherms (red dashed contours), and frontal zones for (a) initial time, and (b) the same front-relative view at a later time (24 h later). The rotated front-relative coordinate axes are shown.

It should be emphasized that there is prominent wind shear mechanism from surface to upper layers as veering and backing in Fig. 1.14.

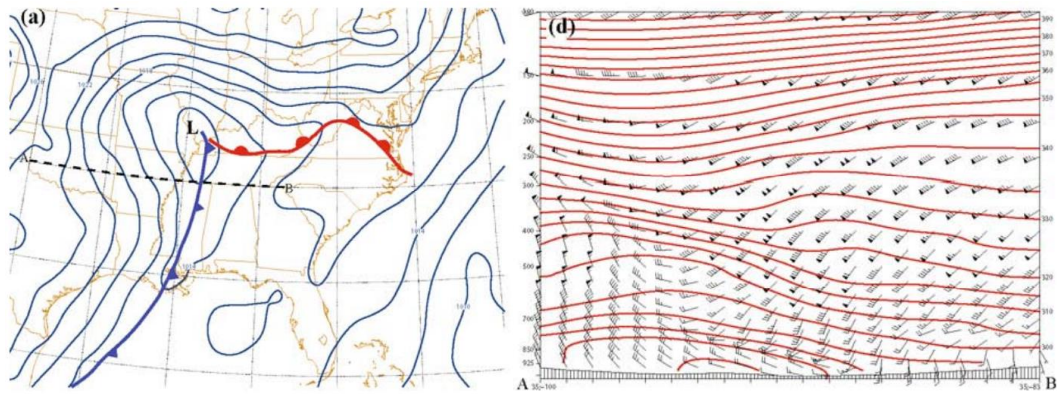


Figure 1.14 : Diagnostic summary for 0000 UTC 17 Nov 2009, based on North American Mesoscale (NAM) analysis: (a) sea level pressure and subjective frontal analysis, bold line shows orientation of cross section shown in (d); (d) cross section of wind and potential temperature (interval 5K, red contours); orientation shown in (a) (Lackmann, 2011).

As similar, this is a different frontal structure, it is obviously seen the circulation in Fig 1.15. Cold front pushes down to surface.

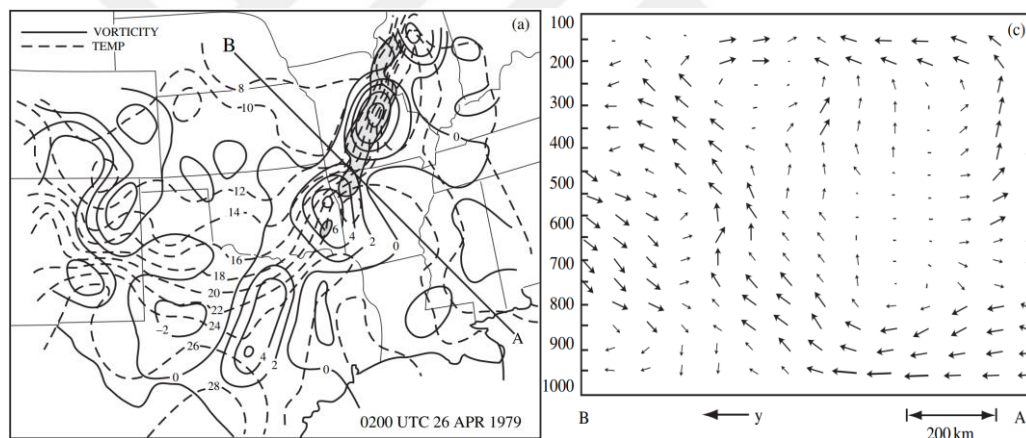


Figure 1.15 : Frontal structure as depicted by a front analyzed for 0200 UTC April 26, 1979: (a) Surface temperature (8C, dashed), relative vorticity (contour interval $2 \times 10^{-5} \text{ s}^{-1}$, solid). Radar echoes at 0235 UTC April 26, 1979 are shaded. (c) Transverse circulation relative to the movement of the front (Adapted after Ogura and Poris 1982).

To illustrate inclination of frontal boundary, Margules Model, there is a prominent plot in Fig. 1.16.

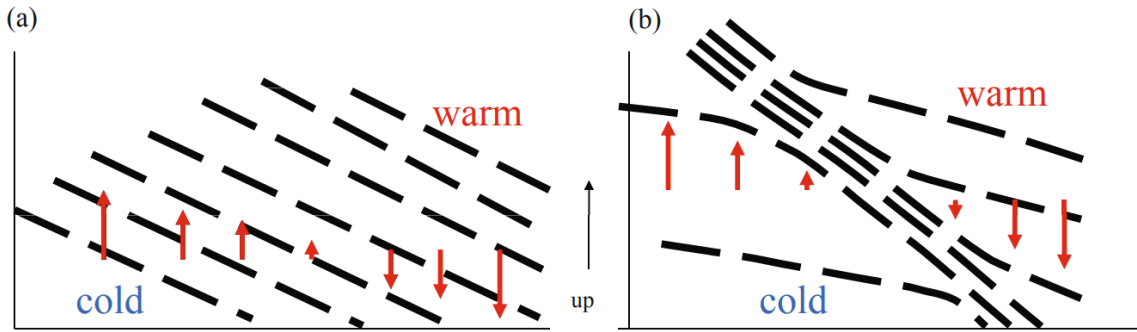


Figure 1.16 : Idealized cross-sectional diagrams demonstrating frontogenetical tilting. Dashed lines are isentropes and red arrows represent vertical motion for (a) an initial time and (b) a later time (Lin, 2007).

$$\tan a = \frac{f\bar{T}}{g} \left(\frac{v - v'}{T' - T} \right) \quad (1.1)$$

$$\frac{dz}{dy} \approx \left(\frac{f\bar{T}}{g} \right) \left(\frac{u_{gw} - u_{gc}}{T_w - T_c} \right) \quad (1.2)$$

- Coriolis force: f
- Mean temperature: \bar{T}
- Geostrophic wind diff.: ΔU
- Gravitational acceleration: g
- Temperature diff. of air masses: ΔT

It can be derived the final form of Margules Model Equation in Eq. 1.2. In meteorology, density is not measured, the Eq. 1.1 and Eq. 1.2 can be expressed in terms of temperature using the equation of state as follows. As can be seen from Eq. 1.1 and Eq. 1.2, the slope of a front is directly proportional to the wind discontinuity and the reversely proportional with temperature discontinuity. The average slope of a front is around 1/150, with 1/50 being quite steep as in cold fronts and 1/300 is considered a weak slope in warm fronts (Fig. 1.17) (Penn State, n.d.).

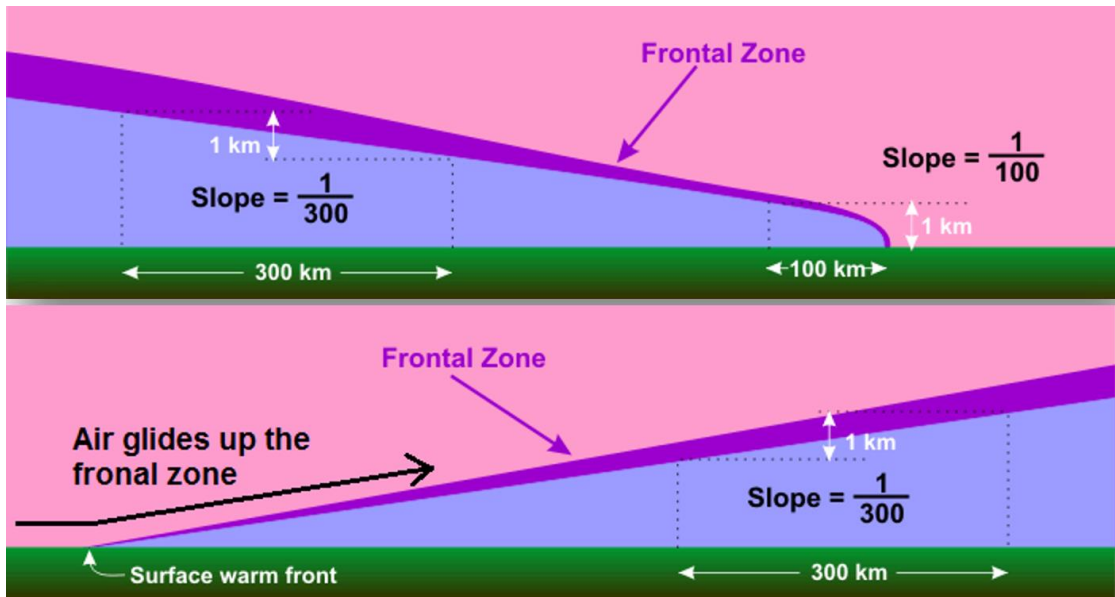


Figure 1.17 : Typical inclination of atmospheric cold (top) and warm (bottom) fronts (Penn State, n.d.).

1.1.1.4 Cross-frontal circulations and Q-vector

In other words, the frontogenesis produces a direct transverse, ageostrophic, secondary circulation in the Y–Z plane by a convergent deformation basic flow in time (Fig 1.18 and Fig 1.19).

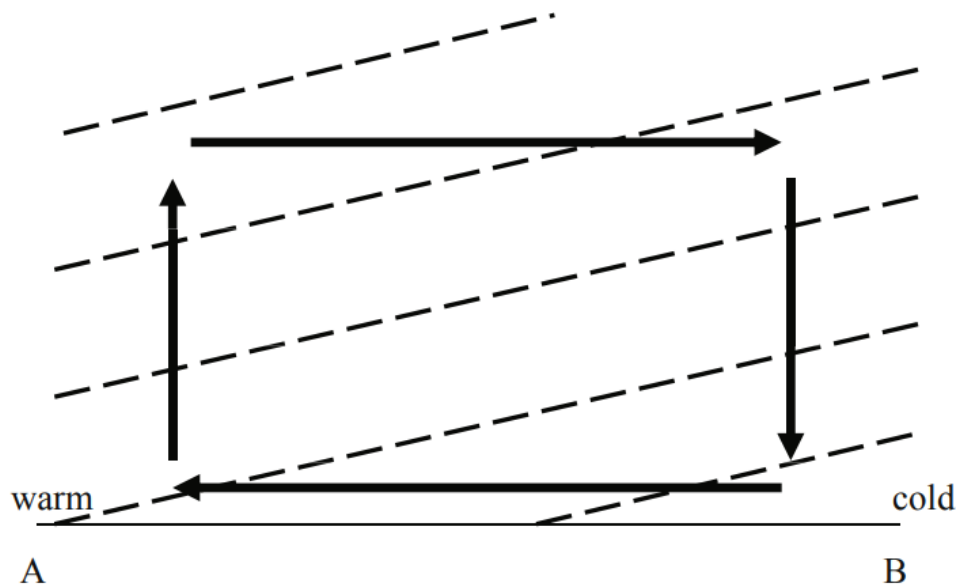


Figure 1.18 : Schematic cross section of isentropes (dashed sloped lines) and ageostrophic circulation (thick arrows) (Lackmann, 2011).

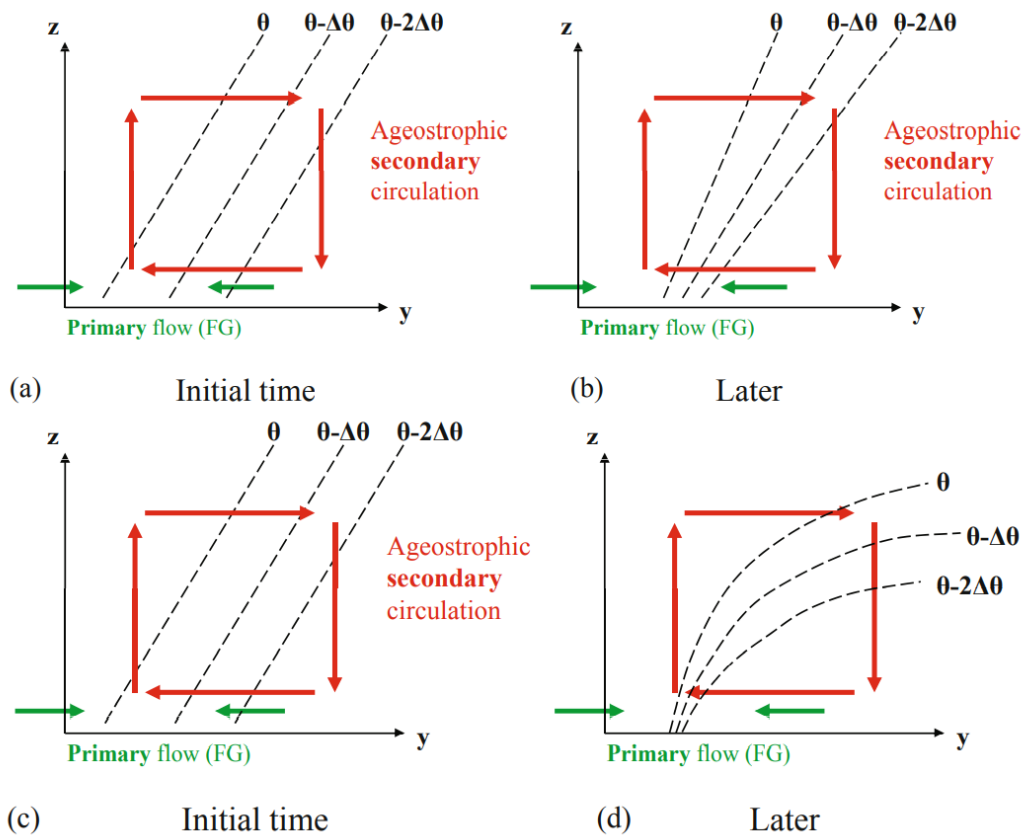


Figure 1.19 : Idealized comparison of (a),(b) quasigeostrophic frontogenesis with (c),(d) semigeostrophic frontogenesis. Green arrows show primary geostrophic flow, red arrows represent ageostrophic frontal circulation, and dashed black lines are isentropes. Adapted from Bluestein (1986). Warm air mass (left), cold air mass (right) (Lackmann, 2011).

In the meteorology literature, there are several evaluating and interpreting methods for vertical motion as in the following (Steenburgh, n.d.): Kinematic method, Raw model vertical velocity, Omega equation, and Q-vectors. Based on Quasi-Geostrophic Equation, Q-Vector eliminates term cancellation and multi-level problems posed by traditional omega equation and can be used to identify the vertical motion on maps.

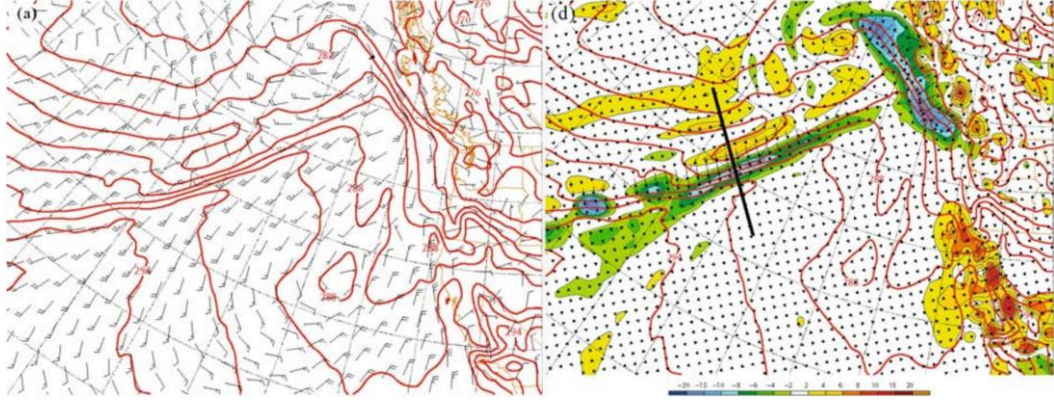


Figure 1.20 : Diagnosis of North Pacific front with GFS analysis valid 1200 UTC 14 Nov 2008: (a) 10-m wind barbs, 1000-mb isentropes (red, interval is 2 K); (d) as in (a), but with 850-mb omega (contour interval is $2 \times 10^{-2} \text{Pa s}^{-1}$, dashed for ascent, solid for descent, and shaded as in legend).

As interpretation, it can be reminded that ascending air means movement of vertical velocity (w) is positive in z system and vice versa, descending air indicates the movement of vertical velocity (w) is negative in z system.

$$\left[\nabla^2 + \frac{f_0^2}{\sigma} \frac{\partial^2}{\partial p^2} \right] \omega \sim -\omega \propto w \quad (1.3)$$

So that,

$$w \propto -\omega \propto -2\nabla \cdot \vec{Q} \propto -\nabla \cdot \vec{Q} \quad (1.4)$$

- Q-vector convergence ($\nabla \cdot \vec{Q} < 0$) is associated with rising motion ($w > 0$). (Fig. 1.21)
- Q-vector divergence ($\nabla \cdot \vec{Q} > 0$) is associated with sinking motion ($w < 0$). (Fig. 1.21)

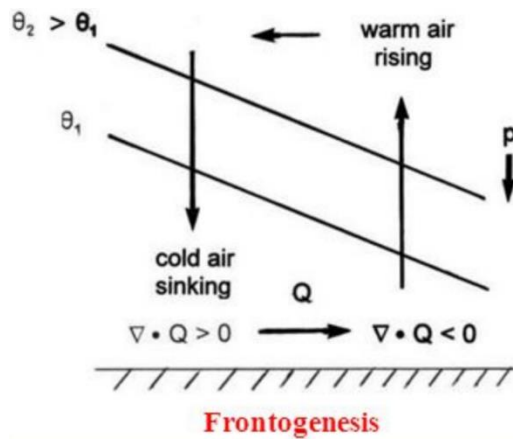


Figure 1.21 : Vertical view of Q-Vector in Frontogenesis (Steenburgh, n.d.).

Ageostrophic flow creates 'frontolysis' if the Q-vector points toward cold air and crosses the temperature gradient (Steenburgh, n.d.).

The converging Q-vectors suggest rising (or sinking) motion should occur to the east of troughs (or ridges) and surface cyclones (or anticyclones). Q-vectors are oriented parallel to the ageostrophic wind vector (Fig 1.22). In addition, Q-vectors are proportional to the magnitude of the ageostrophic wind (Bluestein, 1993).

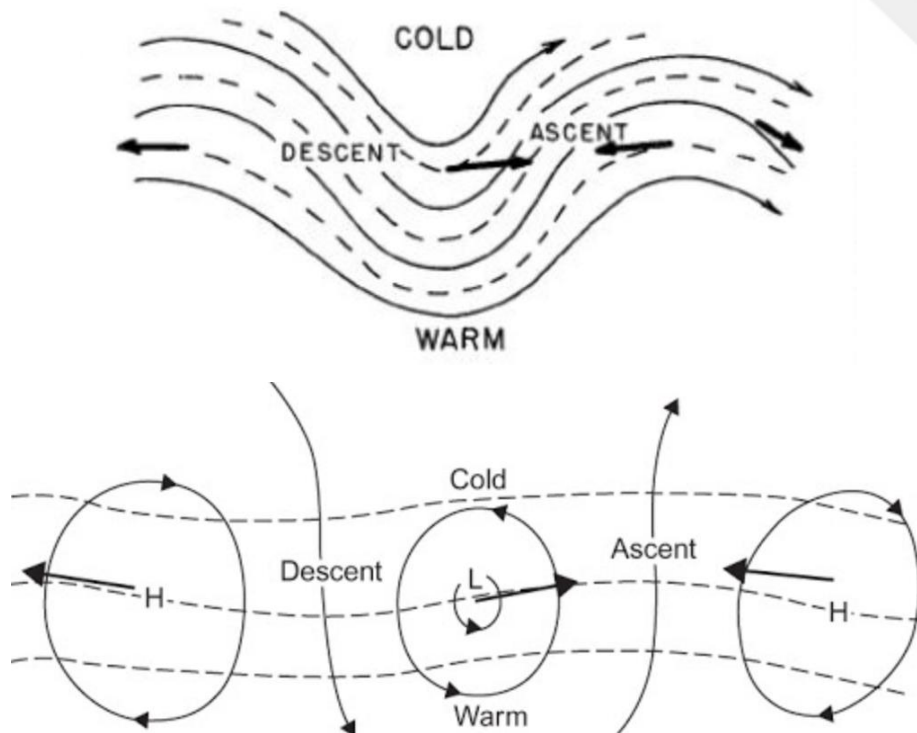


Figure 1.22 : Q-Vector Analysis on upper level systems (top) and surface systems (bottom) (Bluestein, 1993).

The frontogenetical action of the secondary frontal circulation near the surface leads to the formation of very sharp horizontal discontinuities there, limited only by mixing due to turbulence in the frontal zone (Fig 1.23).

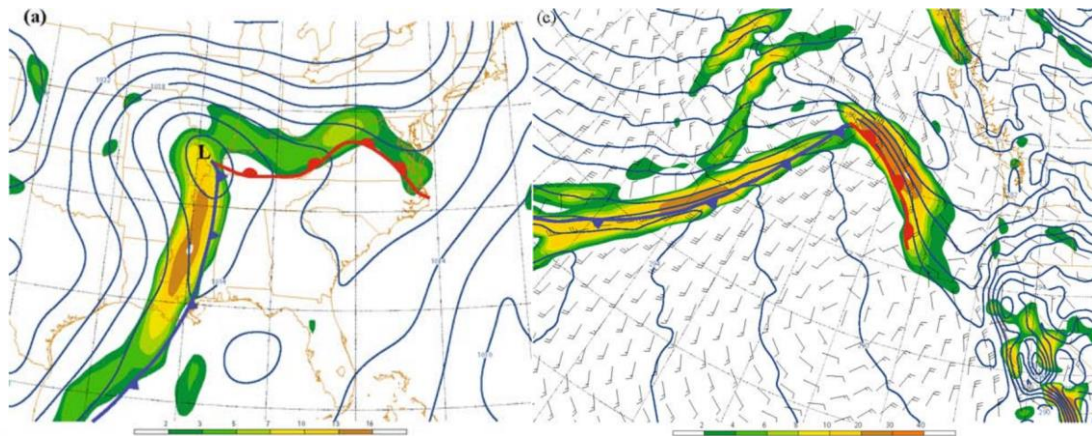


Figure 1.23 : Examples of near-surface horizontal frontogenesis function (shear and confluence terms): (a) sea level pressure, subjectively analyzed fronts, and frontogenesis (shaded as in legend, beginning at $3 \text{ K (100 km)}^{-1} (3 \text{ h})^{-1}$) (c) 10-m wind (barbs) and 1000-mb potential temperature and frontogenesis (shaded as in legend) from Global Forecast System (GFS) analysis valid 0000 UTC 14 Nov 2008 (Lackmann, 2011).

1.2.4 Assessment of mesoscale convective systems including supercell tornadic storms & connection with weather fronts

As one of the main phenomena in severe weather in meteorology, thunderstorms are the most common source of hazardous weather at local scales which should be profoundly concerned. They are defined as one or more sudden electrical discharges, manifested by a flash of light (lightning) and a sharp or rumbling sound (thunder).

Economic loss of thunderstorms has been increasing in the last decade in Europe shown in Fig. 1.24. The most frequent location for thunderstorms to form and develop is in the mid-latitude region, where warm, moist air from tropical latitudes collides with cooler air from polar areas and They are the driving force behind the growth and development of a wide variety of severe weather occurrences. There is a high risk of injury associated with thunderstorms and the phenomena that occur with them. The majority of the damage that occurs as a consequence of thunderstorms is brought about by downburst winds, huge hailstones, and flash flooding brought about by excessive precipitation. Storm cells that are more vigorous have a greater likelihood of generating tornadoes and waterspouts.

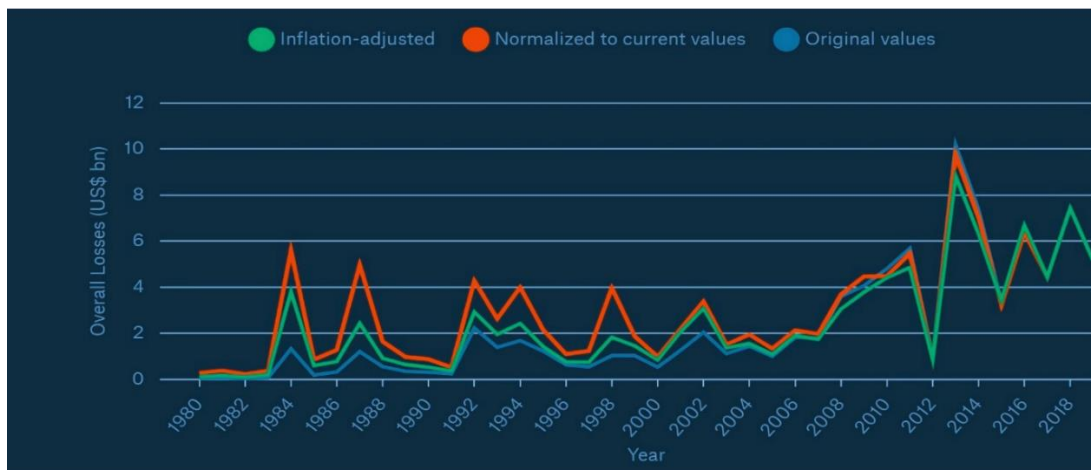


Figure 1.24 : Normalized losses from thunderstorms have increased in Europe (WMO, 2021).

They occur in a type of cloud known as a cumulonimbus and usually accompanied by strong winds and often produce heavy rain and sometimes snow, sleet, or hail, but some thunderstorms produce little precipitation or no precipitation at all (Kridler, 2020). Squall lines are formed when a line of thunderstorms or a band of rain develops and becomes known as a squall line. Large hail, high winds, and tornadoes are only a few of the potentially life-threatening meteorological events that can be brought on by intense or severe thunderstorms. Supercell thunderstorms, which are a group of the most persistent and intense storms, rotate in a similar way that cyclones do. With all this importance and damage power, it is necessary to classify Thunderstorms in detail in the scope of spatial scale of radar echo, shear environment, and expected storm type (Fig. 1.25). These clusters of thunderstorms, which are commonly refer to as MCSs, are greater in scale than single storms but on a smaller scale than low-pressure systems with cold and warm fronts.

Determining Thunderstorm Classification

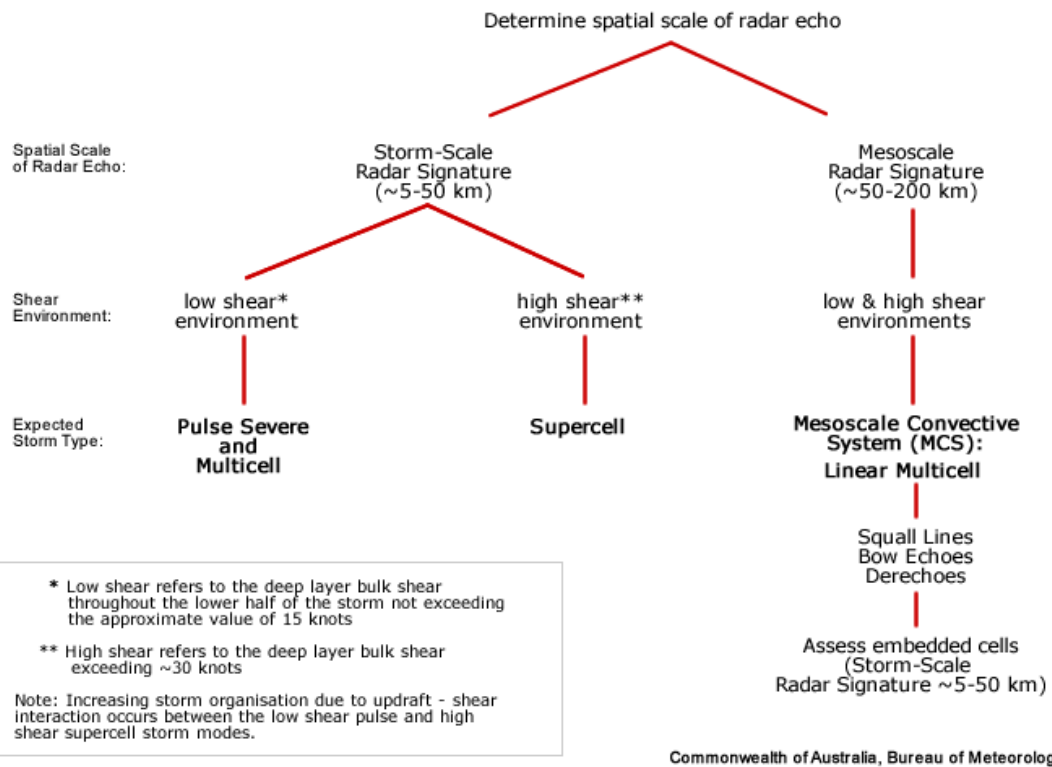


Figure 1.25 : Determining thunderstorm classification (Commonwealth of Australia, Bureau of Meteorology, n.d.).

Any MCS is composed of a contiguous area of precipitation that is 100 km or greater across in at least one spatial dimension (Bluestein, 2013). It is apparent from radar or satellite imagery of convective precipitation, especially when the anvil is very large. MCSs include both isolated/amorphous complexes of convective storms and squall lines (lines of deep convective cells), some of which are relatively long, but very narrow, perhaps as long as 100 km or more and as narrow as 10 km or less. MCSs undergo evolution in which both their mode of organization and spatial scale change with time. The individual convective cells that make up at least part of a MCS are considered to be its building blocks. The building blocks may be ordinary cells or supercells. MCSs composed of ordinary cells are sometimes referred to as “multicell” complexes, but the latter term could also include regions of precipitation too small to be considered MCSs. They have different sorts of mesoscale signatures on radar (Fig. 1.26).

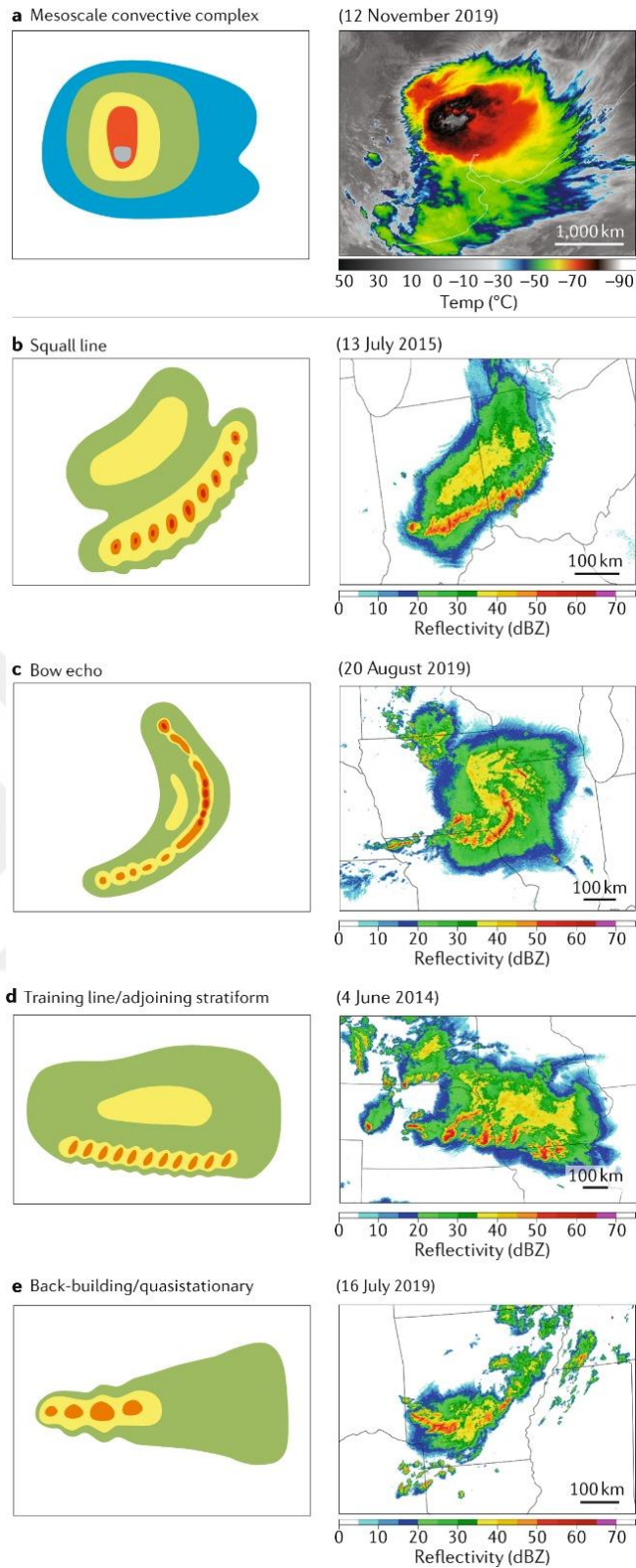


Figure 1.26 : Mesoscale radar signatures of storm cells (Schumacher & Rasmussen, 2020).

Moreover, a highly particular type of organized convection is a bow echo can be seen in Fig. 1.27. Bow echoes and supercells share potential for development of vortices and tornadoes (Goulet, 2015). These tornadoes can occur near of low level meso vortex or the triple point within the frontal structure located at north of the bow apex (Fig. 1.27). However, they tend to be weaker and shorter-lived on average than those associated with supercell thunderstorms.

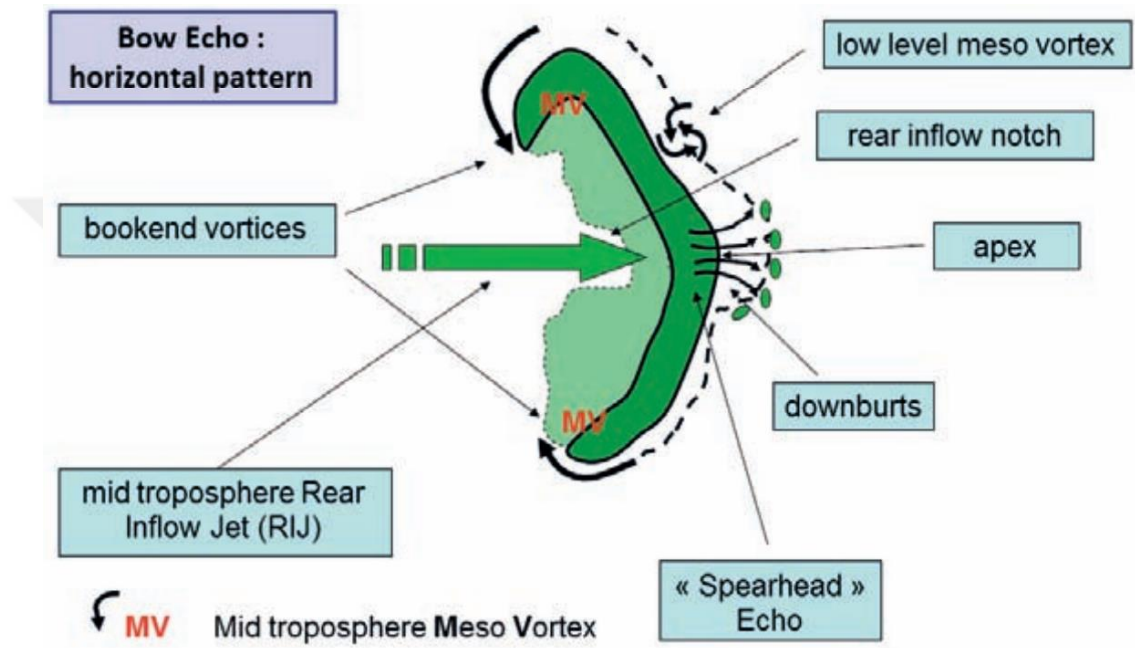


Figure 1.27 : Typical horizontal pattern of a bow echo (Goulet, 2015).

From meso-scale weather phenomena containing vortices such as tornadoes, we can write the definition of the supercell as follows using the Glossary of Meteorology (AMS, 2012) is that “An often dangerous convective storm that consists primarily of a single, quasi-steady rotating updraft, which persists for a period of time much longer than it takes an air parcel to rise from the base of the updraft to its summit (often much longer than 10–20 min). Most rotating updrafts are characterized by cyclonic vorticity (Fig. 1.28). The supercell typically has a very organized internal structure that enables it to propagate continuously. It may exist for several hours and usually forms in an environment with strong vertical wind shear.”

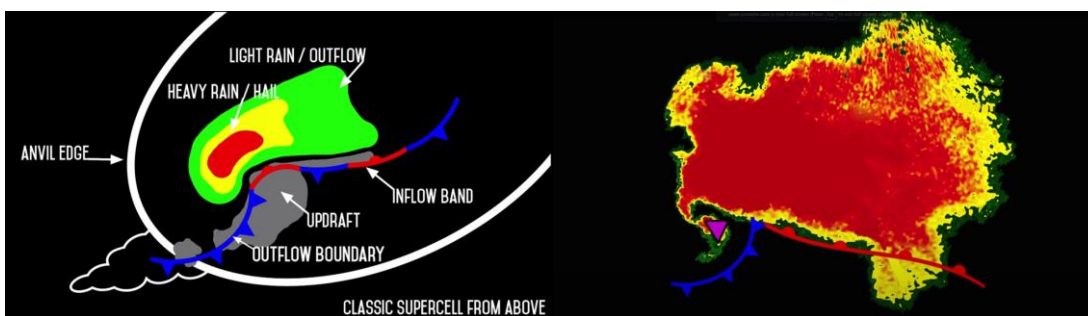
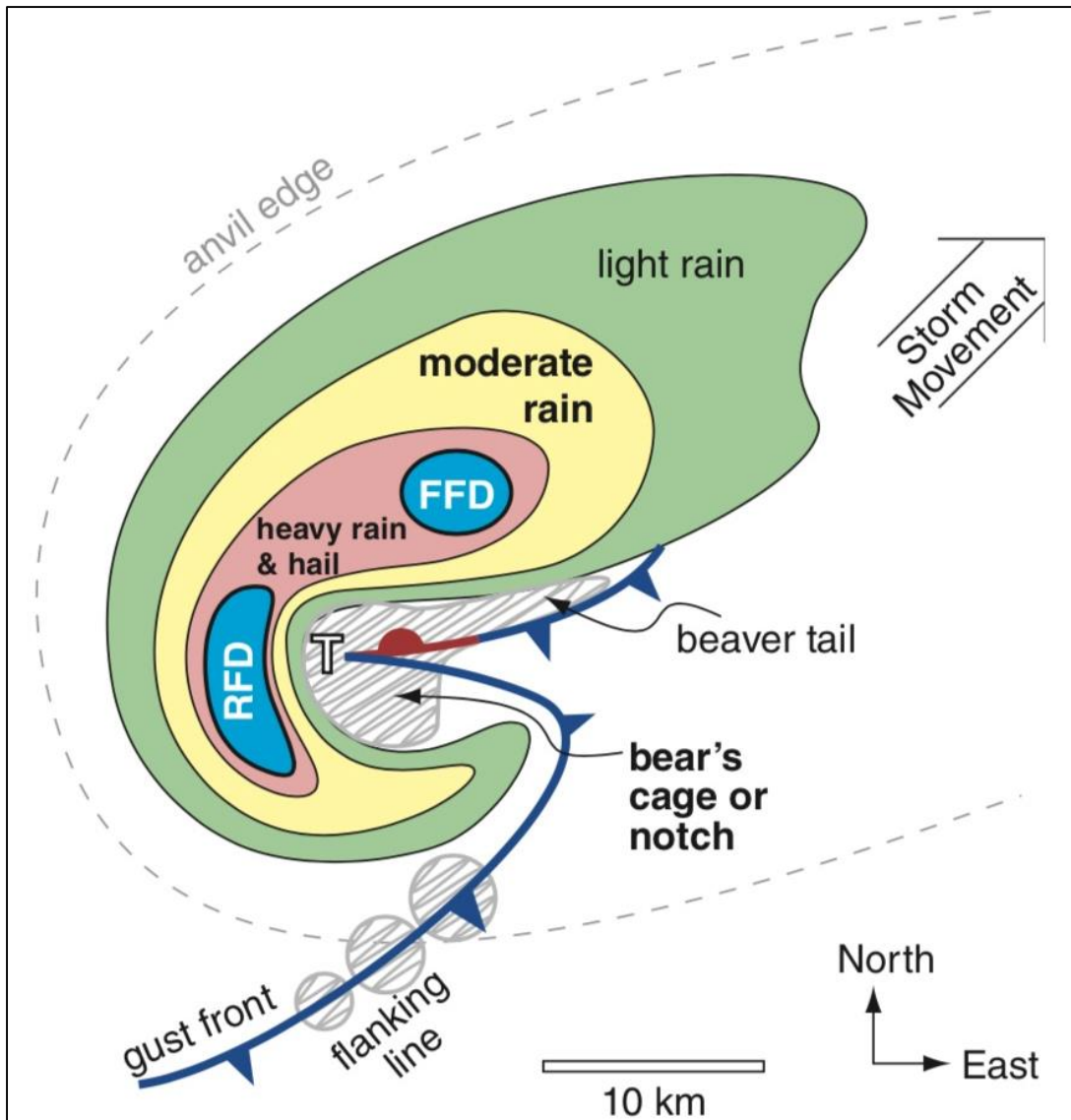


Figure 1.28 : Typical supercell structure (top) (Stull, 2015). Tornado location in near-fronts and typical supercell (bottom left), radar reflectivity data relation with supercell and fronts (bottom right) (Weingart, 2016).

Supercells may be embedded within MCSs and also coexist with multicells. The typical radar signature of supercells consists of Rear Flank Downdraft (RFD), updraft, Forward Flank Downdraft (FFD) and the presence of hook echo (Fig. 1.28; Fig 1.29). According to these placements, the mesocyclone can be identified with the

contribution of local fronts and secondary winds around the front intersection. One out of four supercells around the world approximately can culminate by occurrence of a tornado (Trapp et al. 2005). Portions of some MCSs during parts of their life may be composed of both a broken line or solid line or a solid line of convective cells and (a broader region of) strati-form precipitation. In parts of the US., a relatively large fraction of the annual precipitation falls in MCSs. Since Doppler radar observations and three-dimensional non-hydrostatic numerical cloud models have become available, the major aspects of MCSs may be explained at least qualitatively.

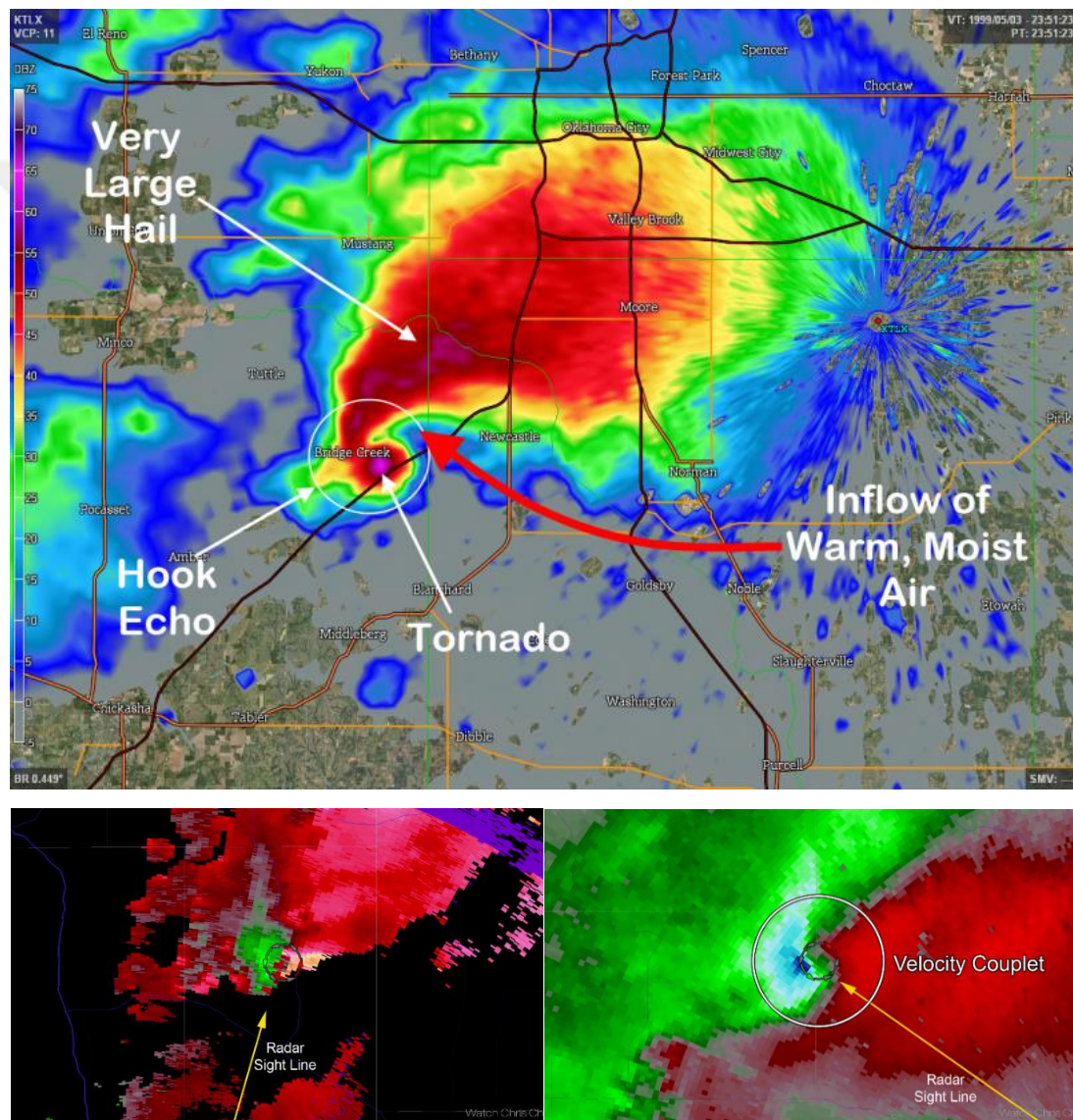


Figure 1.29 : Radar Detection of a mesocyclone by reflectivity data (dBZ) dragging by supercell storm (top) and velocity data retrieved through radar sight line (bottom left/right) (Watch Chris Chase, 2019).

Supercell thunderstorm forecasting and detection could be discussed, in light of the disastrous weather events that often accompany supercells. Characteristically,

supercells or other thunderstorm types such as derechos, bow echos or squall lines could be interpreted as the collection and all sub-headings of the MCS or Mesoscale Convective Complex (MCC) concept. Particularly supercells, which are capable of producing high winds, flash floods, large hail, and strong, long-lived tornadoes.

1.2.5 Characteristics, types and severity of tornadoes

The definition of a tornado in the Glossary of Meteorology (AMS, 2003) begins with the following: “A rotating narrow column of air, in contact with the surface, pendant from a cumuliform cloud, and often visible as a funnel cloud and/or circulating debris/dust at the ground.” The tornado is averaging about 100-m to 1-km in diameter, pendant from convective clouds (Bluestein, 2013). It typically extends to the ground from the interior of a cumulonimbus (or occasionally a cumulus congestus) cloud and appears as a condensation funnel pendant from cloud base and/or as a swirling cloud of dust and debris rising from the ground (Edwards, 2006). Significant damage can occur at the ground even when the condensation funnel does not reach the surface. A condensation funnel associated with a tornadic vortex that fails to contact the ground is called a funnel cloud. The tornado in these storms typically have life spans of approximately 10 minutes (Wicker and Wilhelmson, 1995).

Waterspouts are tornadoes that characterized by a spiraling funnel-shaped wind current, connecting to a large cumulus or cumulonimbus cloud. They are described as in general, any tornado over a body of water (AMS, 2012). Apart from various types of tornadoes include the multiple vortex tornado, landspout, and waterspout; other types of twisters (vortices) are not connected with a cloud base such as gustnado, dust devil, fire whirl, whirlwind, steam devils.

The minimum wind speed in tornadoes is generally that considered high enough to sustain devastation. In the absence of direct measurements, tornado wind speeds are estimated from damage using the enhanced Fujita scale (EF) (Marshall, 2004) and supplemented when possible by data from mobile Doppler radars (Snyder & Bluestein, 2014).

The Fujita scale or Fujita–Pearson scale (FPP measure) is a rating metric for assessing tornado strength based mostly on that tornadoes inflict to constructions and plants (Fujita, 1971). The EF, which became operational on February 1, 2007, is used to assign a tornado a 'rating' based on estimated wind speeds and related damage. The

new scale considers construction quality and standardizes various types of structures. Meteorologists and engineers deemed the wind speeds on the original scale to be excessively high, and engineering studies revealed that slower winds than initially estimated cause the respective degrees of damage (Table 1.1; Fig. 1.30). The old scale defines an F5 tornado as having wind speeds of 261-318 mph (420-512 km/h), whereas the new scale defines an EF5 tornado as having winds greater than 200 mph (322 km/h), which were found to be sufficient to cause the damage previously attributed to the F5 range of wind speeds. An "EF-Unknown" (EFU) category was later added for tornadoes that cannot be rated due to a lack of damage evidence. Tornadoes ranked EF4 and EF5 on the Enhanced Fujita scale that exhibit long paths are the least common but most damaging and deadly type of tornado (Orf et al. 2017).

Table 1.1 : A comparison of the Fujita scale with the enhanced Fujita scale (SPC 2009; SPC 2021).

| Fujita Scale | Wind Speed (ms-1) | Wind Speed (kmh-1) | Frequency | Potential Damage Description | Enhanced Fujita Scale | Wind Speed (mph) | Wind Speed (kmh) | Frequency | Potential Damage Description |
|--------------|-------------------|--------------------|-----------|------------------------------|-----------------------|------------------|------------------|-----------|------------------------------|
| - | - | - | - | - | EFU | N/A | N/A | 3.11% | No surveyable damage |
| F0 | 18–32 | 64–116 | 44.14% | Light damage | EF0 | 29–38 | 105–137 | 52.82% | Minor damage |
| F1 | 33–50 | 117–180 | 34.24% | Moderate damage | EF1 | 38–49 | 138–177 | 32.98% | Moderate damage |
| F2 | 51–70 | 181–253 | 16.17% | Significant damage | EF2 | 50–60 | 178–217 | 8.41% | Considerable damage |
| F3 | 71–92 | 254–332 | 4.35% | Significant damage | EF3 | 61–74 | 218–266 | 2.18% | Severe damage |
| F4 | 93–116 | 333–418 | 1.00% | Devastating damage | EF4 | 75–90 | 267–322 | 0.46% | Devastating damage |
| F5 | 117–143 | 419–512 | 0.10% | Incredible damage | EF5 | >90 | >322 | 0.05% | Incredible damage |

| T0 | T1 | T2 | T3 | T4 | T5 | T6 | T7 | T8 | T9 | T10 | T11 |
|-----------|----|-----------|----|-------------|----|-----------|----|-----------|----|-----------|-----|
| F0 EF0 | | F1 EF1 | | F2 EF2 | | F3 EF3 | | F4 EF4 | | F5 EF5 | |
| Weak | | | | Strong | | | | Violent | | | |
| | | | | Significant | | | | | | | |
| | | | | | | Intense | | | | | |

Figure 1.30 : Tornado rating classifications of NOAA's SPC and are used by the NWS.

1.2.6 Formation tornado vortex: tornadogenesis

Tornadoes are frequently formed by a type of thunderstorm known as a supercell. Mesocyclones are areas of organized rotation a few kilometers/miles up in the atmosphere that are typically 1.6-9.7 km across. Hence, supercells contain mesocyclones and produce the most powerful tornadoes (EF3 to EF5 on the Enhanced Fujita Scale). Tornadoes are common in such storms, as are heavy rain, frequent lightning, strong wind gusts, and hail. Most supercell tornadoes have a predictable life cycle that begins when increasing rainfall drags an area of rapidly descending air known as the RFD with it. This downdraft accelerates as it approaches the ground, dragging the supercell's rotating mesocyclone with it. An example mesocyclonic tornado over land in US can be found in Fig. 1.31.



Figure 1.31 : A visible mesocyclone and a F3 tornado in Alabama, US (Sutter, 2017).

As the mesocyclone moves downward below the cloud base, it begins to capture cool, moist air from the storm's downdraft region. The convergence of warm air in the updraft and cool air results in the formation of a rotating wall cloud. The RFD also focuses the base of the mesocyclone, causing it to draw air from a smaller and smaller area on the ground. As the updraft intensifies, it prominently creates a low-pressure

zone near the surface. This compelled the focused mesocyclone downward, creating a visible condensation funnel. The RFD reaches the ground as the funnel descends, fanning outward and creating a gust front that can cause severe damage a long distance away from the tornado (Howard, 2015). Mostly, the funnel cloud initiates causing damage to the surface (becoming a tornado) within a few minutes of the RFD reaching the ground.

1.2.7 Synoptic climatology of the tornadoes in Euro-Mediterranean in particular

Tornadoes occur throughout the year, and each region may experience increased tornadic potential at different times of the year. The frequency of tornadoes in the United States is closely tied with the progression of the warm season when warm and cold air masses often encounter. In spite of, occasionally seen at different months of the year due to the effects of global climate change, most of the tornadoes in the United States tend to occur from early spring to late summer.

Because a tornado is part of a SCS, and these storms occur all over the Earth, tornadoes are not limited to any specific geographic location. Wherever the atmospheric conditions are exactly right, the occurrence of a tornadic storm is possible. Some parts of the world are much more prone to tornadoes than others. The middle latitudes provide the most favorable environment for tornadogenesis. This is the zone where cold air from the polar regions collides with warmer air from the subtropics, which frequently results in the production of convective precipitation at the collision boundaries. In addition, air in the extratropics commonly flows at different speeds and directions at several levels of the troposphere, which makes the development of rotation within a storm cell quicker. The United States is at the top of the list when it pertains to the total number (counts) of tornadoes that have been recorded; on average, they have more than 1,000 each year. Canada is a distant second, with around 100 per year. Europe is also intriguing continent for occurrence of severe convective storms and tornadoes. The highest density of tornado reports is in western and central Europe (Fig. 1.32). The Mediterranean annual maximum is in autumn and winter, while regions farther north have a maximum in summer as in Fig. 1.33 and there is also strong underreporting in the Mediterranean region and Eastern Europe (Groenemeijer & Kühne, 2014).

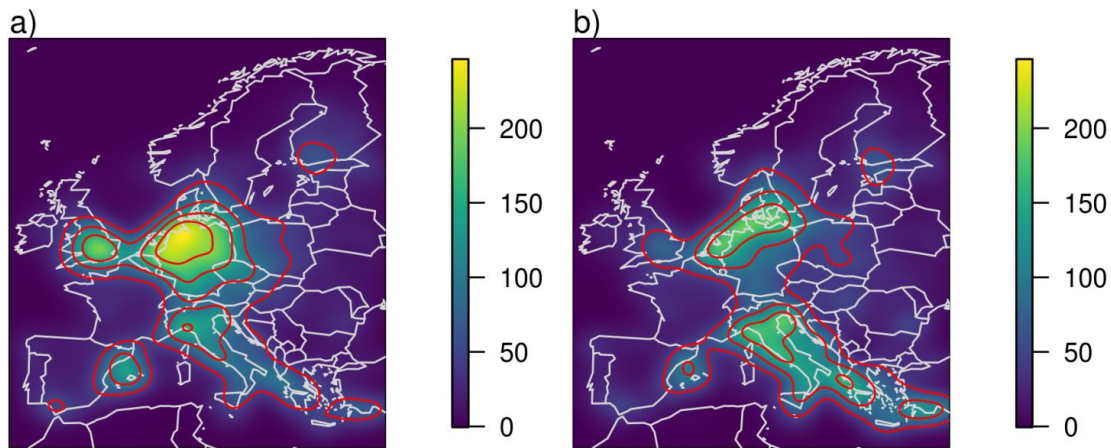


Figure 1.32 : Kernel smoothed ESWD tornado reports per 100 years and 10,000 km² based on (a) all recorded tornadoes, (b) tornadoes recorded in the period 2005–2019 (Grieser & Haines, 2021).

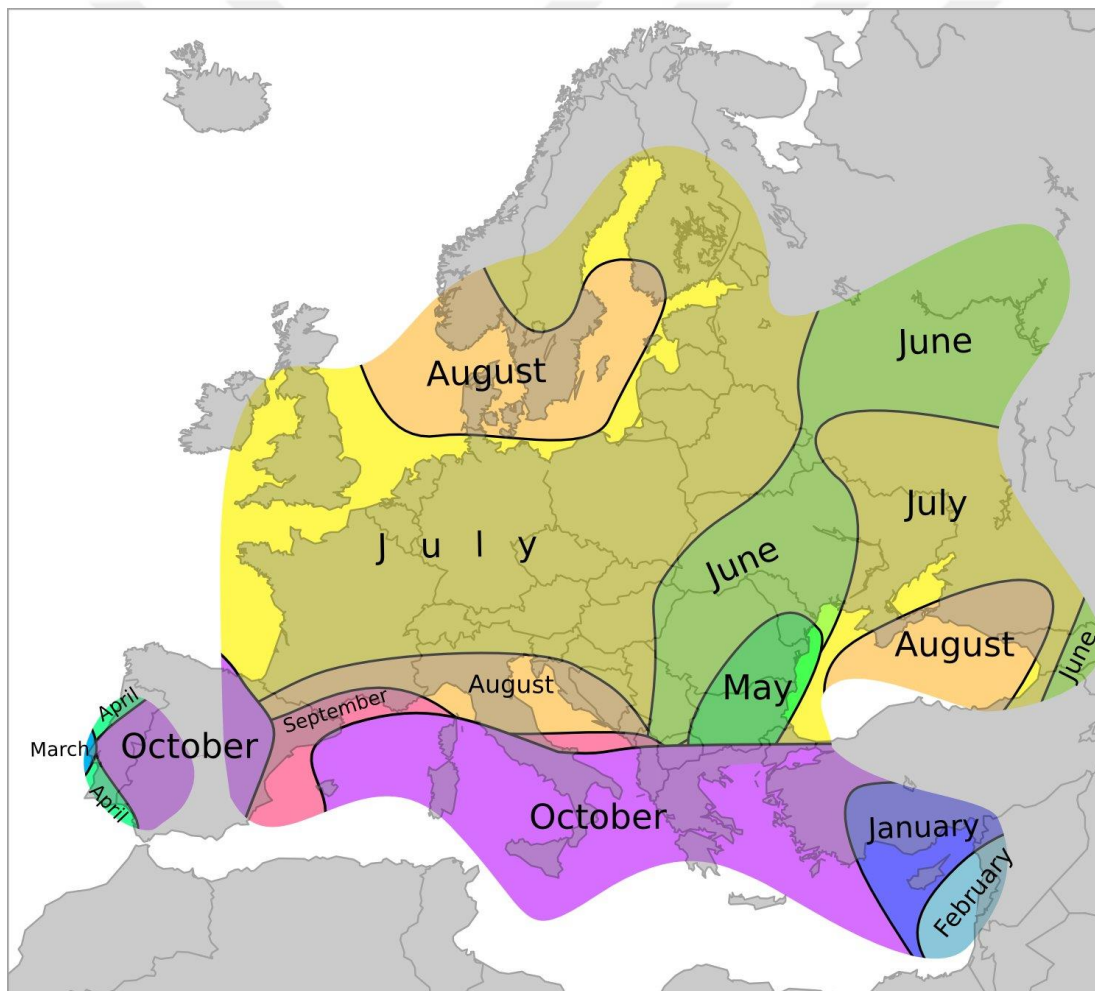


Figure 1.33 : Month of maximum number of tornado days (Groenemeijer & Kühne, 2014).

Whereas the Mid-Eastern Mediterranean Basin is an area that remained with a relatively low barometric variability due to the influence of the central European

anticyclone which is mostly under the influence of the Azores High and the extension of Siberian High. From October to March, when the trough with cold air mass behind moves through the sub-tropics (Fig. 1.33), the Mediterranean Sea has an inclination to typically create cold-core-low pressure systems (as a reactive manner from the warm SST) which carries low pressure systems from Ionian Sea to Black Sea. Five cyclogenesis areas affect the Mediterranean Basin (Fig. 1.34). They can be hazardous by contribution of ULLs which are dangled from the north by Rossby waves. The specific location for initial low development and movement is determined by synoptic dynamics. Each frontal passage triggers very different weather to develop. The severity of a system is influenced by surface pressure patterns, shortwave troughs, vortices advection, and jet stream positions. Between late October and early April, low-pressure systems and surface cold fronts influence the weather conditions in the area (Walters et al.1991).

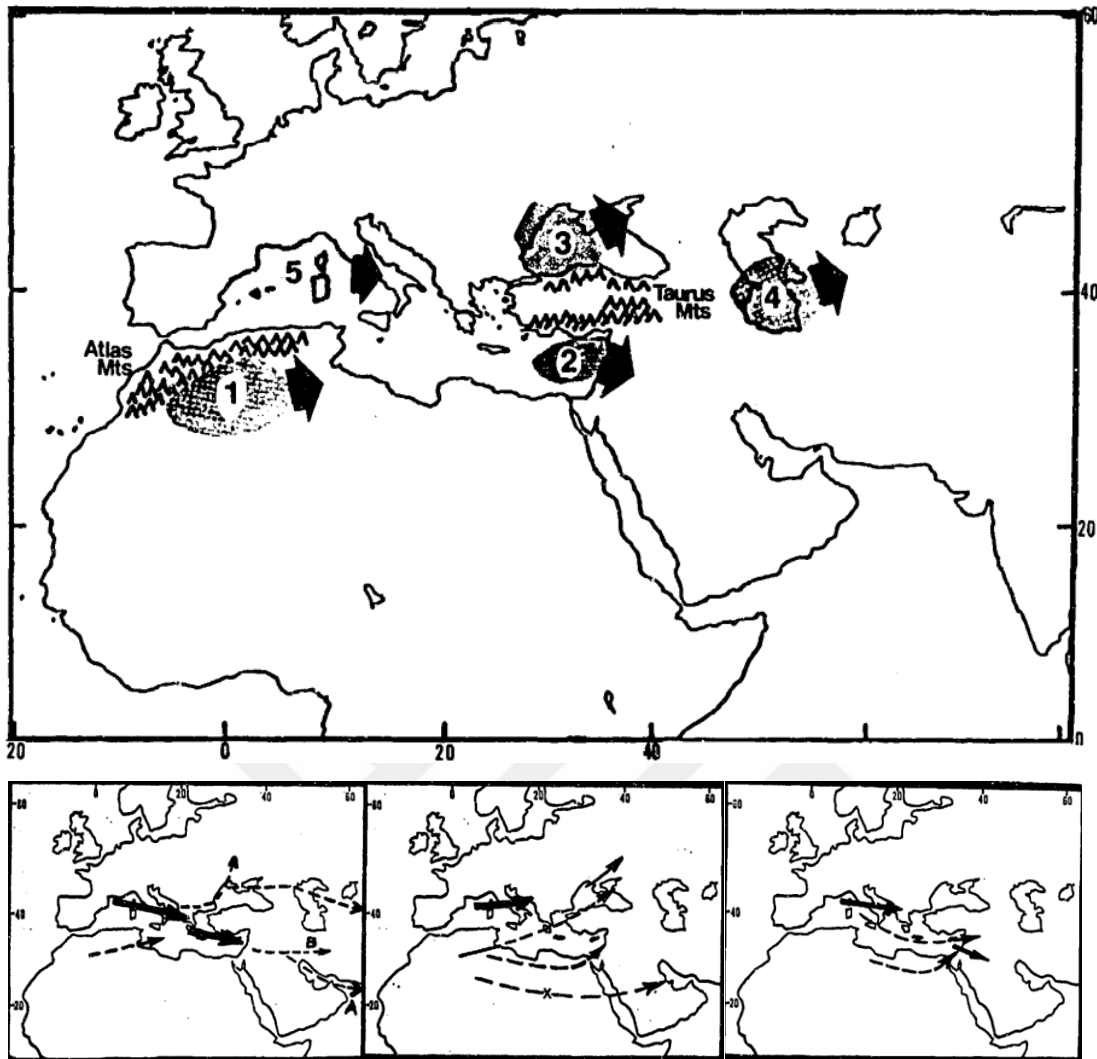


Figure 1.34 : Mid-Latitude Cyclogenesis Regions. The five primary zones of cyclogenesis are (1) the Atlas Mountains, (2) the Eastern Mediterranean, (3) the western Black Sea, (4) the southern Caspian Sea, and (5) the Western Mediterranean (Walters et al. 1991). Primary (short, solid arrow) and Secondary (dashed arrow) Mid-Latitude Storm Tracks: December, January, and February (left bottom). March, April, and May (middle bottom). November (bottom right).

The upper-level lows and troughs are responsible for 47% of tornado days and 55% of very large hail days in Türkiye; moreover, nearly a quarter of all synoptic patterns are covered by Mediterranean cyclones with both central and eastern origins, which are well-known and common wintertime events (Kahraman, 2021). For this reason, these cyclones can be different region originated and influence Eastern Mediterranean Basin from five different cyclone directions: Cyclones from Balkans (CYBAL), Cyclones from Black Sea (CYBLA), Cyclones from Center Mediterranean (CYMDC), Cyclones from Eastern Mediterranean (CYMDE), Cyclones from Africa (CYAFR) (Fig. 1.35). They are able to decrease the atmospheric pressure in the vicinity of Türkiye

afterwards. Regions of low dynamic tropopause potential temperature (high dynamic tropopause pressure) are cyclonic potential vorticity anomalies and accompanied by upper-level troughs/cyclones. With this mechanism, frontogenesis can be triggered and accompanying supercells, multi-cells, or single cell events can form through convergence zone of low-pressure system.

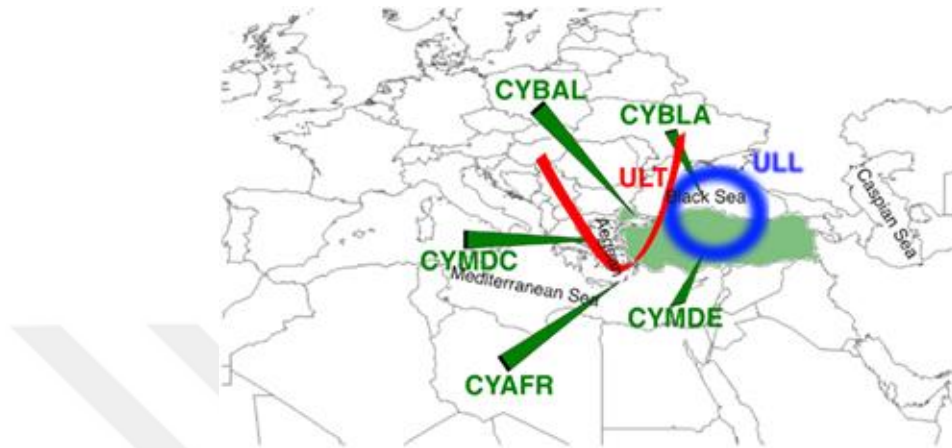


Figure 1.35 : Typical paths of cyclones and their directions over Turkiye (green arrows), and locations of upper level low (blue contour) and trough (red contour) for weather phase categories. Turkiye is shaded as light green (Kahraman, 2020).

In fact, the southern and southwestern coastline of Turkiye is likely among the most tornado-prone regions of Europe (ESWD, 2022). For instance, 443 tornado cases were reported on the lands and coastal regions of Turkiye from 2015 to 2022 (ESWD, 2022). There are tornadoes with intensities ranging from F0 to F3, with F1 being the most frequently reported or implied. Kahraman (2014) revealed that the months of May and June are the most likely for mesocyclonic tornadoes, with October and November seeing a secondary peak in Turkiye. Nonmesocyclonic tornadoes (waterspouts) are most common in the winter along the (southern) Mediterranean coast and in the fall along the (northern) Black Sea coast. Tornadoes, both mesocyclonic and nonmesocyclonic, are most likely to occur in the afternoon and early evening (Kahraman, 2014).

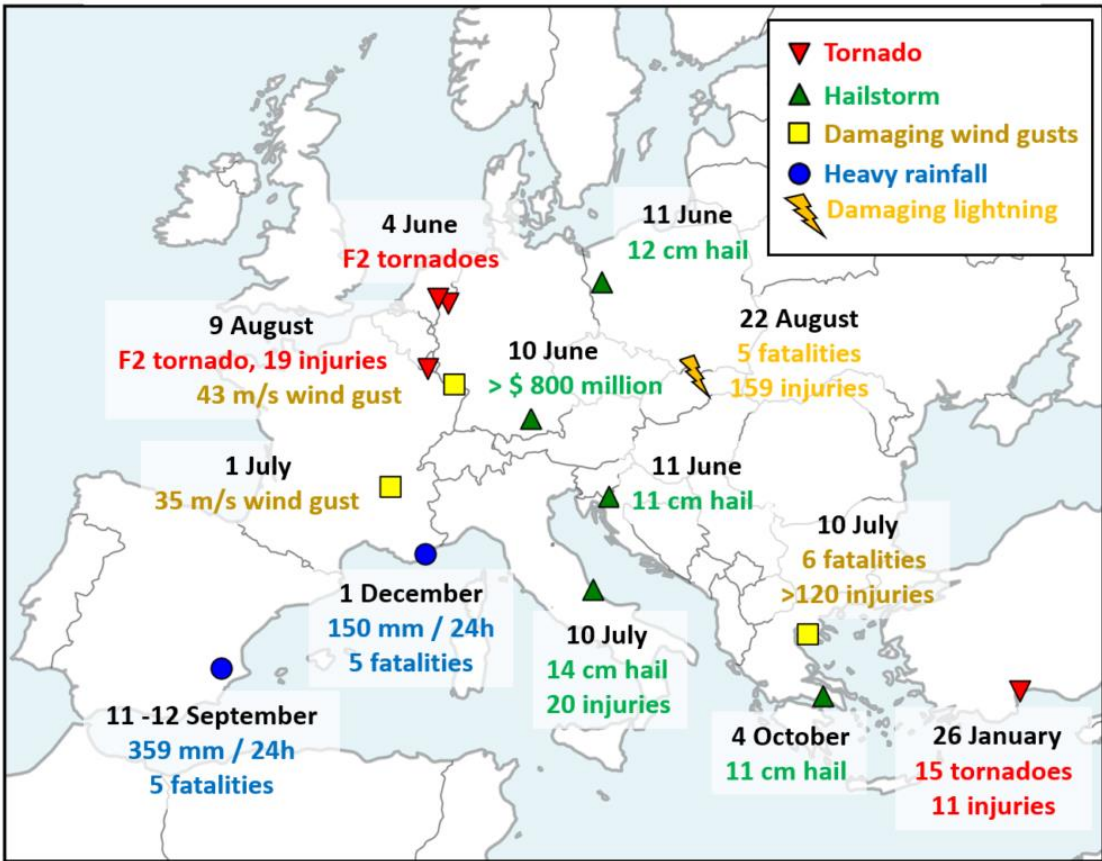


Figure 1.36 : Major convective storm events in 2019 (ESWD, 2021).

Considering such high-impact extreme weather events such as hailstorms, damaging winds, lightnings, heavy rainfall and tornadoes, 2019 was just one of those memorable years with severe convective storms and the damage they caused (Fig. 1.36). One of these severe weather conditions carried by consecutive thunderstorms and mesoscale convective systems through Eastern Mediterranean. Only in province of Antalya, Turkiye from the beginning of 2015 to the end of 2021, totally 123 tornado events (including all types) has occurred (ESSL, 2021). To illustrate, started as a waterspout and evolved to supercellular tornadic storm on 26 January 2019 in Antalya and it struck Antalya Airport, ripped the buildings and vehicles around the coastal areas of the city in Fig. 1.37.



Figure 1.37 : A tornado incident on January 26, 2019, Antalya Airport, Turkiye.

1.2.8 Current understanding of environmental conditions and dynamics of severe convective storms & tornadoes

A convective storm requires three main ingredients to form with mesocyclones; low-level moisture, instability, lifting trigger mechanism. Those are primarily necessities that could increase the probability of occurrence of the severe thunderstorm with producing tornado incident. In fact, strong vertical wind shear can be a negative factor during storm initiation (Markowski & Richardson, 2011). However, once a storm has initiated, vertical wind shear take on a different role and can increase its severity and longevity as a fourth ingredient. A low-level moisture concentration and conditional instability make an air parcel buoyant during ascent. The third component, a lifting mechanism, is necessary to ensure that the parcel ascends to the Level of Free Convection (LFC) from Lifted Condensation Level (LCL), where it first becomes positively buoyant, before it may accelerate freely upward from LFC. Because most tornadoes are related to the strength of a thunderstorm, and these sorts of storms normally gain most of their energy from solar heating and latent heat released by the condensation of water vapor, it is not surprising that most tornadoes occur in the

afternoon and evening hours, with a minimum frequency around dawn (when temperatures are lowest and radiation deficits are highest).

The dynamics of moist convection is even more complicated than the already complicated dynamics of dry convection. In mesocyclones supercell environment, the intersection area of cold air from the Rear Flank Downdraft (RFD) region and humid-warm air creates wind shear throughout the vertical layer of troposphere. Tornadoes become more likely as streamwise vorticity and storm-relative helicity near the ground increase. According to research, the relative frequency of occurrence of convective hazards such as large hail, severe wind gusts, and tornadoes increases as vertical wind shear increases. With deep moist convection tends to become increasingly organized as the vertical wind shear increases (Markowski & Richardson, 2011).

At this point, hodographs are significant for determining vertical wind shear in different layers. Long, curved hodographs in the lower troposphere represent storm relative helicity environments favorable to supercells in Fig 1.38.

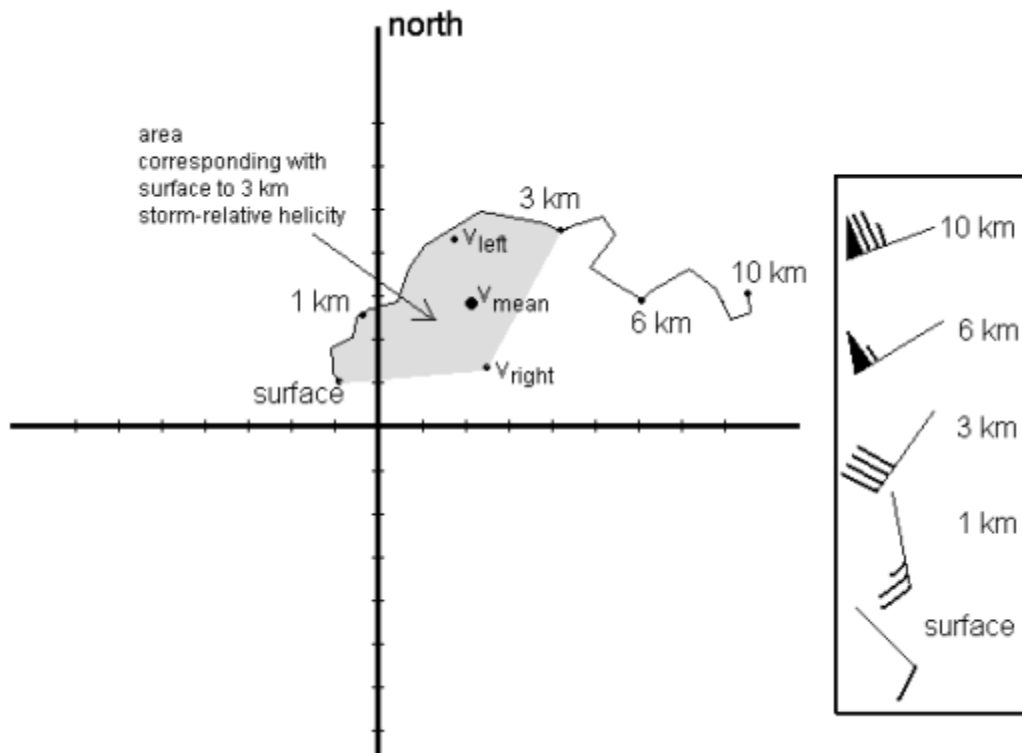


Figure 1.38 : Typical hodograph and the motion of the mean wind represents possible supercell storm, the left- and right-moving storms plotted on it as well a shaded area corresponding to 0-3 km storm-relative helicity for a right-moving storm (ESTOFEX, n.d.).

Rasmussen and Blanchard (1998) examined National Weather Service soundings from 1992 to distinguish between environments associated with supercells that produced tornadoes of F2 intensity or higher (deemed "significant" tornadoes), supercells that did not generate significant tornadoes, and non-supercell thunderstorms. In the scope of Mediterranean Basin and especially Turkiye, severe convective storm environments and tornado environments were analyzed comprehensively for the first time and whether revealed to serve the purposes of tornado forecasting (Kahraman & Markowski, 2014; Kahraman et al. 2017).

Environmental parameters, including wind shear metrics, have been used as predictors in statistical models and neural networks to provide probabilistic forecasts of convective hazards in recent and ongoing research. For tornadoes, numerous composite parameters that incorporate measures of vertical wind shear have been developed.

One of the composite indices is the Energy–Helicity Index (EHI), which combines Convective Available Potential Energy (CAPE) and Storm-Relative Helicity (SRH) (Hart and Korotky 1991; Davies-Jones 1993). It is formulated as in the following:

$$EHI = \frac{CAPE \times SRH}{160,000} \quad (1.5)$$

Another composite index for supercell forecasting is the Supercell Composite Parameter (SCP) is designed by adding Bulk Wind Shear (BWD) to identify environments favorable for the development of supercells, and is calculated using the formula developed in the following (Thompson, 2004):

$$SCP = \frac{MUCAPE}{1000 \text{ J kg}^{-1}} \times \frac{SRH_{03}}{50 \text{ m}^2 \text{ s}^{-2}} \times \frac{BWD_{06}}{20 \text{ m s}^{-1}} \quad (1.6)$$

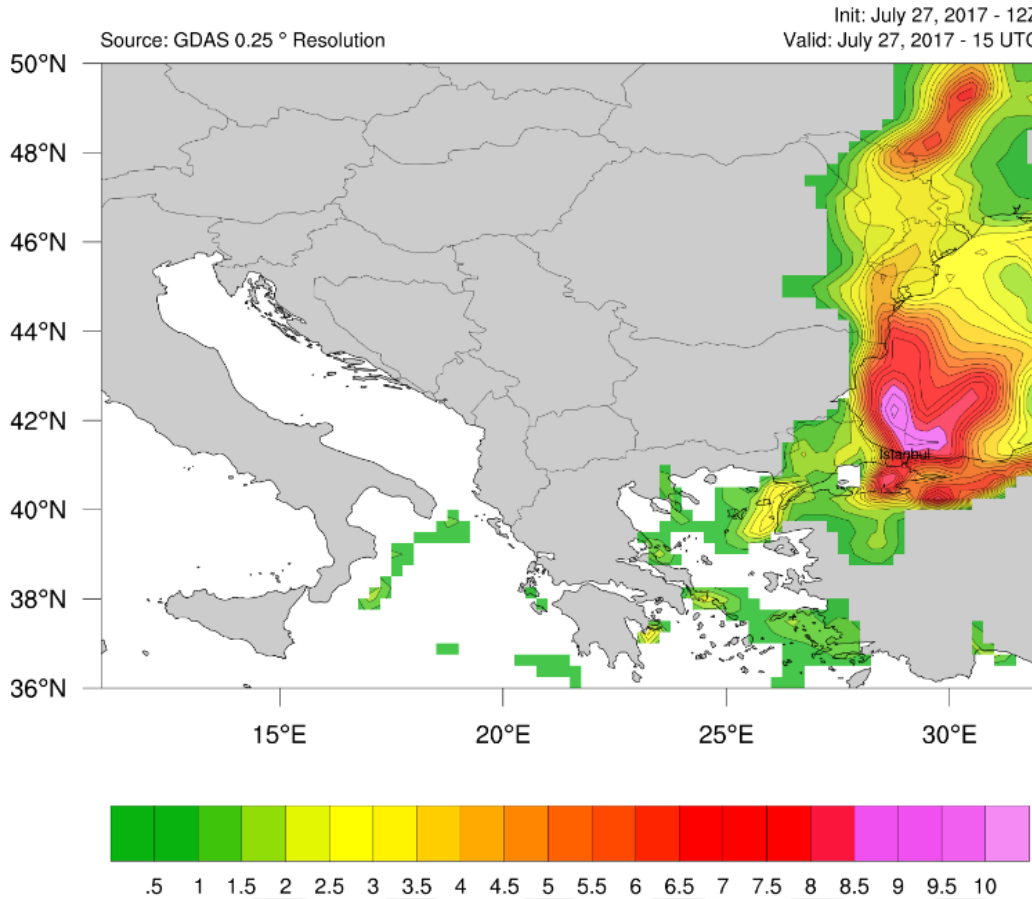


Figure 1.39 : A supercell forecast based on Supercell Composite Parameter (SCP) valid for July 27, 2017, 15 UTC.

The Significant Tornado Parameter (STP) is an index established to identify significant tornadic storm environments (Thompson et al. 2004). It combines SBCAPE and deep-layer shear (ingredients for supercells), in addition to SRH01 and LCL (ingredients for tornadoes) in the following manner (Eq. 1.7):

$$STP = \frac{SBCAPE}{1500 \text{ J kg}^{-1}} \times \frac{2000 - SBLCL}{1000 \text{ m}} \times \frac{SRH_{01}}{150 \text{ m}^2 \text{ s}^{-2}} \times \frac{BWD_{06}}{20 \text{ m s}^{-1}} \quad (1.7)$$

A remarkable number of tornadoes in Turkiye were notified as a waterspout and most of these waterspouts especially in the vicinity of coastal areas appear as non-mesocyclonic (Kahraman & Markowski, 2014). In terms of CAPE, the environments of severe convective storms in Turkiye are typically 500 Jkg^{-1} larger and roughly 500-1000 Jkg^{-1} smaller than US in comparison to the rest of Europe and US, respectively (Kahraman et al. 2017). The LCL for severe storm environments in Turkiye is equivalent to the LCL recorded for environments in Europe, and LCLs in both regions are lower than those for severe storm environments in the United States (Kahraman et

al. 2017). Compared to other types of extreme weather, non-mesocyclonic tornadoes have a lower CAPE. Supercell surroundings in Turkiye demonstrate weaker deep-layer vertical wind shear than supercell environments in US, while tornadic supercell surroundings in Turkiye indicate significantly $\sim 2\text{--}4\text{ ms}^{-1}$ weaker low-level shear than supercell environments in US and Europe (Kahraman et al. 2017).

The highest SCP values in Turkiye lead to very large hail and supercell environments, followed by mesocyclonic tornado and F2+ tornado environments (Kahraman et al. 2017) (Fig. 1.40). Even though, STP exceeding value of 1 is commonly considered to be supportive of significant tornadoes in the United States, rarely exceeds value of 1 in Turkiye due to climatologically modest 0-1-km SRH and SBCAPE in comparison to the US (Kahraman et al. 2017).

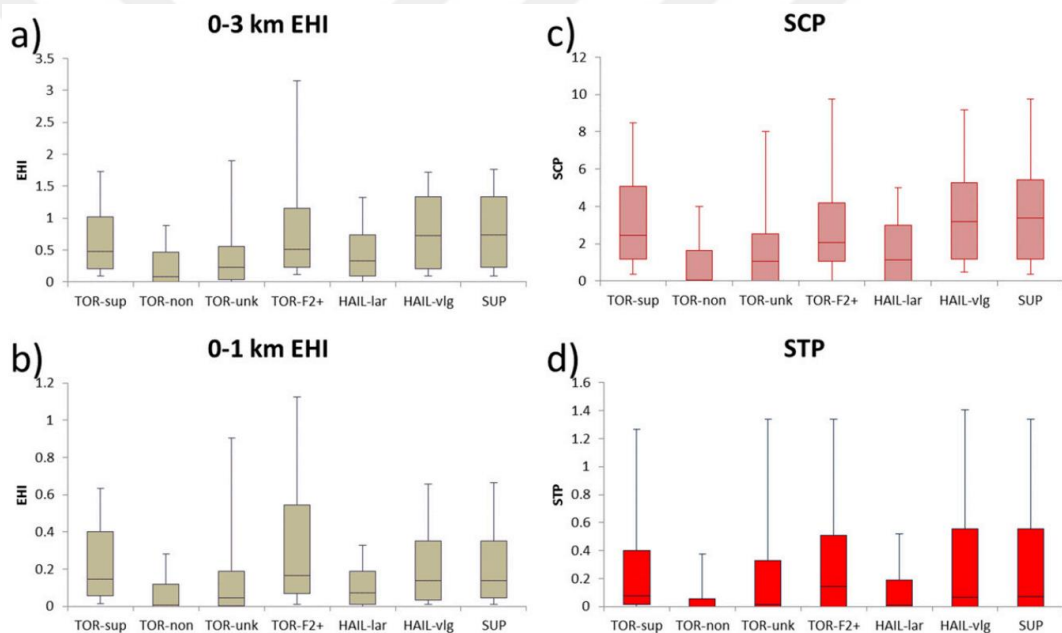


Figure 1.40 : Composite parameter thresholds for hail and tornado events in Turkiye: (a) EHI for the 0–3-km layer, (b) EHI for the 0–1-km layer, (c) SCP, and (d) STP (Kahraman et al. 2017).

This means that composite thermodynamic or kinematic parameters such as STP and SCP may not constantly identify the dynamics of storms Eastern Mediterranean as they have CAPE, SRH, BWD, LCL ingredients in their formulas. For this reason, commonly used thresholds in US for such composite parameters would have to be modified for use in Turkiye; however, the necessity of detailed numerical modeling for specific days are inevitable. It should be concerned that to discriminate a misleading CAPE value that may occur with the effect of the warm water of the

Mediterranean and to obtain specific days which are sufficient to occurrence and development of tornadic storms.

1.2.9 SCSs, tornadoes, and their associations with climate change

In the scope of frequencies of SCSs and tornadoes, associations with various climate and environmental trends exist. For example, an increase in the sea surface temperature of a source region (e.g. Gulf of Mexico) increases atmospheric moisture content. Enlarged moisture can fuel an increase in severe weather and tornado activity, particularly in the cool season. Besides, several evidence does suggest that the Southern Oscillation is weakly correlated with changes in a tornado incident, which vary by season and region, as well as whether the ENSO phase is that of El Niño or La Niña. Cook and Schaefer (2008) has found that fewer tornadoes and hailstorms occur in winter and spring in the U.S. central and southern plains during El Niño, and more occur during La Niña, than in years when temperatures in the Pacific are relatively stable. Ocean conditions could be used to forecast extreme spring storm events for United States several months in advance. Climatic shifts may affect tornadoes via teleconnections in shifting the jet stream and the larger weather patterns. Due to considerably moving of jet-streaks to Northern latitudes for a few kilometers each year, SCS formation zones are moving further to relatively north as well.

According the report of IPCC AR6 (2021), atmospheric temperature gradient in extratropical regions has sort of influences on jet streaks and upper-level winds. They interact also with stratospheric level zonal winds (10 hPa - 60 N/S). Most of the scientists agree that if the temperatures in polar regions are still continuing to rise more than lower latitudes in the near future, the temperature difference between polar regions and middle latitudes is decreasing (see Fig. 1.41) and the temperature gradient force will be weakening. Hence, this process will be triggering Arctic Amplification (AA).

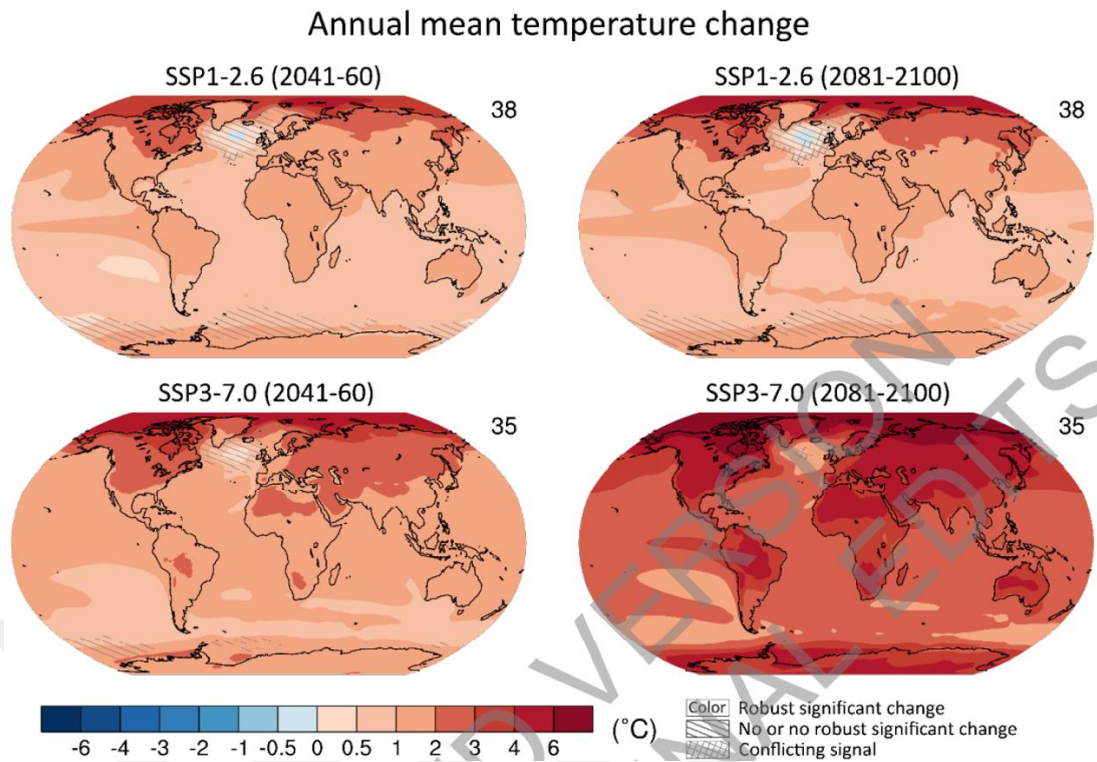


Figure 1.41 : Mid and long-term change of annual mean surface temperature according to different SSP scenarios (IPCC, 2021).

Therefore, zonal winds at stratospheric level can become more meridional and cold air masses in the troposphere can move through the lower latitudes, easily. The intersection areas of cold and warm air masses are being expected to placing a little bit norther with the movement of jet streaks because the amount of cold air is getting smaller and the boundary between polar and tropical air masses tend to relocate at higher latitudes.

The climate-tornado link is confounded by the forces affecting larger patterns and by the local, nuanced nature of tornadoes. Although it is reasonable to suspect that global warming may affect trends in tornado activity, there is no valid consensus for increasing activity of tornado occurrence around the world. As the regions in Europe, especially the Mediterranean Basin, are considered, it can be expected that an area will show a different trend of increase or decrease depending on the type and characteristics of the SCSs compared to another region (Fig. 1.42).

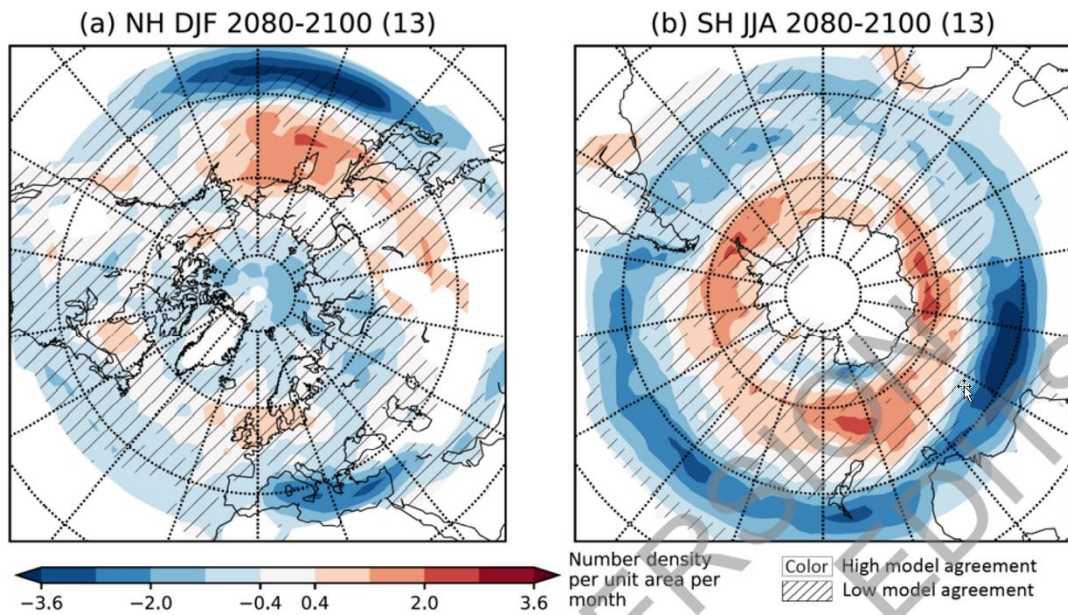


Figure 1.42 : Changes in extratropical storm track density in Northern Hemisphere (left) and Southern Hemisphere (right) (IPCC, 2021).

It is on the whole estimated that while the warming of SSTs provides additional water vapor for the atmosphere and triggers convection processes, wind shear values will be weakening stems from the absence of sweeping mechanism of jet winds in the mid-latitudes. To illustrate, the number of days with daylight conditions conducive for strong convective storms would typically rise over the Mediterranean Sea and slightly decline across Western Europe in the late 21st century (Kahraman et al. 2020).

As a result, from sub-tropical latitudes to extratropical latitudes, convective storms while it is expected to show a decreasing tendency in terms of kinematic support, it may tend to increase in terms of triggering thermodynamic conditions. The frequency of severe convective storms is revealed to be increasing most rapidly in coastal regions along the Mediterranean Sea (Kahraman et al. 2020). Therefore, slow-moving but heavy rainfall storms can be expected to increase in some parts of countries at these latitudes.

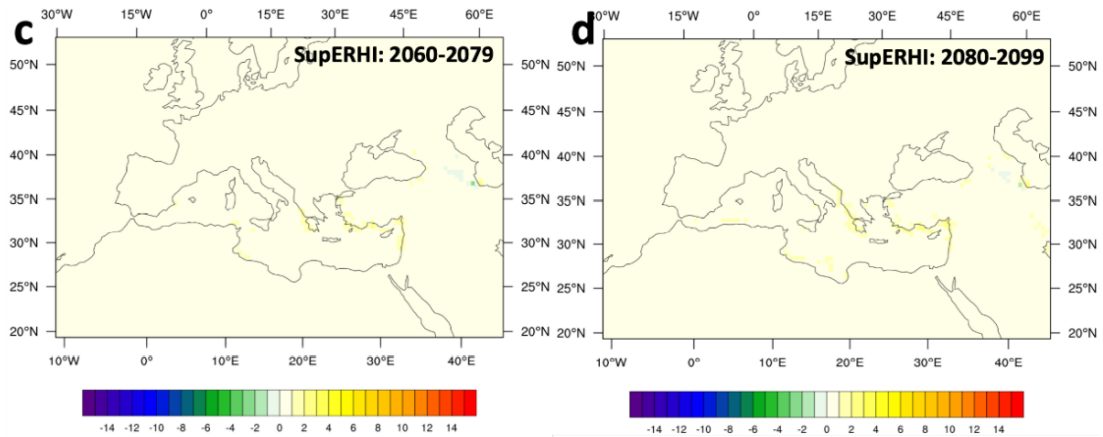


Figure 1.43 : (c) changes in average number of days with SuperERHI for 2060– 2079, (d) changes in average number of days with SuperERHI for 2080. SuperERHI indicates Supercell environment with convective rain and high instability (Kahraman et al. 2020).

1.3 Hypothesis & Necessity of EMEDO Index

There are plenty of oscillation indices which are produced and operated with the intention of examining standardized atmospheric pressure fluctuations. Despite of being inspired by the other oscillation indices in the Mediterranean Basin such as Mediterranean Oscillation (MOi) and the Western Mediterranean Oscillation (WeMOi), etc., also purpose-built index in the study EMEDOi focuses on the early prediction of tornadic storms in Turkiye and it contains more vertical thickness information through the tropospheric layer. These weather events mentioned above, should be taken into consideration several days in advance to assist nowcasting approaches. This is because, one of the current global climate crisis and adaptation processes is to use warning systems to minimize the impacts of severe weather events. As the early warning systems and alerts should undertake the reducing impacts of severe weather events, the EMEDOi could take a decisive representation in operational meteorology as an indicator of tornado weather. Reliable weather data information combined by conventional weather data and numerical modeling play a crucial role for predicting these sorts of meteorological disasters.

The fact that high SST anomalies increase the number of tornadoes and waterspouts in non-mesocyclonic structures indicates that formulas, such as STP and SCP, cannot perpetually be pioneer guides in the Eastern Mediterranean. Understanding and progressing mesoscale model studies becomes important at this point in order to predict tornado formation and dynamical concepts. Due to this reason, high-resolution

modeling is a must a few days in advance for mesocyclonic supercell thunderstorms capable of producing F2+ tornadoes. Secondary circulation and front inclination are present in these storms, and the advection in the cold front transition should be thoroughly examined. In this way, it is possible to predict the convective trigger mechanisms and weather phases and ultimately have a forecasting approach for them. Furthermore, vertical layers must be resolved and elaborately modeled in order to obtain thunderstorm characteristics such as storm motion speed and direction, critical angle, convection energy, and relative winds. These opportunities contribute to geospatial point-based tornado forecasts however operating the model of high-resolution numerical weather prediction incurs huge computational costs which are very huge amount for the institutes and national weather services.

Consequently, there is a need to examine severe weather events in the Eastern Mediterranean region, including Turkiye, and to reveal the clues that the events will take place a few days in advance. At this point, there is a necessity for a new composite parameter showing that the atmospheric conditions expected to influence the region will trigger the formation of SCSs. The main intention is not to replace these modeling approaches, or composite indexes, but to warn operationally to draw attention to the Eastern Mediterranean and Turkiye in particular a few days in advance.

Two main hypotheses were determined according to the synoptic characteristics of Turkiye, one of the countries affected by the EMEDO_i, which was formed from the points included in the analysis, and in which locations it influenced tornado events. The results of the analyzes made within the scope of the study and the accuracy of the hypotheses explained below are tested.

Firstly, EMEDO_i investigates the induction mechanism of environmental conditions of convective and frontal storm types in favor of tornadoes. Thus, this index reveals the signatures of imminent atmospheric conditions.

In the scope of the early warning events in terms of presence of low-level pressure systems and extreme weather events, it guides to run the limited area numerical weather prediction models for Turkiye by determining optimum initial model run time in advance.

2. MATERIAL AND METHODOLOGY

2.1 Study Area

In this study, Eastern Mediterranean Basin is the region that covers the main domain of investigation in the area where the new index is located. Study area has been chosen to let developing of ULL area. Since the frontal movement is a crucial event for the occurrence of mesocyclonic events and synoptic events, the points in the domain have been chosen considering different regions, respectively. The main domain is limited between 25° - 50°N latitudes and 0° - 50°E longitudes. The analysis focuses on the Mediterranean Basin (particularly the eastern part) as a limited area model domain, and it contains five different selected grid cell points (Fig 2.1, Table 2.1).

Table 2.1 : Geospatial Points (Locations).

| Geospatial Point (Defined Location) | City, Country | Latitude, Longitude - (DD) |
|--------------------------------------------|----------------------|-----------------------------------|
| P0 | Ashdod, Israel | 31.81 N, 34.65 E |
| P1 | Lecce, Italy | 40.35 N, 18.18 E |
| P3 | Durres, Albania | 41.31 N, 19.46 E |
| P4 | Ioannina, Greece | 39.67 N, 20.86 E |
| C | Vlore, Albania | 40.46 N, 19.48 E |



Figure 2.1 : Representation of oscillation points in analysis domain over Eastern Mediterranean Basin (Inclined Satellite Projection).

2.2 Data

The GDAS re-analysis dataset by the GFS model of the National Center for Environmental Prediction (NCEP) has been used (Table 2.2). In addition to that, data are utilized as initial conditions and to establish pre-analysis of tornadic storm events and until several hours later. It has 6-hour temporal resolution and 0.25° spatial resolution and it covers 20301 total grids as 201 grid points west to east and 101 grid points south to north with 27 km (0.25°) spatial resolution. For the map visualizations and diagrams, a few of smoothing processes were applied. These data consist of geopotential (m^2s^{-2}) for specific limited area model domain.

Table 2.2 : Description of model configuration and utilized data

| Model | Global Data Assimilation System (GFS-NCEP-NOAA) |
|-----------------------------|-------------------------------------------------|
| Central point of domain | 37.50°N, 25°E |
| Spatial Resolution | 27 km (interpolated to 13.5 km) |
| Vertical level | 23+ (4 levels are used) |
| Temporal resolution | 6h (interpolated to 3h) |
| Temporal extent | 01.01.2017 00:00 UTC to 31.12.2022 23:00 |
| Initial/boundary conditions | Arranged by GFS-NCEP-NOAA |

In addition, 14 tornado events (Table 2.3) and 1 hail event (Appendix B.1) are selected to investigate EMEDO index while 5 events as a test cluster were added to ensure that the index was stable (Table 2.4).

Table 2.3 : Selected tornado/waterspout events for training in Turkiye and their features (ESWD, 2021).

| Date | Time (UTC) | Latitude/Longitude | Intensity | Path Length (km) | Path Width (m) | Funnel Cloud | Area | Province |
|------------|------------|--------------------|-----------|------------------|----------------|--------------|-----------|----------|
| 17.01.2016 | 16:00 | 36.26 N, 29.99 E | F1 | 7 | 270 | yes | landwater | Antalya |
| 05.02.2016 | 13:30 | 36.91 N, 30.57 E | F1 | ? | ? | ? | land | Antalya |
| 03.03.2016 | 15:00 | 36.80 N, 31.49 E | F1 | ? | ? | yes | land | Antalya |
| 13.11.2017 | 18:30 | 36.34 N, 30.19 E | F3 | 8.1 | 300 | yes | land | Antalya |
| 21.11.2018 | 10:05 | 36.82 N, 28.31 E | F1 | ? | ? | yes | waterland | Mugla |
| 24.01.2019 | 10:30 | 36.36 N, 30.28 E | F2T4 | 9 | 400 | yes | landwater | Antalya |
| 26.01.2019 | 07:58 | 36.89 N, 30.80 E | F2T4 | 11.2 | 360 | yes | waterland | Antalya |
| 06.01.2020 | 17:10 | 36.59 N, 31.88 E | F1 | ? | ? | ? | land | Antalya |
| 08.10.2020 | 10:20 | 40.98 N, 27.98 E | F0 | ? | ? | ? | water | Tekirdag |
| 27.01.2021 | 05:30 | 36.75 N, 28.99 E | F1 | ? | ? | ? | land | Mugla |
| 11.02.2021 | 18:10 | 38.26 N, 26.38 E | F2 | 3.3 | 100 | ? | waterland | Izmir |
| 12.10.2021 | 11:45 | 37.40 N, 27.65 E | F1 | ? | ? | ? | land | Mugla |
| 07.12.2021 | 07:33 | 38.24 N, 26.31 E | F1 | 3 | 110 | ? | landwater | Izmir |
| 19.12.2021 | 11:12 | 36.62 N, 31.77 E | F1 | ? | ? | ? | waterland | Antalya |

Table 2.4 : Selected tornado/waterspout events for stability test in Turkiye and their features (ESWD, 2021).

| Date | Time (UTC) | Latitude/Longitude | Intensity | Path Length (km) | Path Width (m) | Funnel Cloud | Area | Province |
|------------|------------|--------------------|-----------|------------------|----------------|--------------|-----------|----------|
| 09-01-2022 | 18:20 | 36.30 N, 30.33 E | F0 | ? | ? | ? | waterland | Antalya |
| 02-03-2022 | 17:35 | 36.96 N, 31.05 E | F1 | 5 | 220 | ? | land | Antalya |
| 19-04-2022 | 06:30 | 36.84 N, 31.18 E | ? | ? | ? | ? | waterland | Antalya |
| 15-10-2022 | 06:00 | 36.70 N, 31.51 E | ? | ? | ? | ? | water | Antalya |
| 07-11-2022 | 09:00 | 36.57 N, 31.87 E | ? | ? | ? | ? | water | Antalya |

2.3 Methods

2.3.1 Description of EMEDO index (EMEDO_i)

The EMEDO_i is a barometric pattern index measuring over the Eastern Basin of the Mediterranean of fluctuations in the difference of atmospheric pressure at upper level between the Israel and the triangle area in the vicinity of Greece/Albania (Fig 2.2).

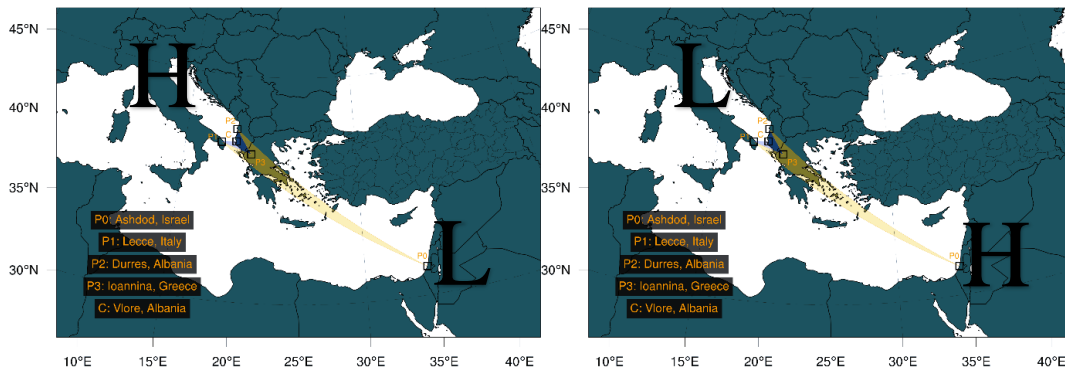


Figure 2.2 : Representation of oscillation points in analysis domain (Lambert Projection) and pressure placements indicates positive EMEDO index (left) and negative EMEDO index (right).

According to hydrostatic equilibrium equation, geopotential unit is in [m²/s²] as in the following equation (2.1):

$$\Phi(z) = \int_0^z g \partial z \quad (2.1)$$

The geopotential unit was divided by the gravitational acceleration at the surface of Earth (g_0) due to the application of hydrostatic equilibrium in the atmosphere, to convert the data set into a geopotential height as in the following equation (2.2).

$$Z = \frac{\Phi(z)}{g_0} \quad (2.2)$$

EMEDO_i values were divided into two phases as EMEDO_i (-) and EMEDO_i (+), thus the effect of either phase on the climatic parameters, as mentioned below, were detected and compared. The EMEDO_i was expressed by (2.3) which are consists of two different parts in (2.4) and (2.5):

$$\text{EMEDO}_i = \text{ThkCoef} \times \text{ULpattern} \quad (2.3)$$

$$\text{ThkCoef} = \mp \frac{(Z500 - Z1000)_i - (Z500 - Z1000)_{P0} - cf}{15} \quad (2.4)$$

$$\text{ULpattern} = \frac{|(Z500)_i - (Z500)_{P0}|}{20} \times \frac{|(Z300)_i - (Z300)_{P0}|}{20} \quad (2.5)$$

for $i = P1, P2, P3$ from Table 1 and correction factor (cf) = 10.17.

The coefficient part of the formula, “ThkCoef”, indicates fluctuations in the geopotential height thickness between 1000 hPa - 500 hPa isobaric levels. It should also be considered that the coefficient part determines whether or not the EMEDO_i has positive or negative sign. The main part of the formula, which is called the “UL pattern”, demonstrates the upper-level synoptic pattern surrounding air around 500 hPa and 300 hPa.

EMEDO_i poles do not have any cyclonic or anticyclonic pressure centers such as Icelandic Low or Azores High. Typically, as a tributary of Rossby waves and subtropical/tropical air pressure sequences, other dominant pressure systems have an impact on these regions. Due to global warming stems from surplus of energy budget of the Earth, it should be considered that extending high pressure areas at around 30 N/S latitudes due to radiative energy surplus. Take into consider these conditions, P0 pole has mostly greater thickness difference than the triangle area which is located in

the norther during the seasons. Thus, it leads constant thickness difference between two poles of EMEDO_i. In order to prevent inconvenient analysis, correction coefficient is produced for H500-H1000 geopotential height on annual data of 1991-2020 period climatologically. This adjustment value indicates the mean difference of last 30 years between index poles. It helps to compensate this deviation between two different poles of EMEDO_i.

2.3.1.1 Variations of EMEDO_i

There are seven (three main, one control, one maximum, one ensemble mean, and one operational) variants of EMEDO_i. The necessity for EMEDO-Control (EMEDO-Ctrl) is related to point 3 and investigates the existence of a trough over Greece and aids in understanding the structure of the trough over Greece, including whether or not it has cut-off or moving extension of Rossby waves. In this way, EMEDO-Oper is derived from the coefficient of computation of the main fluctuations (EMEDO1, EMEDO2, EMEDO3, EMEDO-Ctrl). In addition to these, EMEDO-Max corresponds to at least one point where the values are at an extreme level. Besides, EMEDO-Ens represents the total strength of the fluctuations. When cut-off low pressure system dragged from southwest to northeast direction, one of the points in the triangle allows to detect the transition of low-pressure system.

$$\text{EMEDO}_i = \text{ThkCoef}_i \times \text{ULpattern}_i \quad (2.6)$$

$$\text{EMEDO}_{ctrl} = \text{ThkCoef}_c \times \text{ULPattern}_c \quad (2.7)$$

$$\text{EMEDO}_{oper} = \text{ThkCoef}_c \times \text{ULPattern}_{mean} \quad (2.8)$$

$$\text{EMEDO}_{ens} = \text{ThkCoef}_{mean} \times \text{ULPattern}_{mean} \quad (2.9)$$

$$\text{EMEDO}_{max} = \text{ThkCoef}_{max} \times \text{ULPattern}_{max} \quad (2.10)$$

for $i = P1, P2, P3$ and $c = C$ from Table 1.

2.3.1.2 Positive phase

The EMEDO is in a positive phase when both the middle of the Mediterranean Sea (Adriatic Sea, Ionian Sea) and southern Europe have stronger air pressure than average. The vicinity of Israel (the Harbor of Ashdod) is typically influenced by humid

(drier within time) and cold air masses or cyclones (a low-pressure system at MSL and higher geopotential heights in the upper troposphere) that are typically dominant and mostly stem from a tributary of the Indian monsoon. In the positive phase of EMEDO_i, this geopotential thickness decreases because of an ULL's movement toward lower latitudes. Azores high-pressure system loses its typical position (occasionally with the effect of Iberian Thermal Low), and afterwards it horizontally extends and entwines diagonally to the northeast. This high pressure is stagnant around middle Mediterranean Basin and substitutes Mid-Europe passing through. In this way, the EMEDO_i becomes strong in the positive phase. During positive EMEDO phases, the increased difference in pressure between the two regions results in an enhanced ridge in southern Europe and an extremely eastward shift of the storm track. Consequently, southern Europe experiences decreased storminess and precipitation and warmer-than-average temperatures that are associated with the air masses that arrive from higher latitudes. In western Turkiye, the positive phase of the EMEDO generally brings stagnant higher air pressure; a condition associated with fewer cold-air outbreaks in the following days and decreased storminess. At the same time, the Middle East and Caspian Sea experience lower-than-average temperatures, increased storminess, and above-average precipitation. Hence, ULL brings wet weather across the Middle East. Besides, the ULL movement through the Mediterranean Sea should be considered due to the moving of Rossby waves to the east as a requirement of middle latitudes in the Northern Hemisphere. As a result, the positive phase of EMEDO_i is mostly observed as a regular movement pattern of pressure sequence after the negative phase.

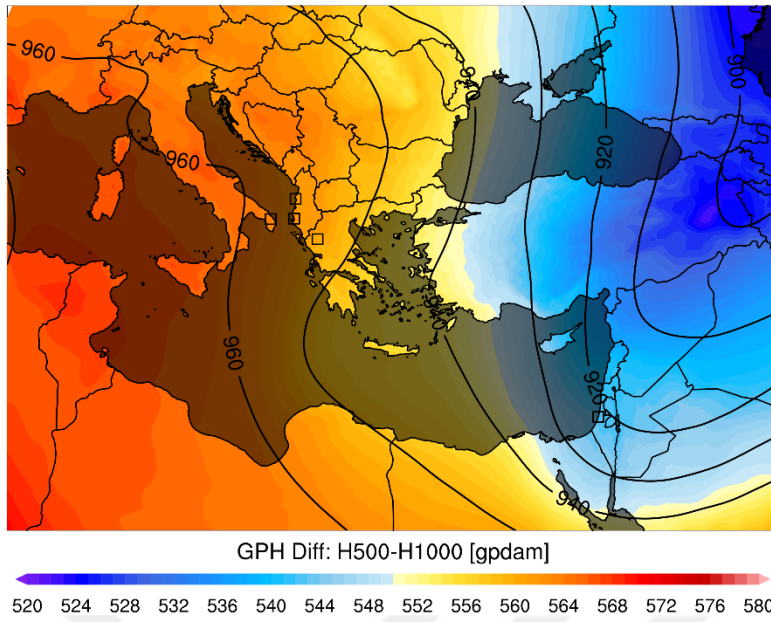


Figure 2.3 : Geopotential height [gpdam] at 300 hPa (isohypses) and geopotential height [gpdam] difference between 500hPa and 1000hPa (shaded color contours) - 27.01.2016 – 12 UTC.

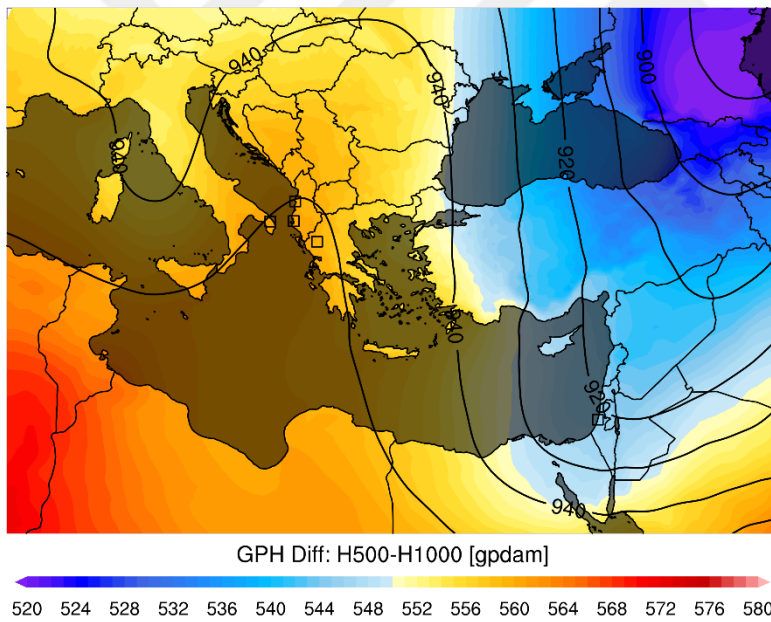


Figure 2.4 : Geopotential height [gpdam] at 300 hPa (isohypses) and geopotential height [gpdam] difference between 500hPa and 1000hPa (shaded color contours) - 16.02.2017 – 18 UTC.

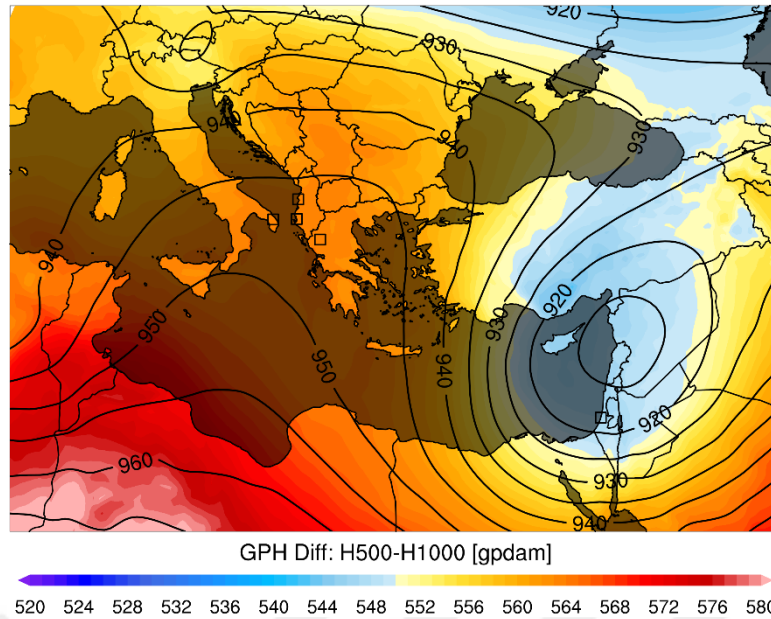


Figure 2.5 : Geopotential height [gpdam] at 300 hPa (isohypses) and geopotential height [gpdam] difference between 500hPa and 1000hPa (shaded color contours) - 21.03.2020 – 00 UTC.

2.3.1.3 Negative phase

The EMEDO's negative phase is characterized by lower-than-average air pressure with baroclinic conditions over the mid-southern Mediterranean Basin. The jet stream is directed from southwest to northeast under these conditions with the contribution of upper level trough. When Azores High vertically covers Western Europe, the triangle area on Greece often encounters with intense ULL from Siberian Region, Middle-Eastern Europe or Balkans during winter time of Northern Hemisphere. These troughs have capability of bringing snowstorms to Eastern Mediterranean such as Greece and Turkiye, rarely to Egypt and Libya in the following days. Broad cold spells and shower rains coming down into Aegean Sea occasionally be divided into cut-off low system or triggered by Omega Block. Thunderstorms, mesoscale convective systems, and cold-fronts (rarely blizzards during winter season) can be produced and shifted southerly of their usual paths. Thus, the sub-tropical part of Eastern Mediterranean Sea, southeastern Europe countries such as Balkans (Greece, Bulgaria, etc.), Ukraine, Turkiye, Cyprus, a generally see greater cold air outbreaks than usual after southerly winds. Conversely, in western Mediterranean and Middle East, dominated by higher air pressure in the negative phase EMEDO, a condition associated with stronger heat waves and decreased storminess. In other words, a negative EMEDO phase is associated to northern based airflows which have travelled and get humidity over the

Mediterranean Sea; these are therefore laden with moisture when they reach the Crete and Rhodes Islands of Greek Islands, western side of the Turkiye, leading to increased (sometimes torrential) frontal precipitation in this area. Tornadoes are more frequent across Eastern Mediterranean and along with coasts of Greece and western parts of Turkiye. These events are typically caused by either supercell frontal structures on the MCS line or sea-induced instabilities which is necessary for waterspouts.

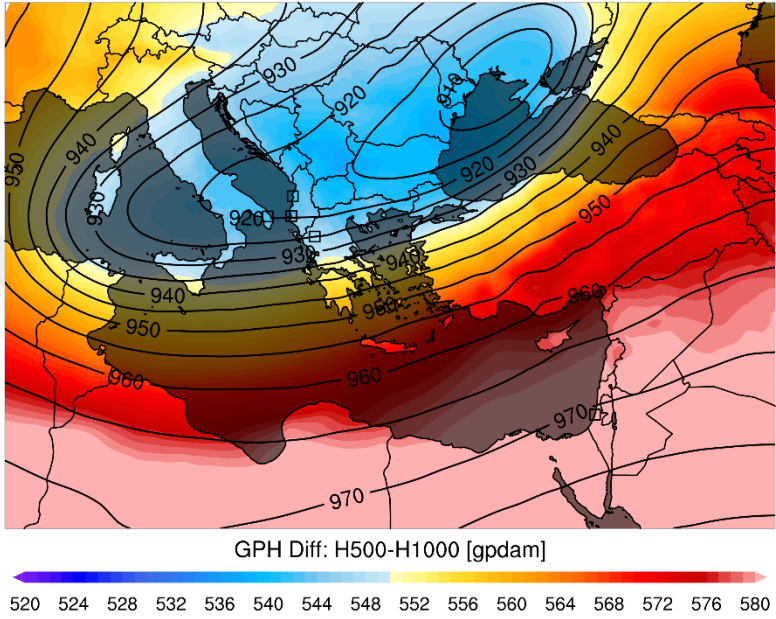


Figure 2.6 : Geopotential height [gpdam] at 300 hPa (isohypses) and geopotential height [gpdam] difference between 500hPa and 1000hPa (shaded color contours) - 21.04.2017 – 12.00 UTC.

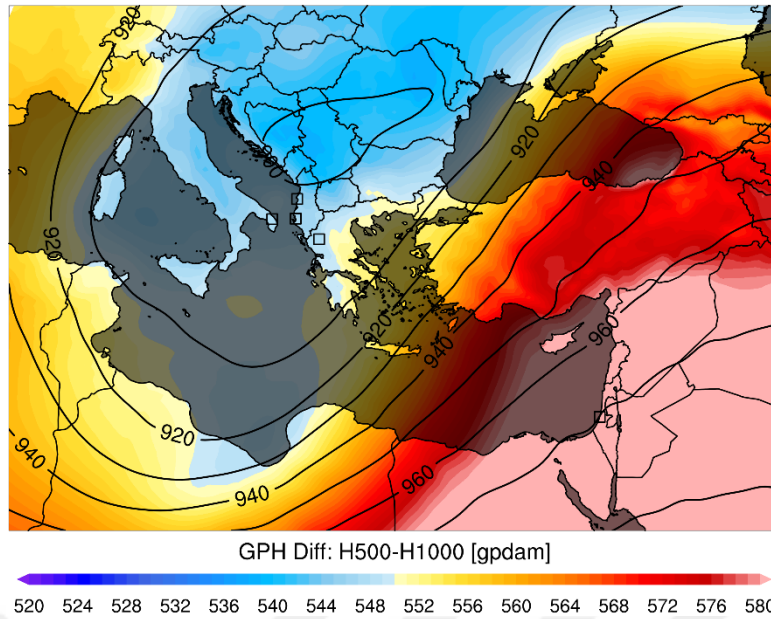


Figure 2.7 : Geopotential height [gpdam] at 300 hPa (isohypses) and geopotential height [gpdam] difference between 500hPa and 1000hPa (shaded color contours) - 23.03.2018 – 18 UTC.

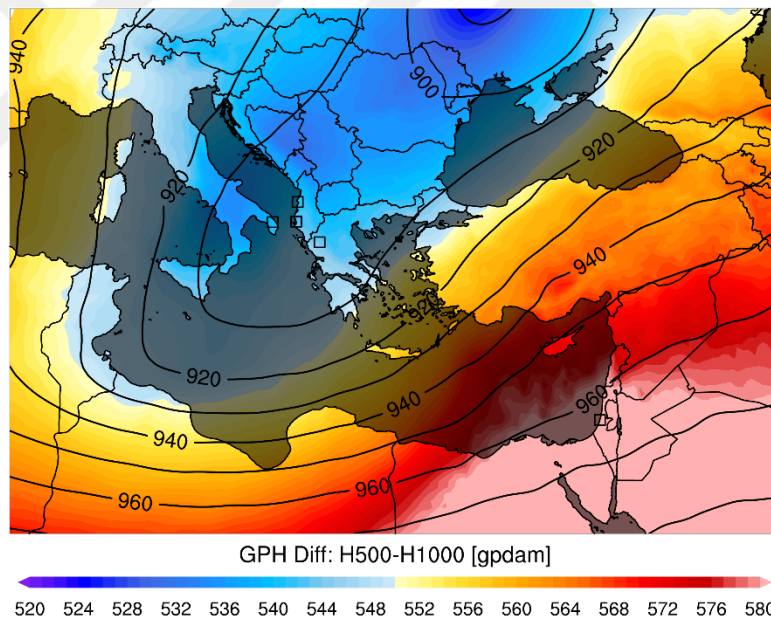


Figure 2.8 : Geopotential height [gpdam] at 300 hPa (isohypses) and geopotential height [gpdam] difference between 500hPa and 1000hPa (shaded color contours) - 22.03.2021 – 18 UTC.

2.3.2 Frontogenesis

Frontogenesis is the process by which a front forms, and it typically occurs when two air masses with different properties come into contact with each other. As the air masses interact, they begin to move and mix, and this can cause the formation of a front. Frontogenesis occurs when the temperature and humidity gradients across the front become stronger, leading to the development of a more distinct and well-defined front. Fronts and frontogenesis are important because their structures can specify a key role in the development of weather systems, such as thunderstorms or snowstorms. Besides, frontolysis refers to the process of a frontal boundary breaking down or dissipating, while frontogenesis refers to the opposite process, in which a frontal boundary forms or strengthens. Equation 2.11 indicates the 2D kinematic frontogenesis of a temperature field.

$$F = \frac{1}{2} |\nabla\theta| [D \cos(2\beta) - \delta] \quad (2.11)$$

F is 2D kinematic frontogenesis

θ is potential temperature

D is the total deformation

β is the angle between the axis of dilatation and the isentropes

δ is the divergence

The equation is used to identify frontogenesis and frontolysis over Eastern Mediterranean on the maps.

3. RESULTS AND DISCUSSION

3.1 Assessment of Recent Climatology and Synoptic Outlook

As moving into the winter season, the polar vortex needs to gather adequate amounts of cold air and store it throughout the stratosphere and the troposphere. The polar vortex in the Arctic region should be prioritized for cold air amplification.

The Rossby wave breaking exerts a drag on the Polar Night Jet, which causes it to weaken and distort as it travels through the stratosphere. The disruption of the stratospheric polar vortex that results from such a change in airflow can cause a split or displacement event in the polar vortex. When air subsequently does converge in the center of the vortex, it has no choice but to fall. This can typically bring about an event known as a sudden stratospheric warming (SSW). When the stratospheric zonal wind at 60 N north latitude (10hPa) becomes neutral or negative (east rather than west), it may occasionally cause cold spells to escape from the upper latitudes (polar region) to the mid latitudes. This could happen when the wind direction changes. In addition to this, it has the potential to play a crucial role in the development of extratropical cyclones, fronts, thunderstorms in the middle latitudes.

Apart from these, there are several teleconnections and atmospheric blocks which influence and dominate Europe in different time periods. Such as the Arctic Oscillation and the North Atlantic Oscillation must fluctuate between neutral and negative a couple times, which allows for wetter conditions over the Mediterranean Basin, particularly during the winter. In this way, polar originated air masses can reach midlatitudes and be dominated by ULLs, which bring frontal precipitation.

Jet streams in the troposphere are responsible for the separation of different air masses and the differences in temperature, precipitation, and other factors that result. This is how storm tracks form all over the North Atlantic. The jets are relatively undulating and buckle as the pattern changes. Numerous air masses have been positioned zonally and meridionally over Europe as a result of the movement of these patterns carried on

by westerlies. Therefore, on the European continent, high pressure over Scandinavia, which are called the Scandinavian Block, and can occur with the development of the Atlantic Ridge (AR), is an example of pressure settlements that can cause the EMEDO index to decrease (Fig. 3.1). This is due to the fact that much stronger jets tend to propagate across Mid-Europe and hold the Eastern Mediterranean area, allowing the ULL to deepen and the winds to strengthen. On the other hand, Greenland Block can cause the development of low level pressure system around contiguous Europe which is able to keep the Northwestern Europe countries within the colder airflow coming from Polar region. This settlement may result in a little ridge of high pressure over the middle Mediterranean and increase the value of EMEDO_i in the positive phase.

Especially, if AR forced by Azores High evolves to Scandinavian Block (BLO+) through Northwestern part of Europe, this pattern creates a favorable environment for frontal and convective storms over Eastern Mediterranean including Greece, Cyprus, and Turkey. The circulation of the strong high-pressure system promotes the development of a convergence area and ULL pressure system over mid-Eastern Europe. It curves the jet stream downward in between the two pressure systems, causing cold air to flow through southern latitudes. Looking at the overall year cycle, cold episodes with ULL appear to occur mostly during the northern hemisphere winter period. For this reason, negative phases are apparent and prominent for the Euro-Mediterranean region during the winter months, with the most common period from October to May (Fig. 3.2).

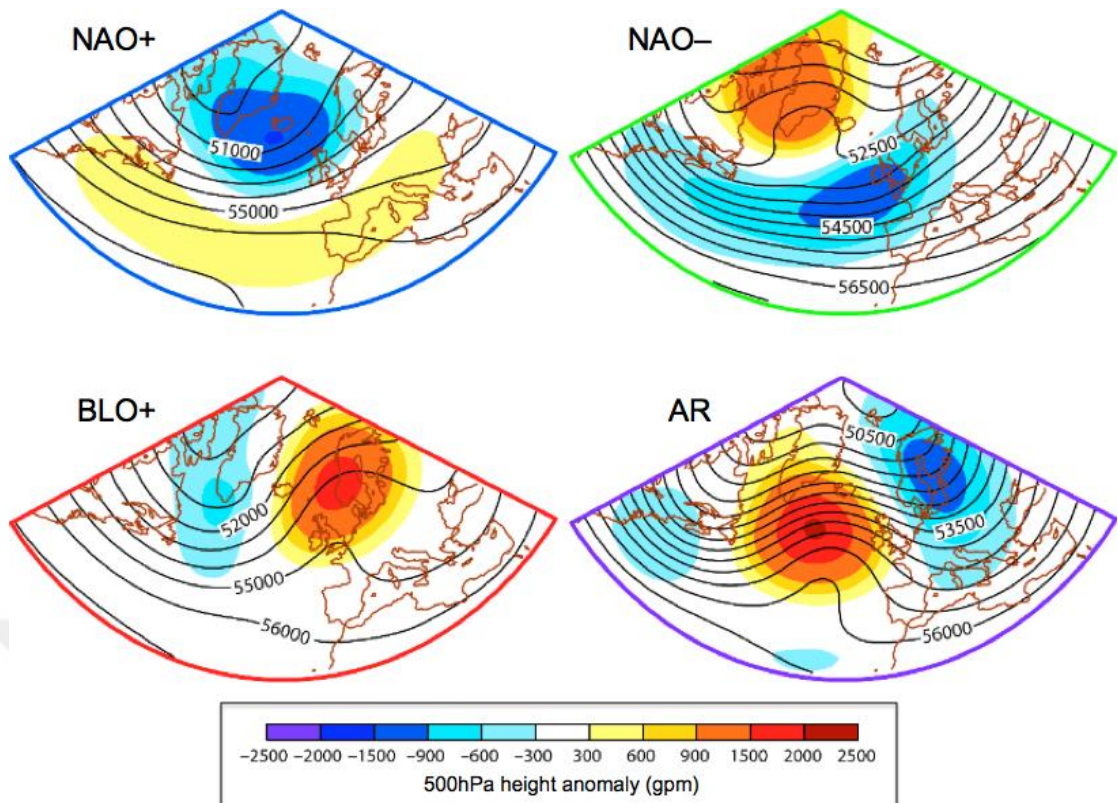


Figure 3.1 : Diagrams depict the Euro-Atlantic sector around which the regime definitions of geographical patterns of Euro-Atlantic climatological regimes (both anomalies and full fields) as used at ECMWF. North Atlantic Oscillation, positive phase (NAO+), North Atlantic Oscillation, negative phase (NAO-), Blocking (BLO+), The Atlantic Ridge (AR) circulation pattern is a particular case of Anti-blocking (BLO-), in which the important feature is the trough over Scandinavia. Geopotential anomalies (color shading) and geopotential (contours) at 500 hPa are shown (Cassou, 2010).

Besides all these, a negative skew will indicate a tail on the left side and will extend to the more negative side. According to the analysis of Fisher-Pearson standardized coefficients, EMEDO_i has severe left skewness for all the year periods and they should be optimized to have normal distribution or the formula might be updated. EMEDO_i of all year periods has been observed that the distribution has a thicker left tail and mode > median > mean.



Figure 3.2 : The values of EMEDO-Oper indices in 6-h temporal resolution during based on the years of 2015-2021 climatological period, percentage distributions of EMEDO_i during the years (upper center), and adjusted Fisher-Pearson standardized moment coefficients (upper left).

3.2 Analysis of Imminent Tornadoic Storm Environment in the Scope EMEDO_i & Fronts in Eastern Mediterranean

The all variation of EMEDO indices were analysed in the range of 10 days which is from 5-day before ($t-5$) to 4-day after ($t+4$) the event day. The figures plotted below, which is based on geopotential heights and frontogenesis additional to the EMEDO indices, will be used to examine 14 separate tornado events (trained clusters) according to the their EMEDO indice local minimum times.

The movement of a cold front system, which is formed by the effect of the cyclonic vorticity field on the Mediterranean over a wide area, draws attention. The time at which the tornado event occurred coincides with the minimum peak time of the EMEDO-Oper index. In this event, the EMEDO_i reached a value of less than -10, which indicates how deep a trough the ULL is in the central Mediterranean (Fig. 3.3). Also, since the relatively low EMEDO₃ index is related to the value at the P3 point on

the western part of the trough, it indicates that the trough oscillates in the vertical direction directly from the side close to Italy to the southern latitudes.

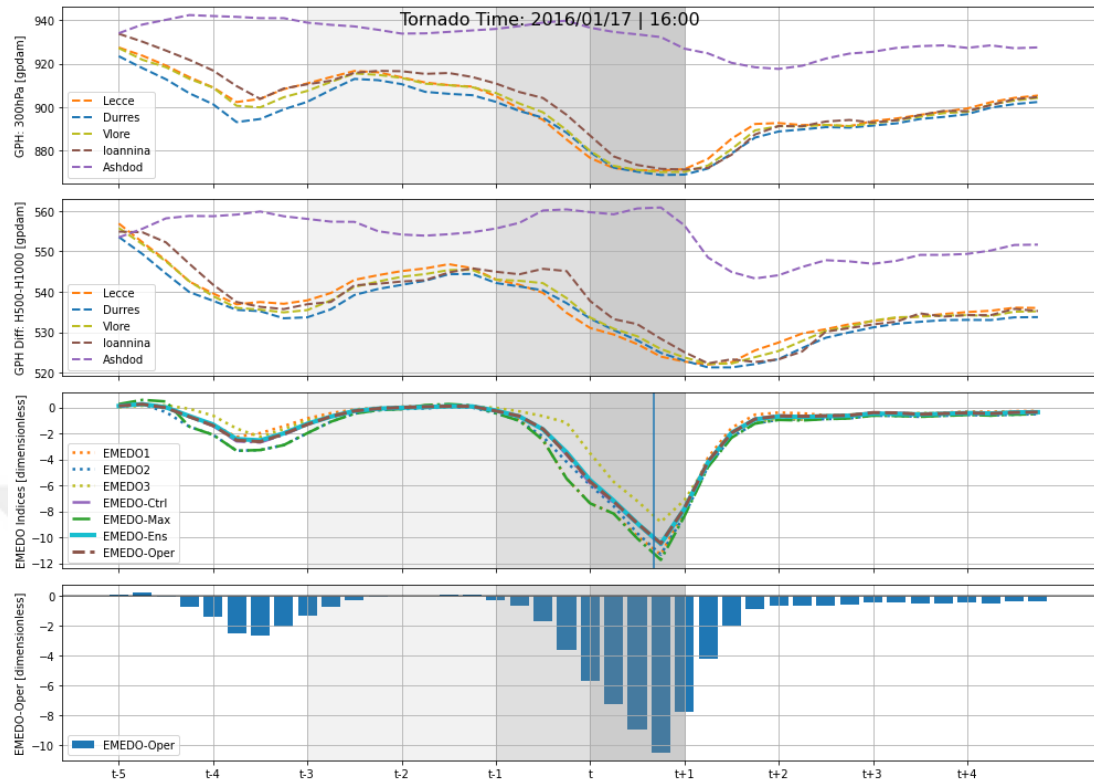


Figure 3.3 : 10-days all EMEDO member oscillations (the vertical axis) surrounding tornado incidents in daily period (the horizontal axis) (17.01.2016). The lightest shaded areas indicate 1 to 3 days before the tornado event of EMEDO_i members, whereas the darkest shaded parts indicate the days when EMEDO_i members begin developing negatively. The area with the most opaque color depicts the day of the tornado (top). Geopotential height [gpdam] at 300 hPa (isohypses) and geopotential height [gpdam] difference between 500hPa and 1000hPa (shaded color contours) (middle). Near-surface (925 hPa) horizontal frontogenesis function [K/100km/3h] (bottom).

In this incident (Fig 3.4), ULL entering from a narrower area created a relatively strong positive vorticity advection. The EMEDO-Oper value reached a magnitude less than -4 and persisted around this value for a long time (approximately 12 hours). It is possible to interpret this as the trough gathering strength and remaining motionless. The hour when the hose came out occurred during the hours when the EMEDO values started to decrease with a high tendency value. Lower geopotential heights around the surrounding air are indicated on one of the reference points at the western polar caps.

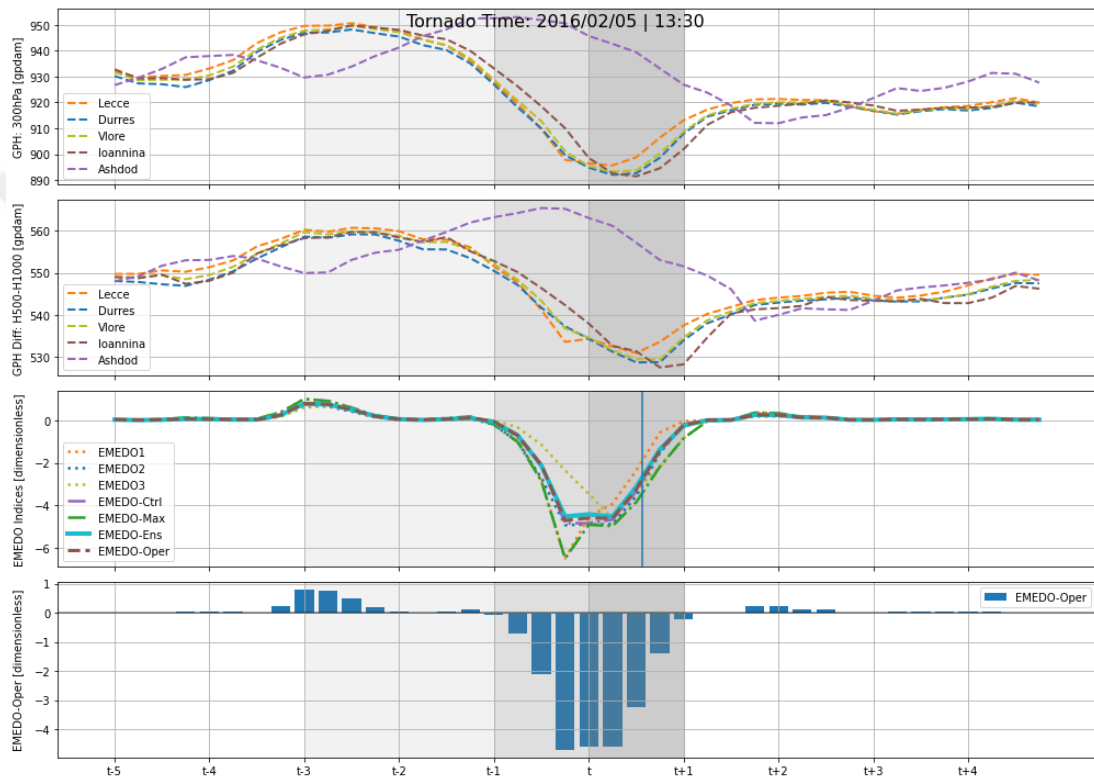


Figure 3.4 : 10-days all EMEDO member oscillations (the vertical axis) surrounding tornado incidents in daily period (the horizontal axis) (05.02.2016). The lightest shaded areas indicate 1 to 3 days before the tornado event of EMEDO_i members, whereas the darkest shaded parts indicate the days when EMEDO_i members begin developing negatively. The area with the most opaque color depicts the day of the tornado (top). Geopotential height [gpdam] at 300 hPa (isohypses) and geopotential height [gpdam] difference between 500hPa and 1000hPa (shaded color contours) (middle). Near-surface(925 hPa) horizontal frontogenesis function[K/100km/3h] (bottom).

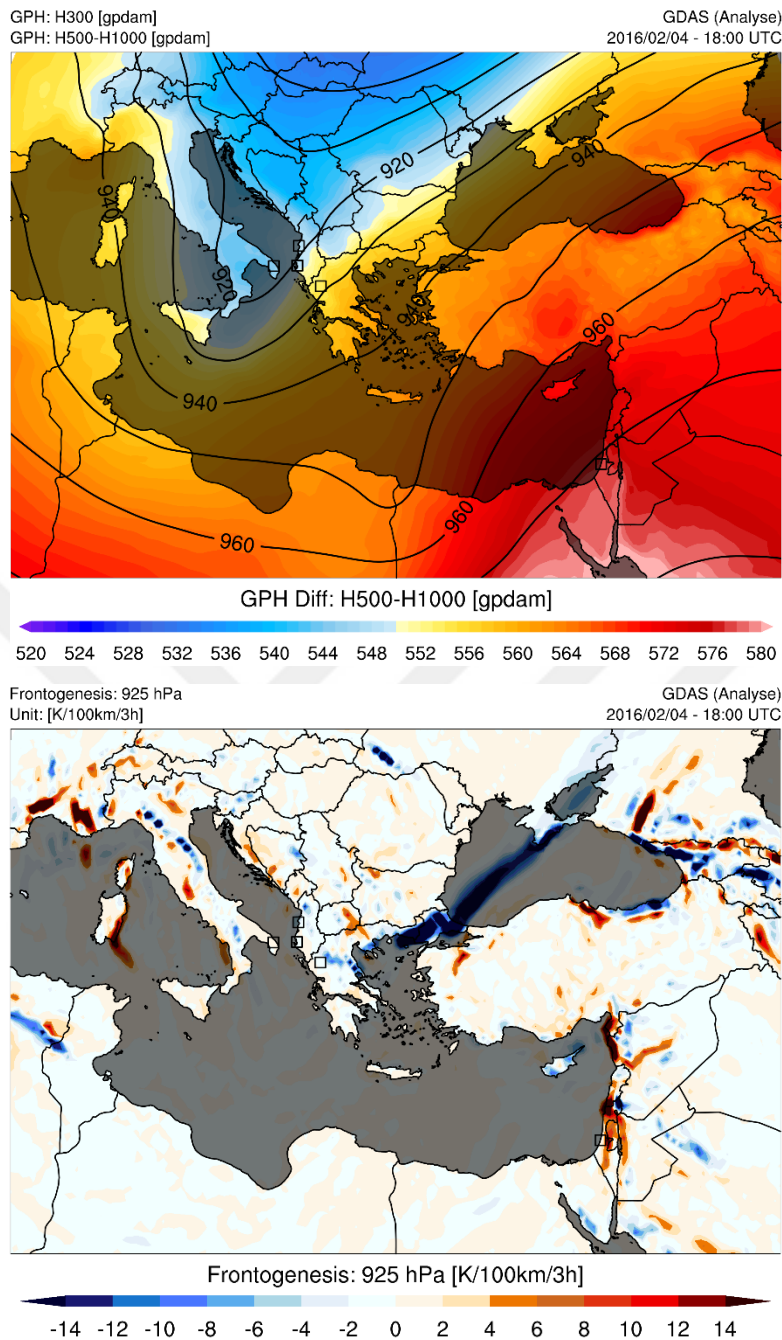


Figure 3.4 (continued): 10-days all EMEDO member oscillations (the vertical axis) surrounding tornado incidents in daily period (the horizontal axis) (05.02.2016). The lightest shaded areas indicate 1 to 3 days before the tornado event of EMEDO_i members, whereas the darkest shaded parts indicate the days when EMEDO_i members begin developing negatively. The area with the most opaque color depicts the day of the tornado (top). Geopotential height [gpdam] at 300 hPa (isohypses) and geopotential height [gpdam] difference between 500hPa and 1000hPa (shaded color contours) (middle). Near-surface(925 hPa) horizontal frontogenesis function[K/100km/3h] (bottom).

Prior to the event, the EMEDO-Max value was less than -6. And when the graph is examined carefully, it is clearly seen that the EMEDO-Oper index value, which is almost reaching the value of -5, returns to the neutral phase within 24 hours. This shows us that the ULL, which was stagnant at first, moved rapidly to the east in the following hours.

The instability that occurred between two consecutive fluctuations was the cause of the tornado that was depicted in Figure 3.5. As a result of this instability, the EMEDO-Oper value reached a minimum peak of -6. The EMEDO-3 value is relatively near to the P0 point, whereas the other EMEDO variations are relatively low. This is due to the fact that the flowing upstream trough occupies such a large area.

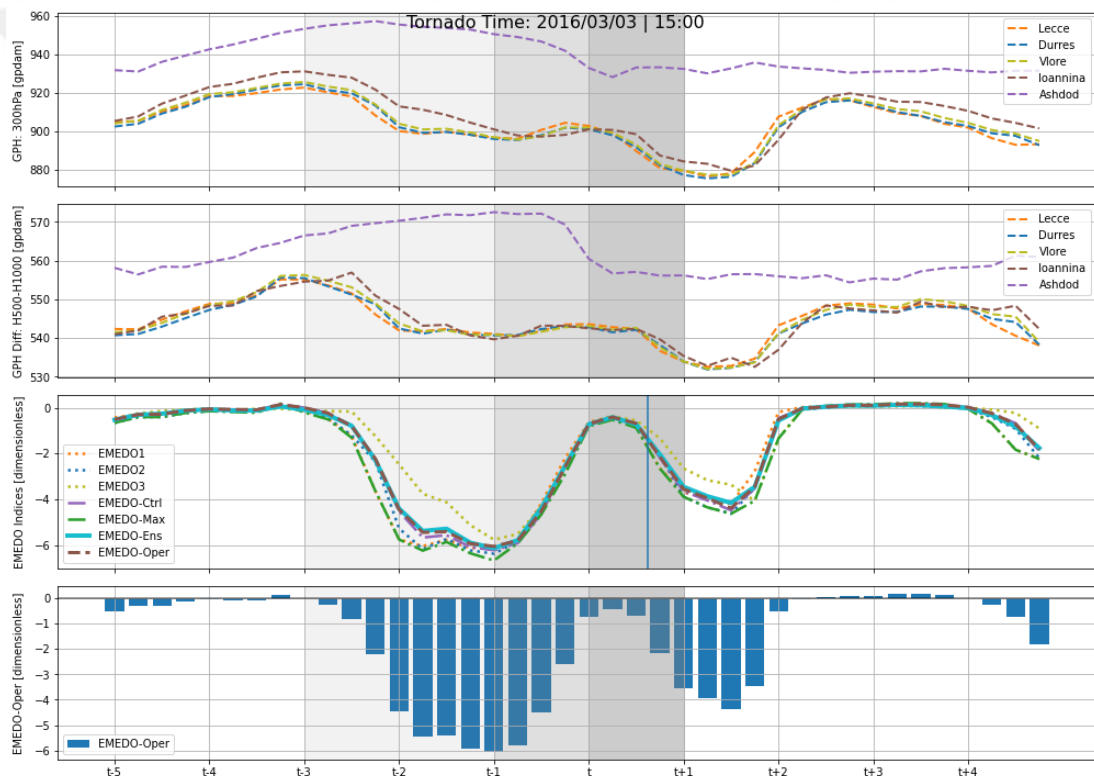


Figure 3.5 : 10-days all EMEDO member oscillations (the vertical axis) surrounding tornado incidents in daily period (the horizontal axis) (03.03.2016). The lightest shaded areas indicate 1 to 3 days before the tornado event of EMEDOi members, whereas the darkest shaded parts indicate the days when EMEDOi members begin developing negatively. The area with the most opaque color depicts the day of the tornado (top). Geopotential height [gpdam] at 300 hPa (isohypses) and geopotential height [gpdam] difference between 500hPa and 1000hPa (shaded color contours) (middle). Near-surface(925 hPa) horizontal frontogenesis function[K/100km/3h] (bottom).

The most important difference of this system is that the main ULL zone is located further west than the EMEDO western pole (Fig 3.6). Although it seems like a skeptical system synoptically, the EMEDO-Oper value approached -1 in the condition that produced the most severe event of recent years at the F3 level. Also, in this incident, a low-pressure system with semi-cut-off support, which moved with the front on the Mediterranean, left the main system and struck Turkiye again from Africa. The fact that the tornado, which emerged during the decrease in tendency, fell to a height of 900 gpdam at the jet level reveals that the groove hit Turkiye in a fragmented manner.

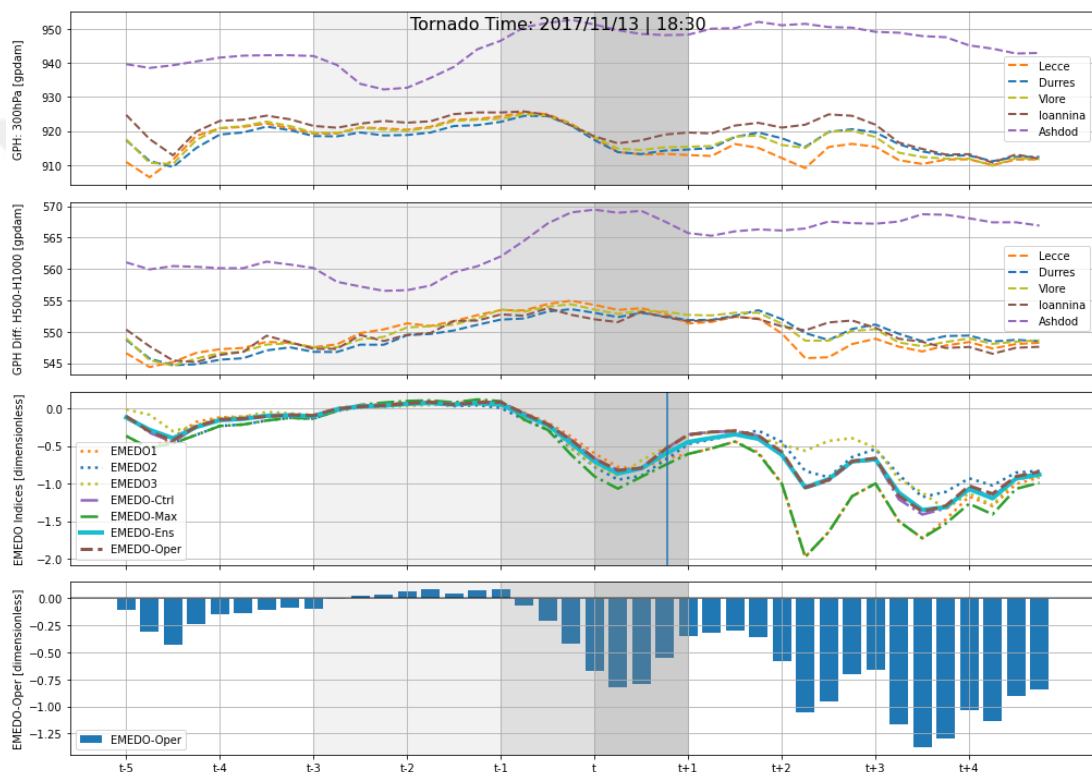


Figure 3.6 : 10-days all EMEDO member oscillations (the vertical axis) surrounding tornado incidents in daily period (the horizontal axis) (13.11.2017). The lightest shaded areas indicate 1 to 3 days before the tornado event of EMEDO_i members, whereas the darkest shaded parts indicate the days when EMEDO_i members begin developing negatively. The area with the most opaque color depicts the day of the tornado (top). Geopotential height [gpdam] at 300 hPa (isohypses) and geopotential height [gpdam] difference between 500hPa and 1000hPa (shaded color contours) (middle). Near-surface (925 hPa) horizontal frontogenesis function [K/100km/3h] (bottom).

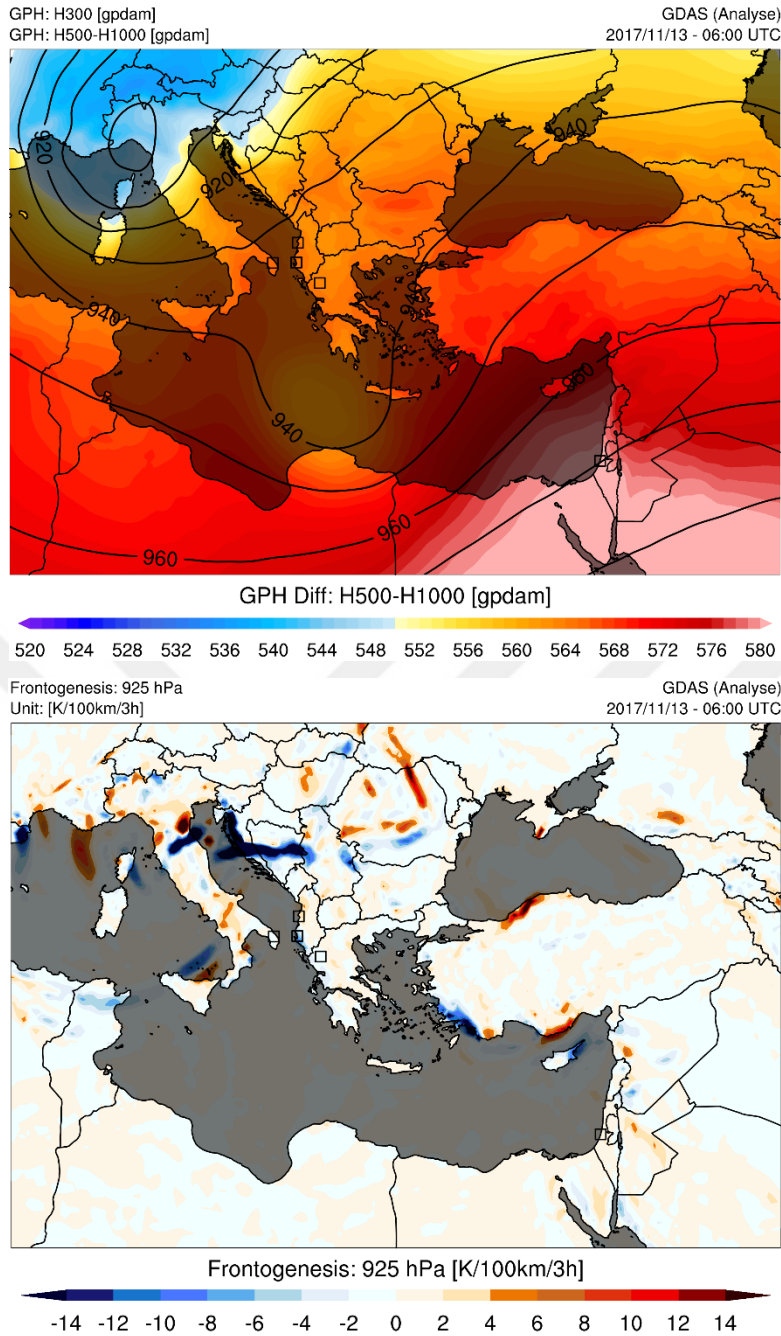


Figure 3.6 (continued): 10-days all EMEDO member oscillations (the vertical axis) surrounding tornado incidents in daily period (the horizontal axis) (13.11.2017). The lightest shaded areas indicate 1 to 3 days before the tornado event of EMEDO_i members, whereas the darkest shaded parts indicate the days when EMEDO_i members begin developing negatively. The area with the most opaque color depicts the day of the tornado (top). Geopotential height [gpdam] at 300 hPa (isohypses) and geopotential height [gpdam] difference between 500hPa and 1000hPa (shaded color contours) (middle). Near-surface (925 hPa) horizontal frontogenesis function [K/100km/3h] (bottom).

For this event (Fig 3.7), Western Europe is being affected by Diffluent block. A split in the eastwards flow can lead to a Diffluent block. Examples with a closed high center to the north of a closed low center in the south are more likely to last for a prolonged period of time. When the EMEDO-Oper index reached close to -0.25, again in the afternoon with local time, there was a tornado. After the system had been running for 6 hours, the values began to approach zero and transitioned into the neutral phase.

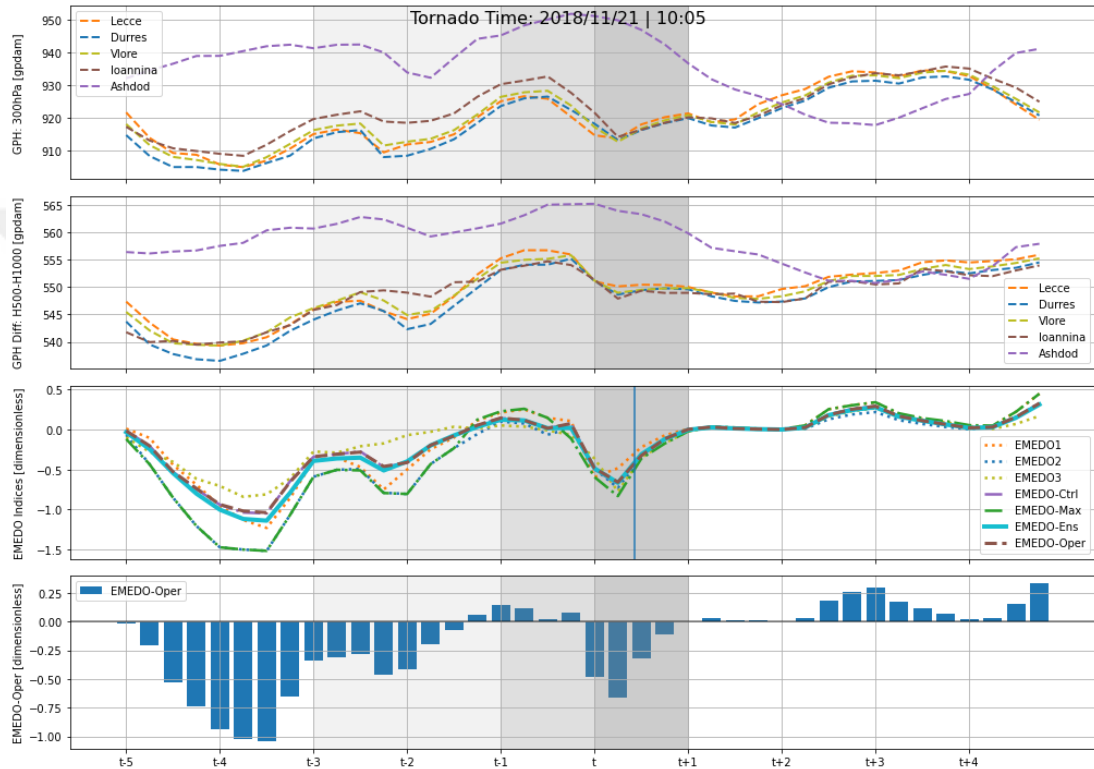


Figure 3.7 : 10-days all EMEDO member oscillations (the vertical axis) surrounding tornado incidents in daily period (the horizontal axis) (21.11.2018). The lightest shaded areas indicate 1 to 3 days before the tornado event of EMEDO_i members, whereas the darkest shaded parts indicate the days when EMEDO_i members begin developing negatively. The area with the most opaque color depicts the day of the tornado (top). Geopotential height [gpdam] at 300 hPa (isohypses) and geopotential height [gpdam] difference between 500hPa and 1000hPa (shaded color contours) (middle). Near-surface (925 hPa) horizontal frontogenesis function [K/100km/3h] (bottom).

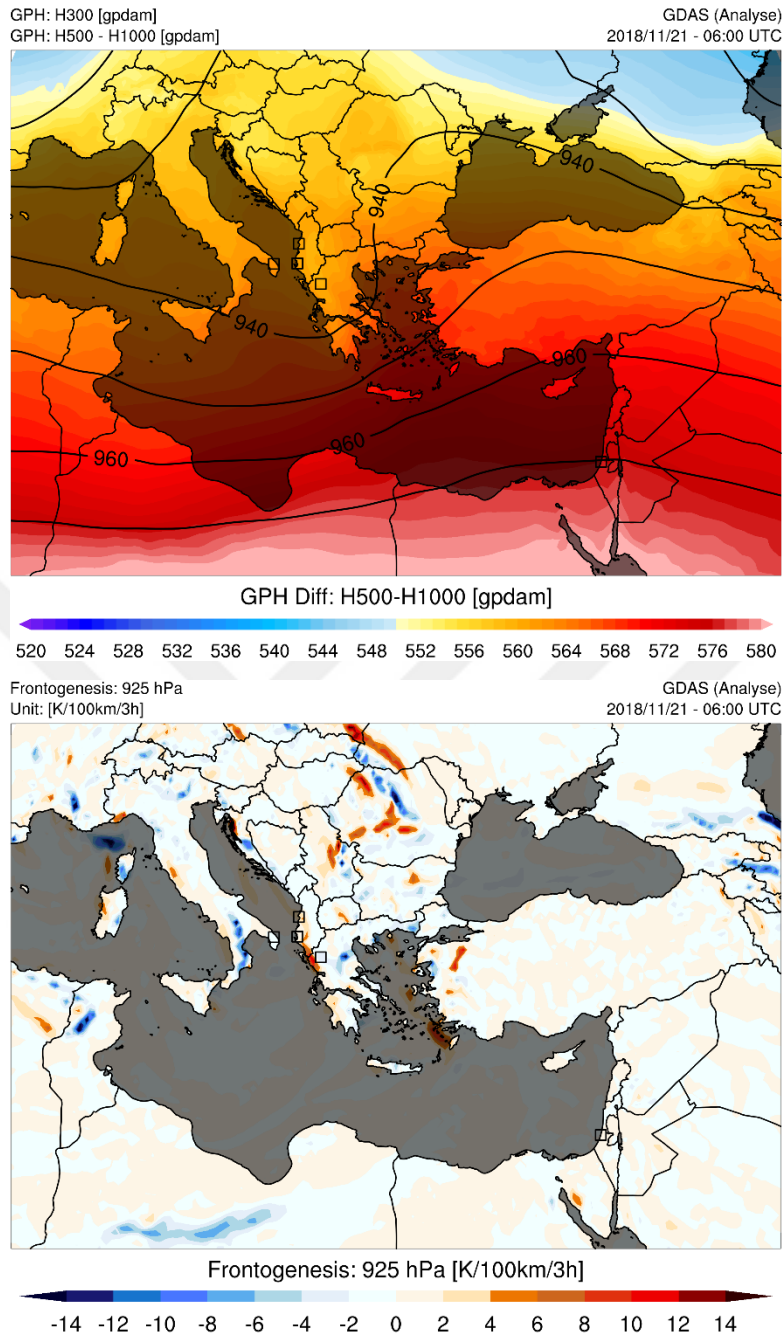


Figure 3.7 (continued): 10-days all EMEDO member oscillations (the vertical axis) surrounding tornado incidents in daily period (the horizontal axis) (21.11.2018). The lightest shaded areas indicate 1 to 3 days before the tornado event of EMEDO_i members, whereas the darkest shaded parts indicate the days when EMEDO_i members begin developing negatively. The area with the most opaque color depicts the day of the tornado (top). Geopotential height [gpdam] at 300 hPa (isohypses) and geopotential height [gpdam] difference between 500hPa and 1000hPa (shaded color contours) (middle). Near-surface (925 hPa) horizontal frontogenesis function [K/100km/3h] (bottom).

Systems in which the temperature difference at the jet level between the EMEDO poles was at its greatest gave rise to the supercell thunderstorms and accompanying SCSs that occurred during this week and the week that followed (Fig 3.8). Within eighteen hours, the EMEDO-Oper index, which had been hovering dangerously close to the value of -3, moved on to the neutral phase, and this was one of the ULL systems with the quickest transition times observed.

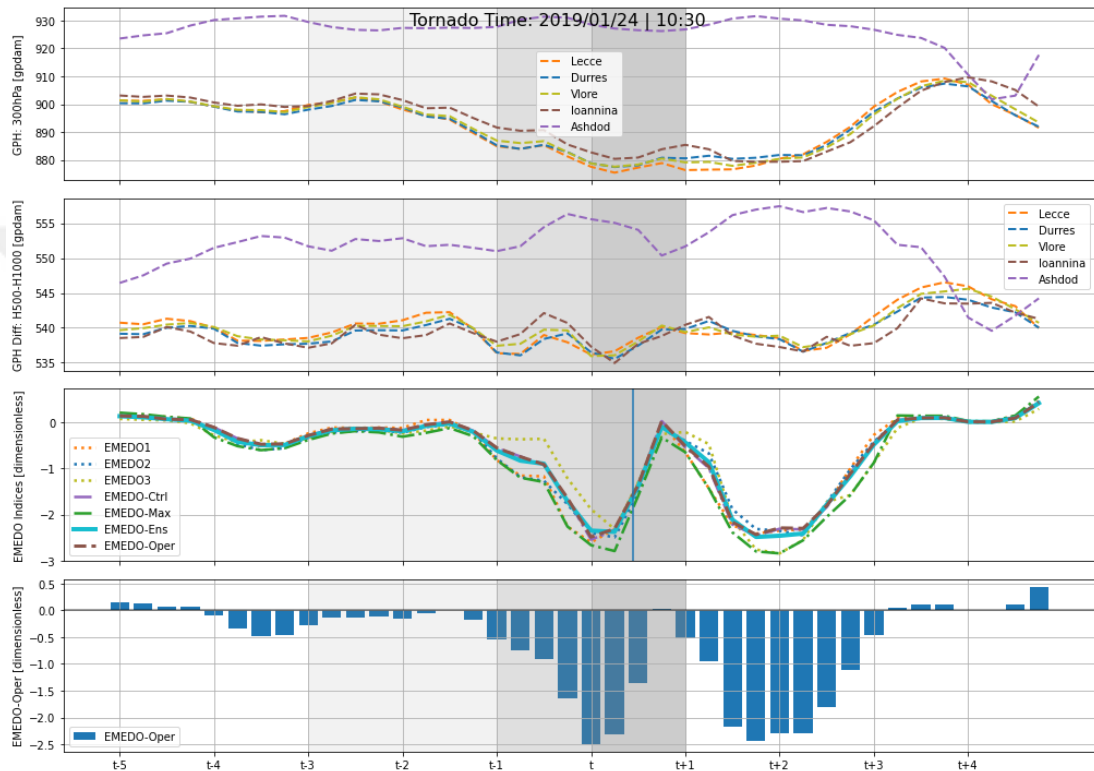


Figure 3.8 : 10-days all EMEDO member oscillations (the vertical axis) surrounding tornado incidents in daily period (the horizontal axis) (24.01.2019). The lightest shaded areas indicate 1 to 3 days before the tornado event of EMEDO_i members, whereas the darkest shaded parts indicate the days when EMEDO_i members begin developing negatively. The area with the most opaque color depicts the day of the tornado (top). Geopotential height [gpdam] at 300 hPa (isohypses) and geopotential height [gpdam] difference between 500hPa and 1000hPa (shaded color contours) (middle). Near-surface (925 hPa) horizontal frontogenesis function [K/100km/3h] (bottom).

In the second ULL push, as a continuation of the previous event, which is a continuation of the previous system, the long suspended trough triggered the reaction low pressure over the Mediterranean, resulting in a cold front developing and moving from Greece to Turkiye (Fig 3.9). The main system, which remained stable on Italy, evolved into the occlusion and seclusion phase. While the EMEDO-Oper index remained below -2 for twenty-four hours and subsequently swiftly approached the neutral phase, the tornado event moved towards land while it was over the sea.

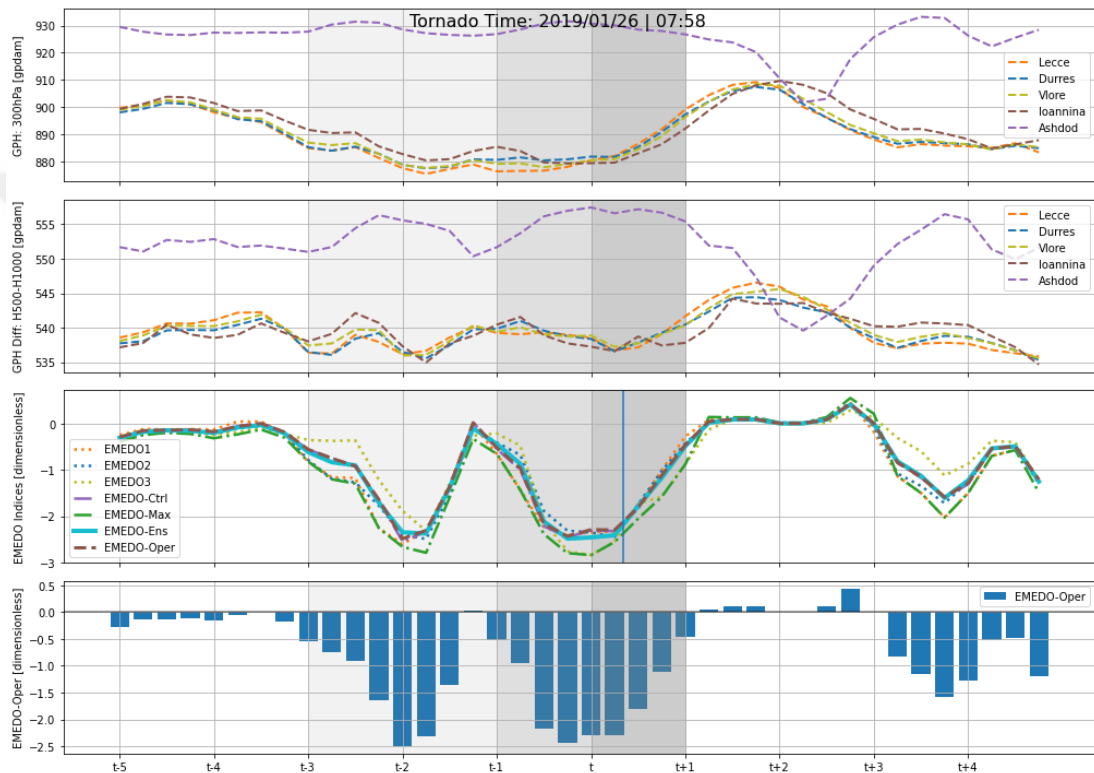


Figure 3.9 : 10-days all EMEDO member oscillations (the vertical axis) surrounding tornado incidents in daily period (the horizontal axis) (26.01.2019). The lightest shaded areas indicate 1 to 3 days before the tornado event of EMEDO_i members, whereas the darkest shaded parts indicate the days when EMEDO_i members begin developing negatively. The area with the most opaque color depicts the day of the tornado (top). Geopotential height [gpdam] at 300 hPa (isohypses) and geopotential height [gpdam] difference between 500hPa and 1000hPa (shaded color contours) (middle). Near-surface (925 hPa) horizontal frontogenesis function [K/100km/3h] (bottom).

Compared to other ULL systems, the trough descending from further west to southern latitudes brought blizzards to many northern terrestrial cities (Fig 3.10). In parallel with this, cities that are located on a relatively warm sea and whose freezing level values are not sufficient for snow experience the danger of tornadoes. The relatively slow-moving ULL took approximately 36 hours to bring the EMEDO-Oper index from around -1 to neutral phase.

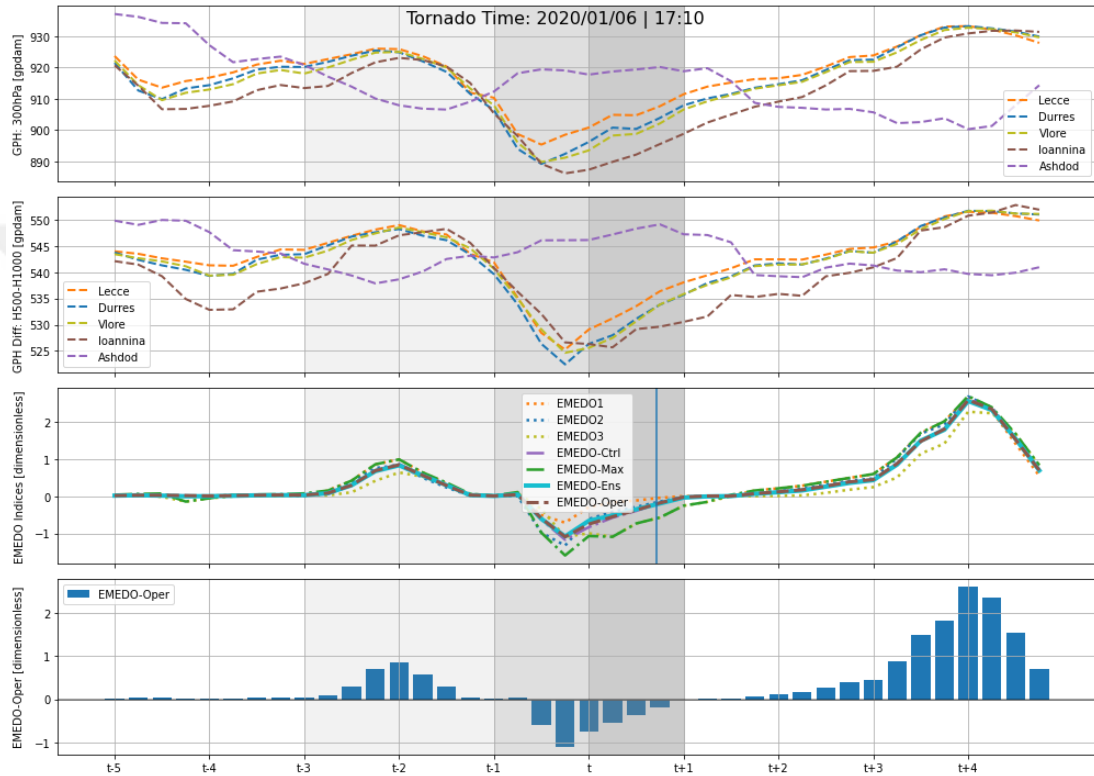


Figure 3.10 : 10-days all EMEDO member oscillations (the vertical axis) surrounding tornado incidents in daily period (the horizontal axis) (06.01.2020). The lightest shaded areas indicate 1 to 3 days before the tornado event of EMEDOi members, whereas the darkest shaded parts indicate the days when EMEDOi members begin developing negatively. The area with the most opaque color depicts the day of the tornado (top). Geopotential height [gpdam] at 300 hPa (isohypses) and geopotential height [gpdam] difference between 500hPa and 1000hPa (shaded color contours) (middle). Near-surface (925 hPa) horizontal frontogenesis function [K/100km/3h] (bottom).

The cold front was moving southeast over the Balkans when it interacted with the Marmara Sea, which was unusually warm for the time of year (Fig 3.11). The occurrence continued to take place as soon as the index value, which had reached its highest point during the negative phase, began its steepest descent. In this system that moves at a somewhat modest pace, it took about 42 hours for the EMEDO-Oper index to reach neutral phase after starting at a value of -1.5.

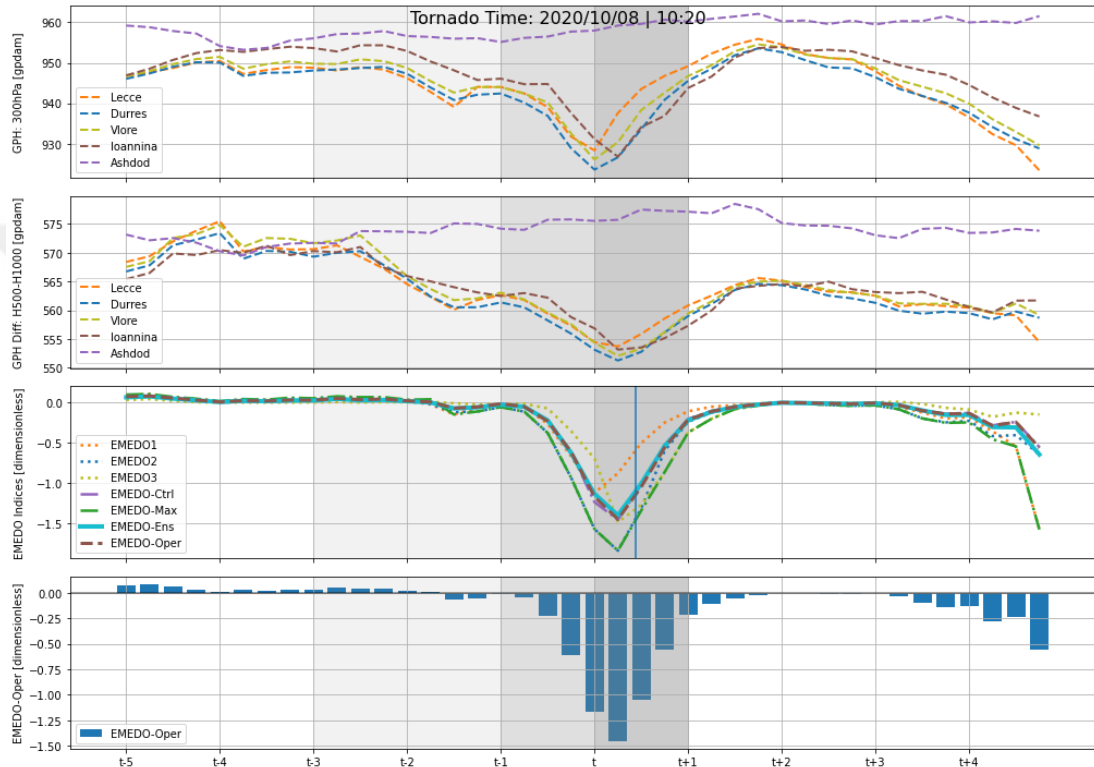


Figure 3.11 : 10-days all EMEDO member oscillations (the vertical axis) surrounding tornado incidents in daily period (the horizontal axis) (08.10.2020). The lightest shaded areas indicate 1 to 3 days before the tornado event of EMEDO_i members, whereas the darkest shaded parts indicate the days when EMEDO_i members begin developing negatively. The area with the most opaque color depicts the day of the tornado (top). Geopotential height [gpdam] at 300 hPa (isohypses) and geopotential height [gpdam] difference between 500hPa and 1000hPa (shaded color contours) (middle). Near-surface (925 hPa) horizontal frontogenesis function [K/100km/3h] (bottom).

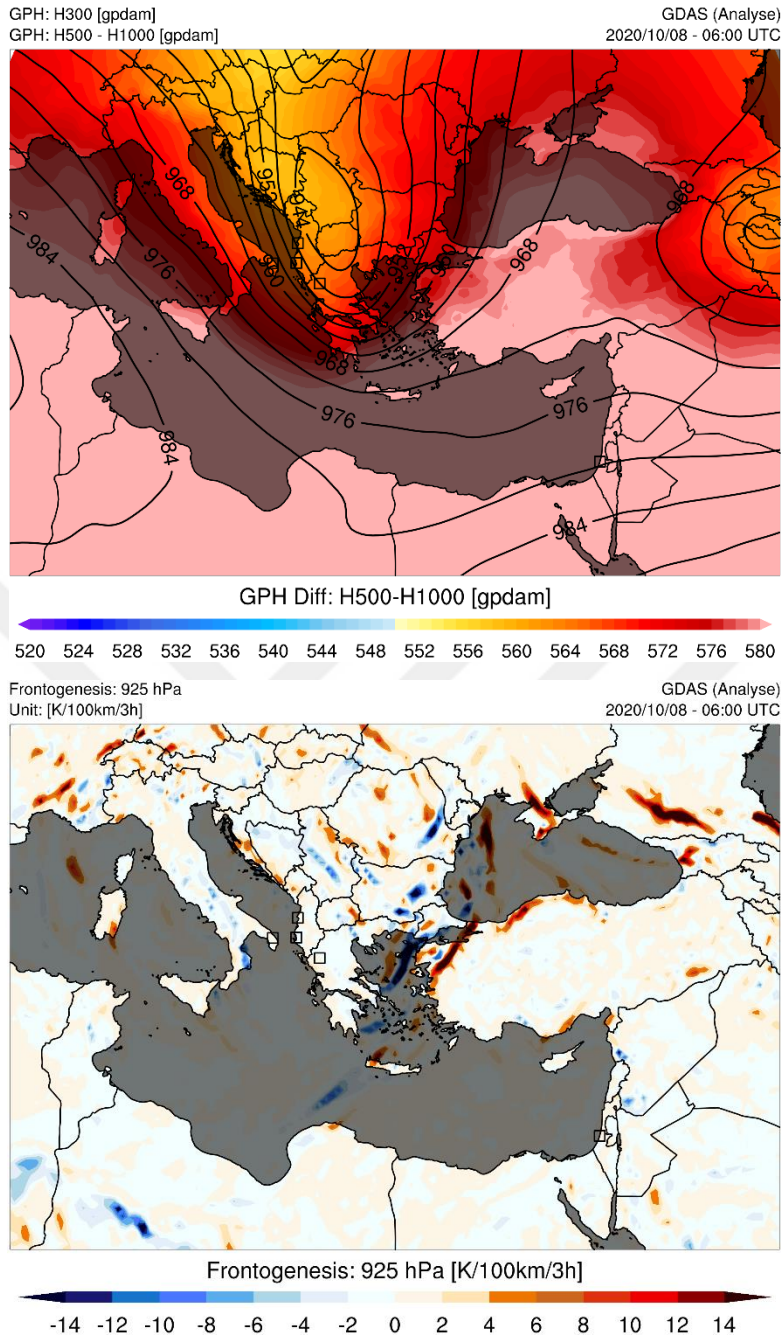


Figure 3.11 (continued): 10-days all EMEDO member oscillations (the vertical axis) surrounding tornado incidents in daily period (the horizontal axis) (08.10.2020). The lightest shaded areas indicate 1 to 3 days before the tornado event of EMEDO_i members, whereas the darkest shaded parts indicate the days when EMEDO_i members begin developing negatively. The area with the most opaque color depicts the day of the tornado (top). Geopotential height [gpdam] at 300 hPa (isohypses) and geopotential height [gpdam] difference between 500hPa and 1000hPa (shaded color contours) (middle). Near-surface (925 hPa) horizontal frontogenesis function [K/100km/3h] (bottom).

At the point when a distinctive cold front passes through the warm front, the dynamics of the storm were at their most potent (Fig 3.12). Over the span of time, the occlusion over the Black Sea evolved into a front. The EMEDO-Oper value, which was very close to hitting -11, arrived in the neutral phase within thirty-six hours, and the incident occurred at the point where the indices peak.

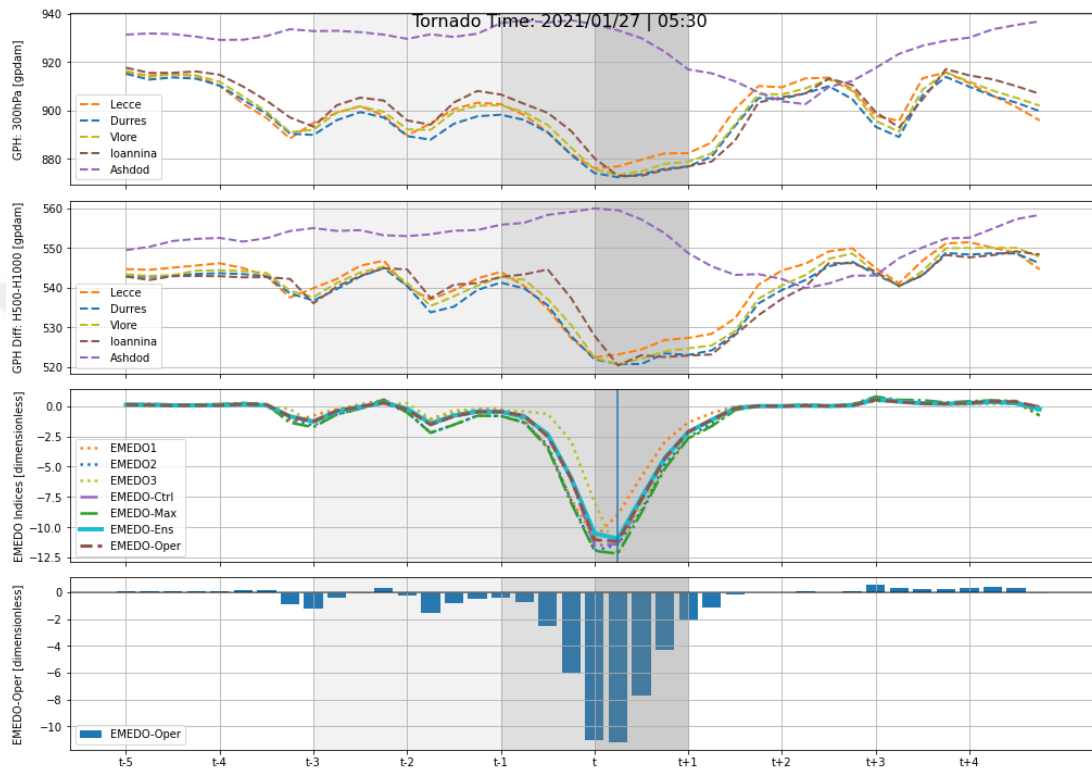
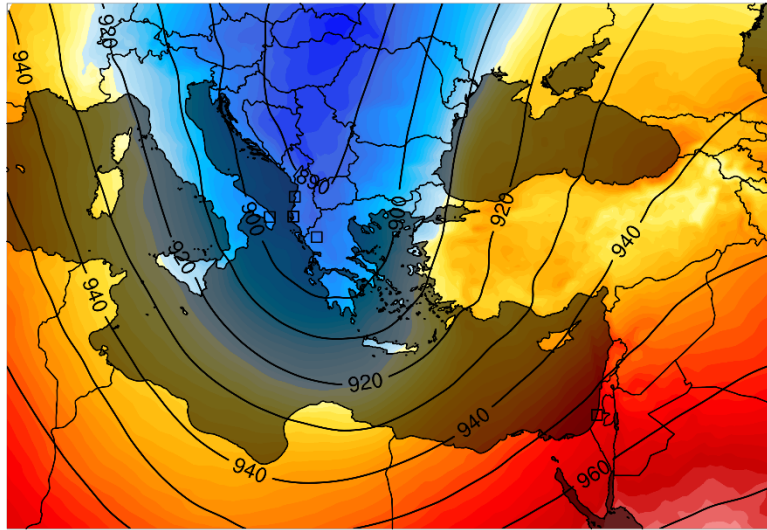


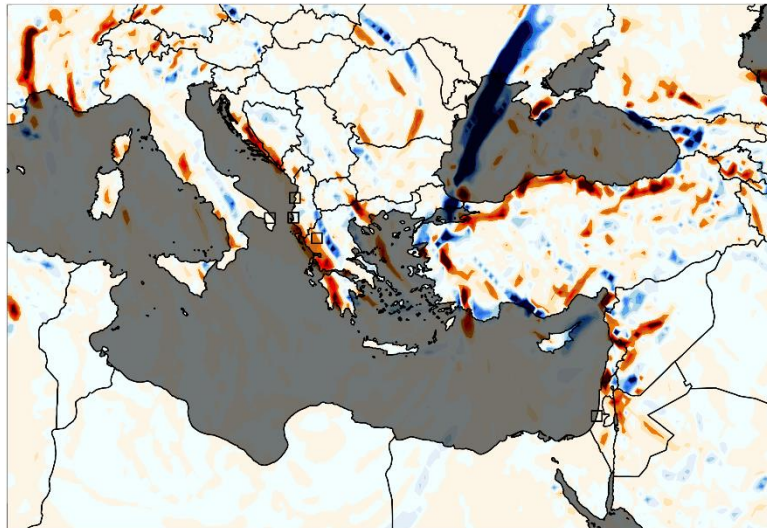
Figure 3.12 : 10-days all EMEDO member oscillations (the vertical axis) surrounding tornado incidents in daily period (the horizontal axis) (27.01.2021). The lightest shaded areas indicate 1 to 3 days before the tornado event of EMEDO_i members, whereas the darkest shaded parts indicate the days when EMEDO_i members begin developing negatively. The area with the most opaque color depicts the day of the tornado (top). Geopotential height [gpdam] at 300 hPa (isohypses) and geopotential height [gpdam] difference between 500hPa and 1000hPa (shaded color contours) (middle). Near-surface (925 hPa) horizontal frontogenesis function [K/100km/3h] (bottom).

GPH: H300 [gpdam] GDAS (Analyse)
 GPH: H500 - H1000 [gpdam] 2021/01/27 - 06:00 UTC



GPH Diff: H500-H1000 [gpdam]
 520 524 528 532 536 540 544 548 552 556 560 564 568 572 576 580

Frontogenesis: 925 hPa GDAS (Analyse)
 Unit: [K/100km/3h] 2021/01/27 - 06:00 UTC



Frontogenesis: 925 hPa [K/100km/3h]
 -14 -12 -10 -8 -6 -4 -2 0 2 4 6 8 10 12 14

Figure 3.12 (continued): 10-days all EMEDO member oscillations (the vertical axis) surrounding tornado incidents in daily period (the horizontal axis) (27.01.2021). The lightest shaded areas indicate 1 to 3 days before the tornado event of EMEDO_i members, whereas the darkest shaded parts indicate the days when EMEDO_i members begin developing negatively. The area with the most opaque color depicts the day of the tornado (top). Geopotential height [gpdam] at 300 hPa (isohypses) and geopotential height [gpdam] difference between 500hPa and 1000hPa (shaded color contours) (middle). Near-surface (925 hPa) horizontal frontogenesis function [K/100km/3h] (bottom).

The cold front moved from Greece to Turkiye and swept the Aegean Sea in a zonal direction (Fig 3.13). The geopotential isohypses moved very frequently, triggering the ground-level convergence field. In addition to the fact that the EMEDO-Oper index went from roughly -2 to the neutral phase, the tornado occurrence happened during the period when the index declined in this system, which lasted for a total of thirty hours.

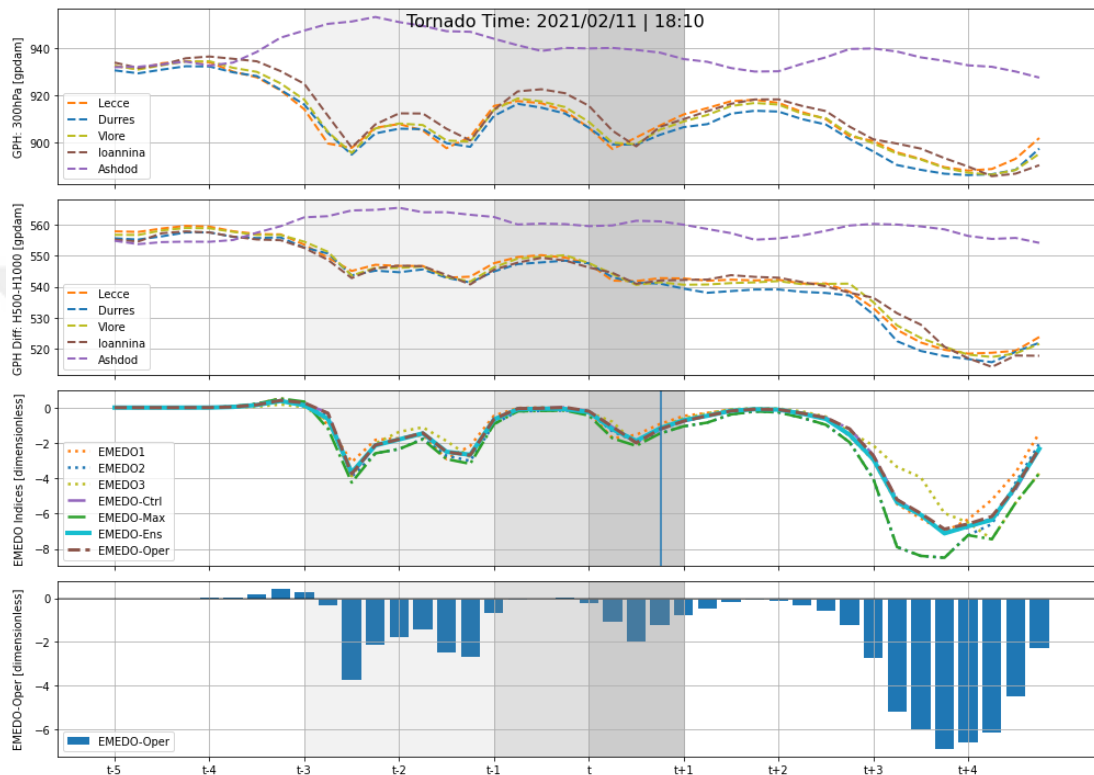


Figure 3.13 : 10-days all EMEDO member oscillations (the vertical axis) surrounding tornado incidents in daily period (the horizontal axis) (11.02.2021). The lightest shaded areas indicate 1 to 3 days before the tornado event of EMEDOi members, whereas the darkest shaded parts indicate the days when EMEDOi members begin developing negatively. The area with the most opaque color depicts the day of the tornado (top). Geopotential height [gpdam] at 300 hPa (isohypses) and geopotential height [gpdam] difference between 500hPa and 1000hPa (shaded color contours) (middle). Near-surface (925 hPa) horizontal frontogenesis function [K/100km/3h] (bottom).

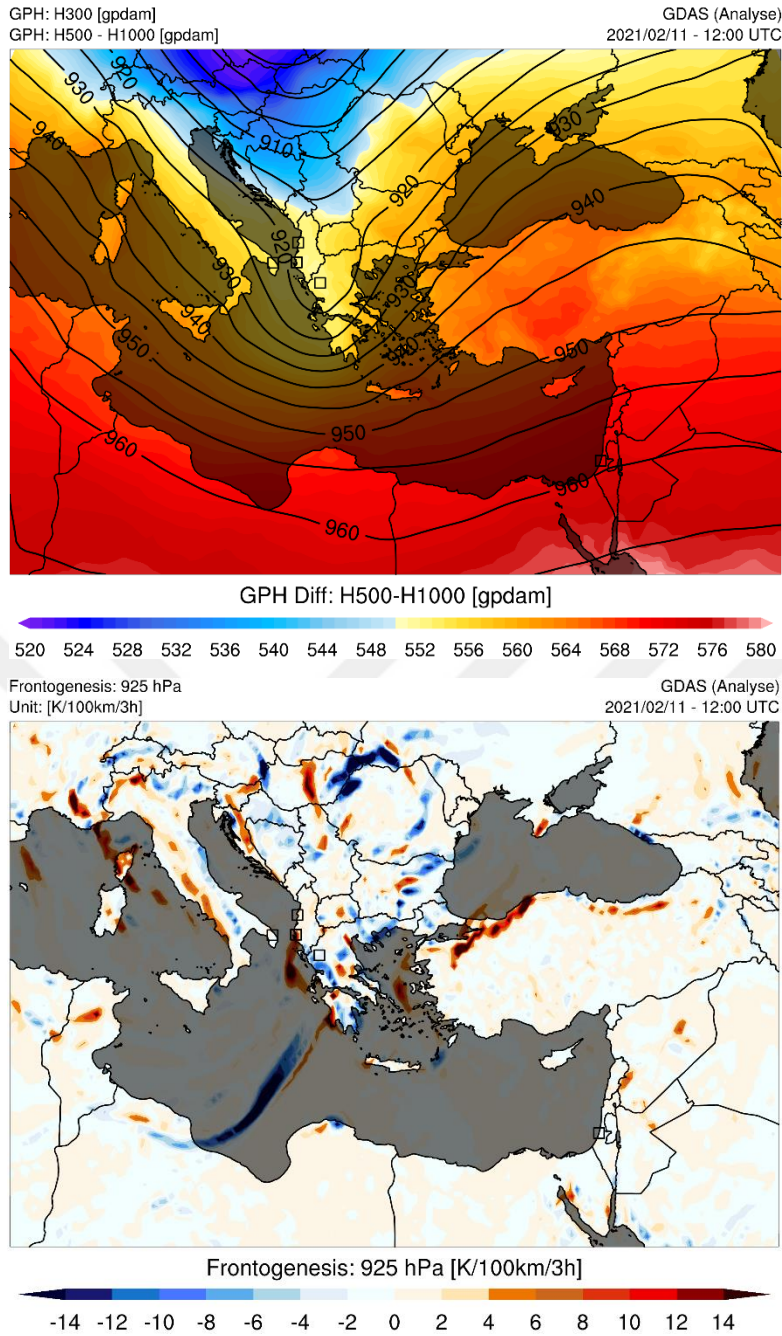


Figure 3.13 (continued): 10-days all EMEDO member oscillations (the vertical axis) surrounding tornado incidents in daily period (the horizontal axis) (11.02.2021). The lightest shaded areas indicate 1 to 3 days before the tornado event of EMEDO_i members, whereas the darkest shaded parts indicate the days when EMEDO_i members begin developing negatively. The area with the most opaque color depicts the day of the tornado (top). Geopotential height [gpdam] at 300 hPa (isohypses) and geopotential height [gpdam] difference between 500hPa and 1000hPa (shaded color contours) (middle). Near-surface (925 hPa) horizontal frontogenesis function [K/100km/3h] (bottom).

It is a system that developed as a result of a cold spell from Central Europe to the Mediterranean basin (Fig 3.14). Cyclonic relative vorticity values are quite high although they are effective in narrow spaces. All indices of EMEDO, which remained negative for a long time, prove that the ULL is suspended in the blocking effect. While the EMEDO-Oper index value, which reached -3 in the series, constituted the strongest part of severe convective storms, the tornado incident also emerged in the continuation of the decline.

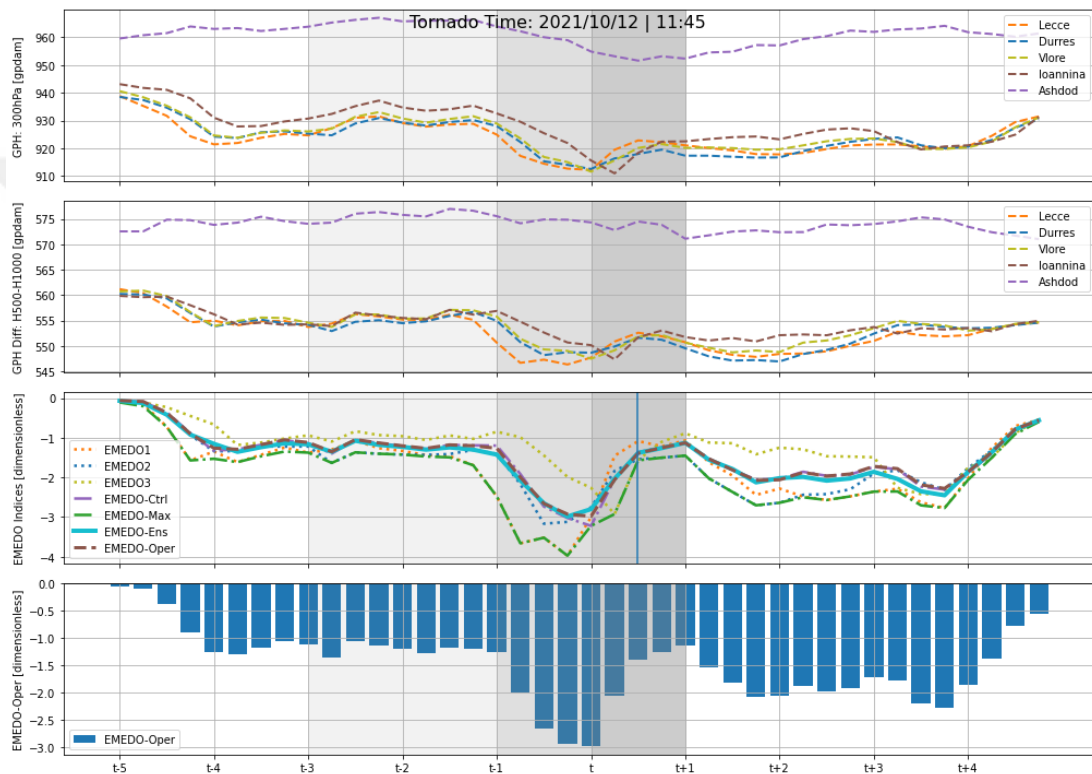


Figure 3.14 : 10-days all EMEDO member oscillations (the vertical axis) surrounding tornado incidents in daily period (the horizontal axis) (12.10.2021). The lightest shaded areas indicate 1 to 3 days before the tornado event of EMEDO_i members, whereas the darkest shaded parts indicate the days when EMEDO_i members begin developing negatively. The area with the most opaque color depicts the day of the tornado (top). Geopotential height [gpdam] at 300 hPa (isohypses) and geopotential height [gpdam] difference between 500hPa and 1000hPa (shaded color contours) (middle). Near-surface (925 hPa) horizontal frontogenesis function [K/100km/3h] (bottom).

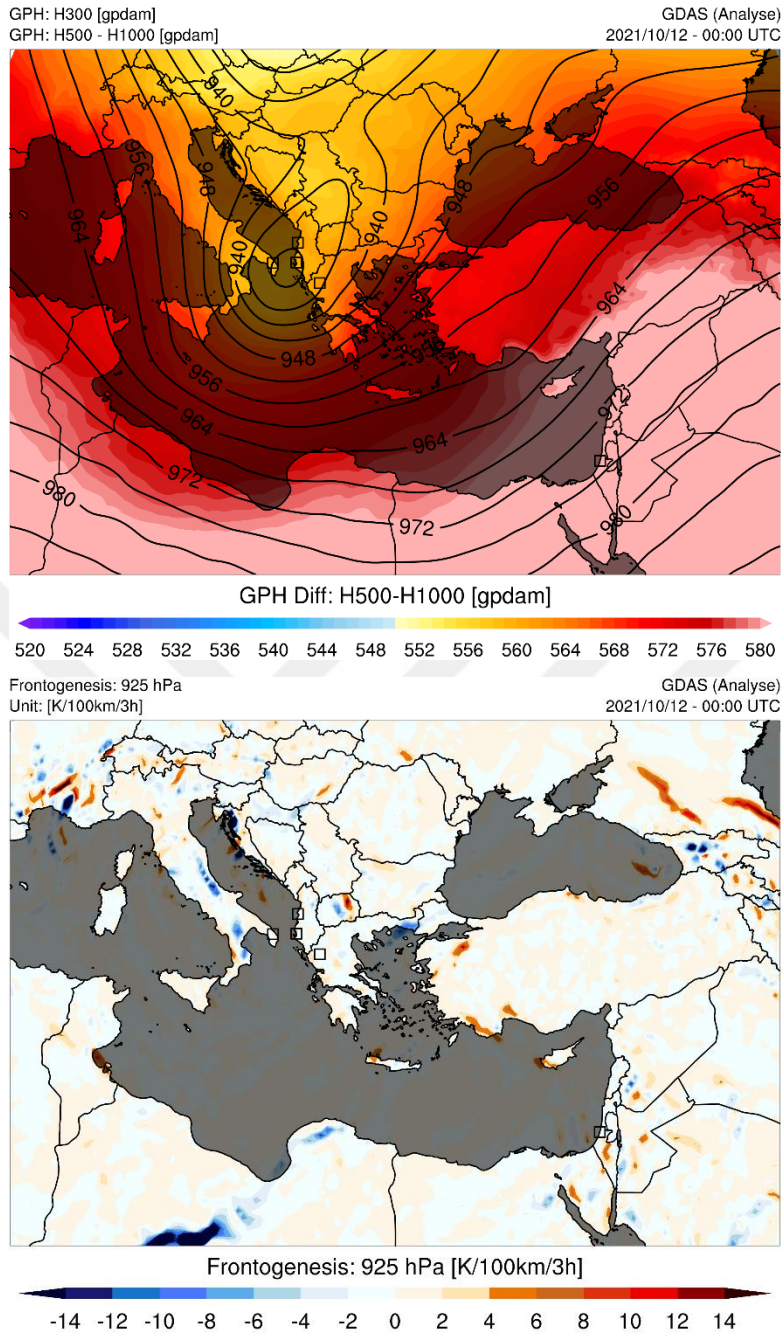


Figure 3.14 (continued): 10-days all EMEDO member oscillations (the vertical axis) surrounding tornado incidents in daily period (the horizontal axis) (12.10.2021). The lightest shaded areas indicate 1 to 3 days before the tornado event of EMEDO_i members, whereas the darkest shaded parts indicate the days when EMEDO_i members begin developing negatively. The area with the most opaque color depicts the day of the tornado (top). Geopotential height [gpdam] at 300 hPa (isohypses) and geopotential height [gpdam] difference between 500hPa and 1000hPa (shaded color contours) (middle). Near-surface (925 hPa) horizontal frontogenesis function [K/100km/3h] (bottom).

The movement of the cold front towards the northeast resulted in it being occluded over the North Aegean (Fig 3.15). The temperature gradient at the jet level is quite high between the poles of the index. This mechanism led to gusts of jet gusts. The EMEDO-Oper index value went from -5 to neutral phase in approximately 36 hours. It remained below -4 for more than 12 hours. With the expansion of the upper level blockage, the tornado incident occurred.

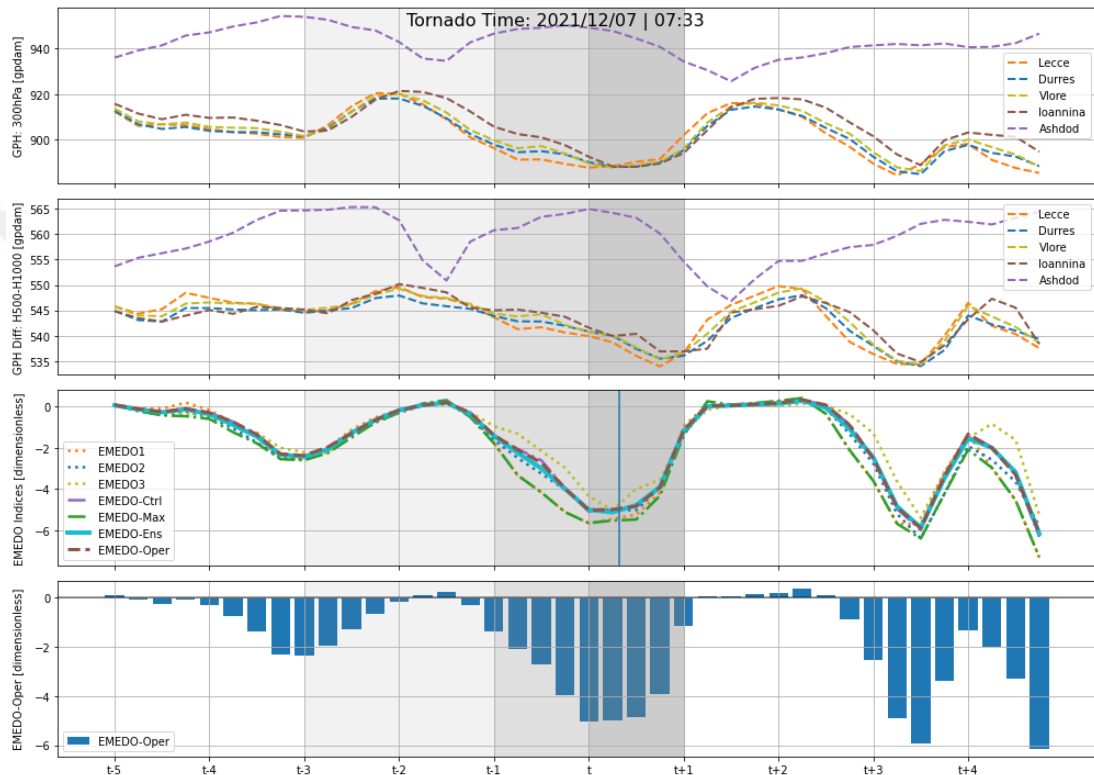
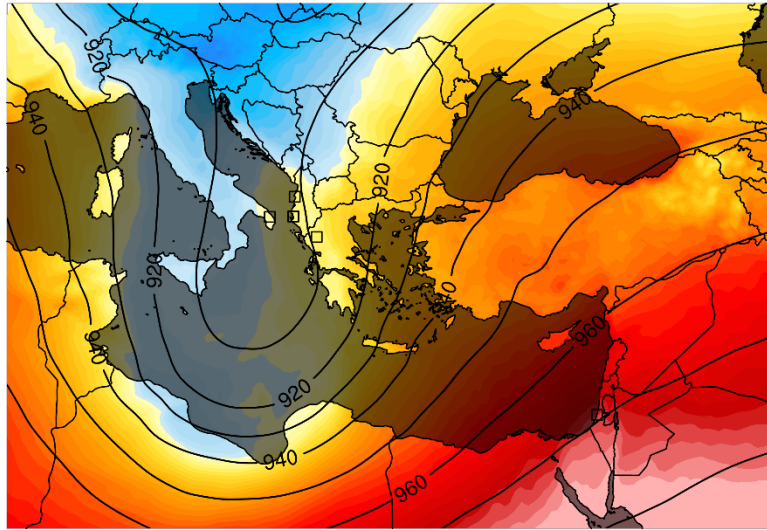


Figure 3.15 : 10-days all EMEDO member oscillations (the vertical axis) surrounding tornado incidents in daily period (the horizontal axis) (07.12.2021). The lightest shaded areas indicate 1 to 3 days before the tornado event of EMEDO_i members, whereas the darkest shaded parts indicate the days when EMEDO_i members begin developing negatively. The area with the most opaque color depicts the day of the tornado (top). Geopotential height [gpdam] at 300 hPa (isohypses) and geopotential height [gpdam] difference between 500hPa and 1000hPa (shaded color contours) (middle). Near-surface (925 hPa) horizontal frontogenesis function [K/100km/3h] (bottom).

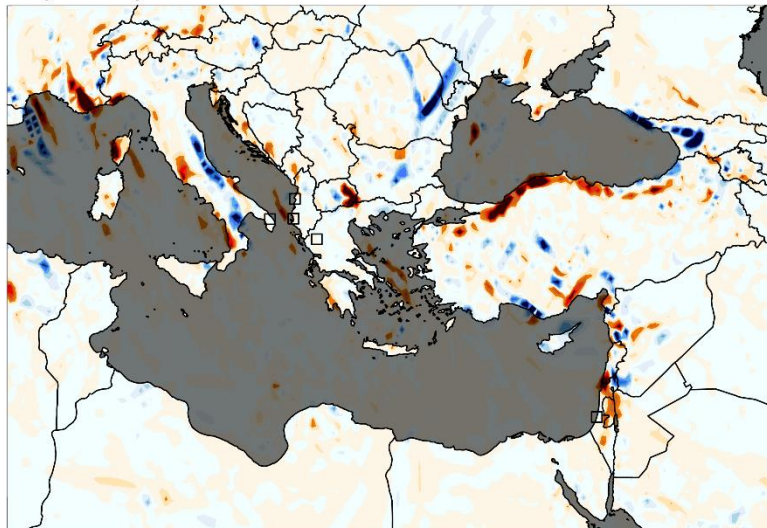
GPH: H300 [gpdam] GDAS (Analyse)
 GPH: H500 - H1000 [gpdam] 2021/12/07 - 00:00 UTC



GPH Diff: H500-H1000 [gpdam]

520 524 528 532 536 540 544 548 552 556 560 564 568 572 576 580

Frontogenesis: 925 hPa GDAS (Analyse)
 Unit: [K/100km/3h] 2021/12/07 - 00:00 UTC



Frontogenesis: 925 hPa [K/100km/3h]

-14 -12 -10 -8 -6 -4 -2 0 2 4 6 8 10 12 14

Figure 3.15 (continued): 10-days all EMEDO member oscillations (the vertical axis) surrounding tornado incidents in daily period (the horizontal axis) (07.12.2021). The lightest shaded areas indicate 1 to 3 days before the tornado event of EMEDO_i members, whereas the darkest shaded parts indicate the days when EMEDO_i members begin developing negatively. The area with the most opaque color depicts the day of the tornado (top). Geopotential height [gpdam] at 300 hPa (isohypsals) and geopotential height [gpdam] difference between 500hPa and 1000hPa (shaded color contours) (middle). Near-surface (925 hPa) horizontal frontogenesis function [K/100km/3h] (bottom).

The cold front was able to extend its area of effect to include the North African region thanks to the ULL system, which maintains the cold air and moves on an axis that passes southwest to northeast (Fig 3.16). On the day before the storm, EMEDO indices of this particular system's are all in the negative phase, and the tornado storm occurred after the EMEDO-Oper index shifted into the neutral phase.

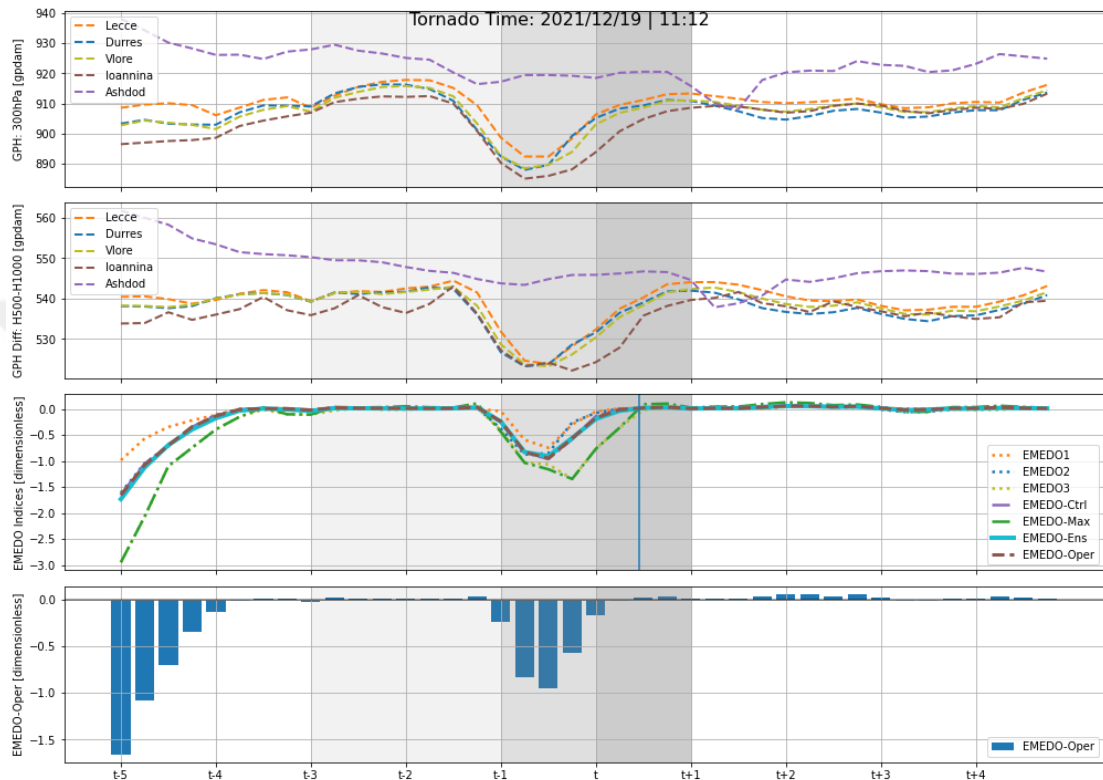


Figure 3.16 : 10-days all EMEDO member oscillations (the vertical axis) surrounding tornado incidents in daily period (the horizontal axis) (19.12.2021). The lightest shaded areas indicate 1 to 3 days before the tornado event of EMEDOi members, whereas the darkest shaded parts indicate the days when EMEDOi members begin developing negatively. The area with the most opaque color depicts the day of the tornado (top). Geopotential height [gpdam] at 300 hPa (isohypses) and geopotential height [gpdam] difference between 500hPa and 1000hPa (shaded color contours) (middle). Near-surface (925 hPa) horizontal frontogenesis function [K/100km/3h] (bottom).

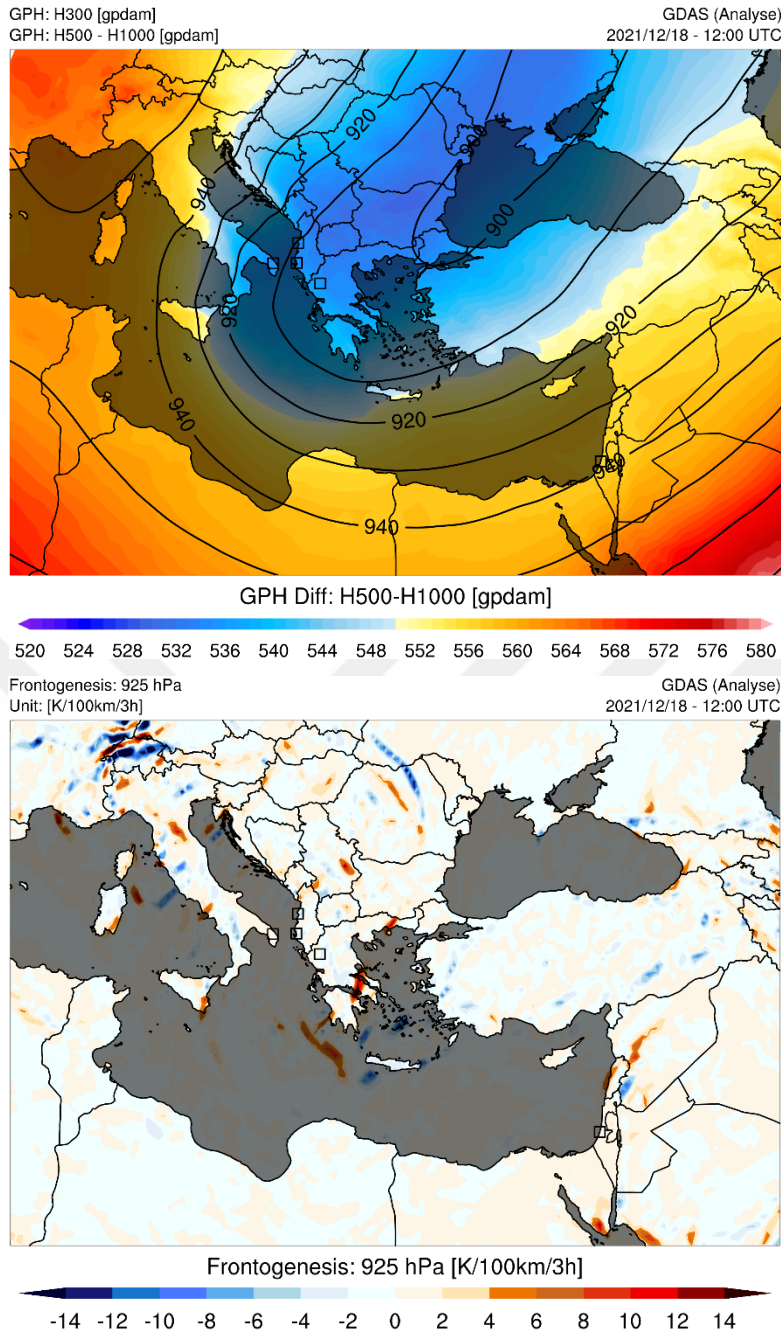


Figure 3.16 (continued): 10-days all EMEDO member oscillations (the vertical axis) surrounding tornado incidents in daily period (the horizontal axis) (19.12.2021). The lightest shaded areas indicate 1 to 3 days before the tornado event of EMEDO_i members, whereas the darkest shaded parts indicate the days when EMEDO_i members begin developing negatively. The area with the most opaque color depicts the day of the tornado (top). Geopotential height [gpdam] at 300 hPa (isohypses) and geopotential height [gpdam] difference between 500hPa and 1000hPa (shaded color contours) (middle). Near-surface (925 hPa) horizontal frontogenesis function [K/100km/3h] (bottom).

There have been observations made of patterns that may be understood to be shared by all EMEDO_i members. Before tornadoes occur, the oscillation pattern and

circulation of EMEDO are responsible for explaining many of the meteorological characteristics. The geopotential heights that were observed during each incident were distinct from one another because to the pressure drop, the enhanced instability brought on by the presence of seawater, and the depth at which the ULL struck Turkiye. This is the essential piece of information necessary to deduce how upper-tropospheric jet streams sweep.

The pattern that is frequently observed in all occurrences, with the exception of the one that occurred on March 03, 2016, is that: At the time of the tornado events, the majority of EMEDO_i members (particularly EMEDO-Oper) are predominantly in negative phase. Because of the triangle and center point that were created at the western pole point, cyclones always pass through the Eastern Mediterranean basin on their way to the east. Because of this, they always cause a decrease in thickness near the ground and a decrease in geopotential height in the upper troposphere. The reason for this can be explained by the fact that the triangle and center point were created at the western pole point.

At the time of the tornado, the EMEDO-Oper value was typically in a negative phase. This is applicable to the majority of the selected tornado incidents. At the time of the tornado occurrence, the values of this member can only possibly qualify as being in a neutral phase in two plots that make up a relatively insignificant portion of the train cluster. The greater the negative EMEDO phase, the deeper the geopotential gradient between the trough over Italy, Greece and Albania and the ridge in the vicinity of Israel; as a result, the environmental conditions in the Eastern Mediterranean are more favorable for the formation of a frontogenesis. In addition, the strength of fronts was typically characterized as being in the strong classification, which is described as having more than 8K per 110km of gradients. There have been a few instances of events that have been reported as waterspouts, and in those instances, the strength of the fronts has been classified as moderate (4K/110km).

The hourly period until the local minimum is obtained can be described and characterized as the process by which the EMEDO-Oper index value decreases continuously. Therefore, the procedure for achieving the local minimum varies between events. This period is calculated to be an average of 31.3 hours based on the tornado occurrences in the train cluster, and 33.2 hours when the 2022 tornado occurrences are included.

This procedure varies based on the velocity of the incoming trough, which transports cold air from the high latitudes to the Mediterranean. Systems located in the Central Mediterranean linger in the Italy-Greece-Albania triangle, sometimes due to Omega blockade and other times because to cyclonic cut-off obstructions emanating from the dipole. Such instances demonstrate how long the ULL, which is a component of the EMEDO-Oper index, lingers in the region of western pole of EMEDO_i, and how the eastern pole over Israel contribute to the increase in values caused by the presence of high pressure and ridge effect. Thus, EMEDO-Oper values might remain in the negative phase for an extended period of time and grow stronger.

In addition, a culminating point may occur at the local minimum point of the negative phase prior to or around the hours of the tornado occurrences, including non-mesocyclonic waterspouts suctioning from warm sea surfaces to relatively cold air at upper level troposphere. This can take place regardless of the movement of the frontal boundary. There is no set schedule for when a tornado will strike; it might happen at any time. The next portion ought to concentrate on the 72 hours that were immediately before the events, with the tornado occurrences serving as the focal point of the investigation. This will allow for a more in-depth analysis in terms of temporal during these 72-h (for instance, t-24 represents 24-h before the storm time).

3.3 Analysis of Statistics

Examining the variations of the numbers 1, 2, and 3 of EMEDO_i reveals that the number of extreme values and values that can be regarded outliers is smaller than the variations of Control, Ensemble, Operational, and Maximum. When all variances are taken into account, the average values measured roughly -3 and achieved a local minimum 12 hours before to the tornado events. The median values, on the other hand, maintained the same overall oscillation and decreased below the value of -2.

Although the box plot lengthens again 12 hours after the tornado, this is due only to the synoptic ULL-induced system lingering over the eastern Mediterranean and reducing the thickness by generating a reaction low-pressure system over the Mediterranean (Fig 3.17). This is because as the cold outbreak goes to such southern latitudes, it transforms into the Cyprus Low or the Black Sea Low with cyclonic movement, especially by the water, which remains relatively warm during the winter (Fig. 1.34).

After the tornado has occurred and lost its effect, the effect of the EMEDO index values in the negative phase declines at the same rate and approaches neutral. The value of the EMEDO index just prior to the tornado tends to range anywhere from -1 to -4 on average. In addition, while all events oscillate similarly without outliers until 12 hours prior to the tornado occurrence, the index values for all events demonstrate significant variations as the tornado time approaches. This oscillation has the same pattern for all EMEDO variations. This can demonstrate whether negative EMEDO readings can generate a tornado forecast. The EMEDO Operational index will be employed in the following round of study.

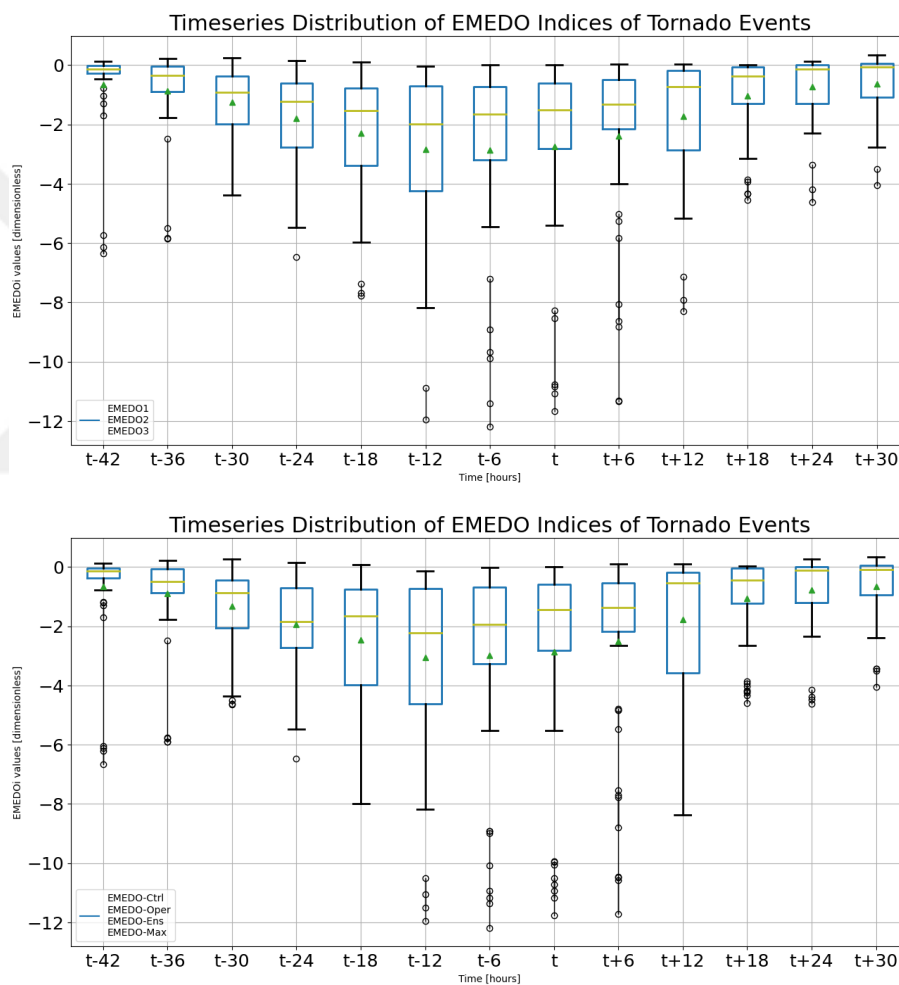


Figure 3.17 : The all EMEDO indices (the vertical axis) in the Whisker-Box plots represent the time period interval (the horizontal axis) of 42 hours before to 30 hours after tornado events initiated. In addition, the EMEDO values at the moment of the tornado are also shown specifically to reveal statistical connection between the events. The boxes extend to the 25th and 75th percentiles, while the whiskers to the 10th and 90th percentiles. Median values are shown as horizontal line within the boxes and mean values are demonstrated as triangle within the boxes.

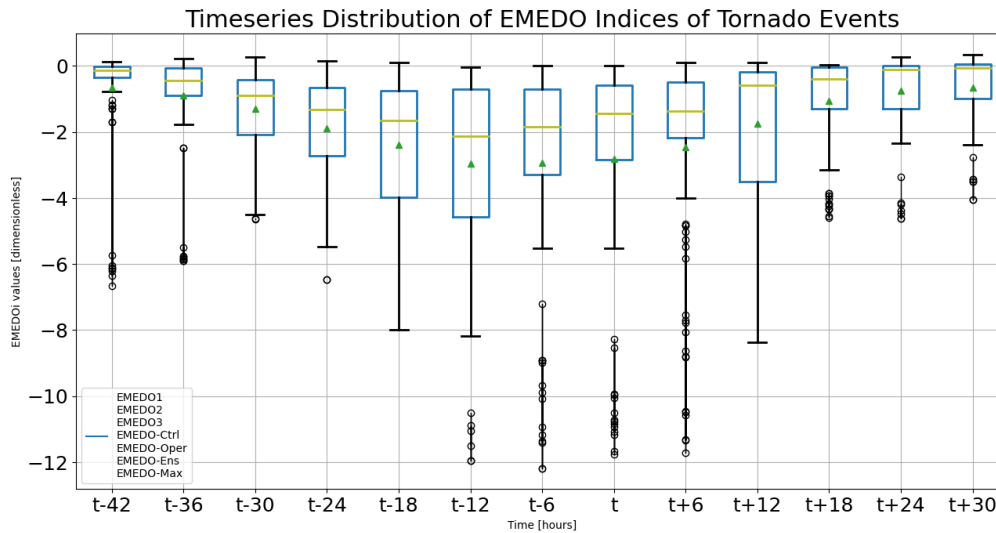


Figure 3.17 (continued): The all EMEDO indices (the vertical axis) in the Whisker-Box plots represent the time period interval (the horizontal axis) of 42 hours before to 30 hours after tornado events initiated. In addition, the EMEDO values at the moment of the tornado are also shown specifically to reveal statistical connection between the events. The boxes extend to the 25th and 75th percentiles, while the whiskers to the 10th and 90th percentiles. Median values are shown as horizontal line within the boxes and mean values are demonstrated as triangle within the boxes.

Table 3.1 refers to the fact that the lowest average EMEDO index value was -2,947 twelve hours before to the tornado. This score indicates the strength of the negative EMEDO_i phase based on whisker plots, where it is a highly remarkable mean. As the tornado moment approaches, the standard deviation numbers grow. This might be taken as the fact that different systems have varying strengths at the index measurement locations; hence, the numbers in the extreme values are excessive.

The minimum value of the EMEDO index is only occasionally lower than -10. These values for the EMEDO index are quite low and are rarely measured. Prior to the occurrence of tornadoes, the minimum values and Pythagorean averages reached the local minimum. In the time series of the 25th, 50th, and 75th quantile values, it is evident that the tendency of EMEDO drops as the tornado moment approaches and returns to neutral phase following the tornado occurrence. As expected, the highest values are close to 0 because the neutral phase is the period during which the tornado risk is not predicted.

Table 3.1 : Performance statistics of tendency metrics for the differences of EMEDO indices in Turkiye during the period of tornadic storm event.

| Time | t-42 | t-36 | t-30 | t-24 | t-18 | t-12 | t-6 | t | t+6 | t+12 | t+18 | t+24 | t+30 |
|----------------------------|-------|-------|-------|-------|-------|--------|--------|--------|--------|-------|-------|-------|-------|
| Mean | -0.61 | -0.83 | -1.19 | -1.78 | -2.27 | -2.95 | -2.85 | -2.75 | -2.41 | -1.68 | -1.01 | -0.74 | -0.62 |
| Geometric mean | -0.13 | -0.32 | -0.60 | -0.99 | -1.38 | -1.65 | -1.30 | -1.18 | -1.02 | -0.48 | -0.18 | -0.15 | -0.20 |
| Harmonic mean | -0.05 | -0.10 | -0.14 | -0.18 | -0.60 | -0.84 | -0.16 | -0.18 | -0.22 | -0.11 | -0.01 | -0.03 | -0.06 |
| Standard Deviation | 1.56 | 1.50 | 1.22 | 1.42 | 2.04 | 3.12 | 3.35 | 3.45 | 3.12 | 2.33 | 1.42 | 1.24 | 1.10 |
| Min | -6.04 | -5.80 | -4.50 | -4.70 | -5.98 | -11.04 | -11.17 | -10.73 | -10.47 | -7.76 | -4.17 | -4.38 | -3.44 |
| Quantiles 25 | -0.30 | -0.70 | -1.91 | -2.64 | -3.72 | -4.20 | -3.02 | -2.63 | -2.10 | -2.97 | -1.15 | -1.08 | -0.82 |
| Quantiles 50 Median | -0.07 | -0.49 | -0.81 | -1.63 | -1.36 | -2.14 | -1.75 | -1.42 | -1.37 | -0.51 | -0.38 | -0.10 | -0.08 |
| Quantiles 75 | -0.01 | -0.08 | -0.46 | -0.73 | -0.72 | -0.61 | -0.67 | -0.69 | -0.45 | -0.14 | -0.05 | 0.01 | 0.05 |
| Max | 0.05 | 0.15 | 0.12 | 0.02 | 0.08 | -0.17 | -0.01 | 0.02 | 0.02 | 0.04 | 0.01 | 0.06 | 0.25 |

The error values exhibit a pattern that is consistent between t-30 and t-12, however mean=-0.75 is the value that provides the highest level of accuracy due to the fact that it has the lowest error rates for the entirety of the episode (Fig 3.18).

According to descriptive data and box-whisker plots, the average EMEDO index value has attained its local minimum between -0.75 and -3. The MSE and MAE graphs of this index range with 0.25 intervals are as follows in order to establish the reference threshold value. As demonstrated, the error tendency from t-42 to t-30 for reference threshold values is extremely large. The MAE error distribution values range from 0.75 to 2.75. However, particularly between t-30 and t-12, that is, in the section with a shaded backdrop, which is the appropriate period for the local minimum and whichever index value is used, the margins of error are quite tight. During this time frame, error rates reach their lowest point, acting like a braid of hair. During this interval, the MAE values do not surpass the threshold of 2, indicating that a tornado is approaching. In addition, error values around the time of tornado events are high for MSE values, while the error values reached their minimum value 30 and 12 hours before the tornado.

When the tornado event begins and the system loses its influence, the error tendency tends to revert to its distribution during the initial time, and error levels rise. The most important finding here is that all lines attain their lowest error levels prior to the tornado, regardless of the threshold values on which the error depends, during the 18-hour period indicated by the shaded region. Consequently, the interval between t-30 and t-12 is crucial for the investigation, and the threshold value as -0.75 will continue to be evaluated because it has the lowest error statistics for predicting the conditions for the occurrence of a tornado event.

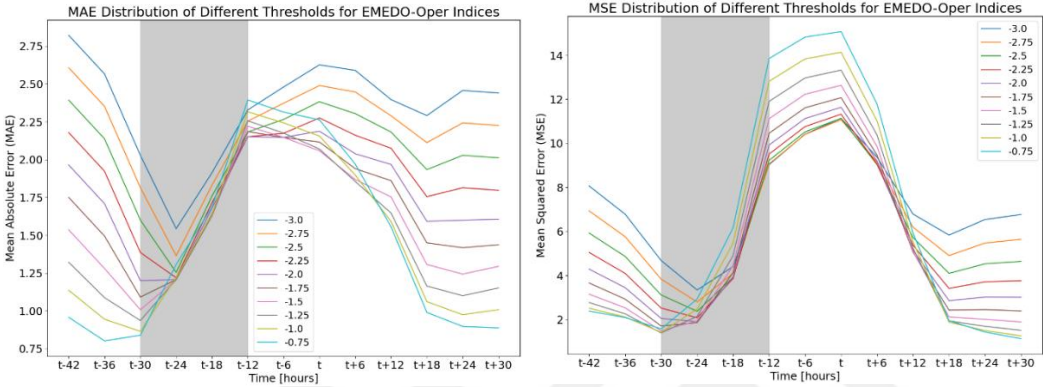


Figure 3.18 : Error distributions between the EMEDO-Oper indice values (the vertical axis) of -0.75 and -3.0 for time period (the horizontal axis) of 42 hours before to 30 hours after for selected tornado events. Mean Absolute Error (left) and Mean Square Error (right).

As shown in Table 3.2., for each error distribution of the EMEDO-Oper value, a variety of conclusions can be drawn. Although the MAE value was lower than 1 during the specific time period that occurred 42 hours before the onset of the tornado, it rises to a value of 2 as the tornado draws closer, and then it subsequently drops back down to a lower value after the tornado has passed. Due to the negative EMEDO-Oper index, MBE values are calculated as negative during the times around a tornado's moment. It approaches the 0-limit value 36 hours before the tornado and after considerable time. Twelve hours before the tornado, MPE values approached the neutral phase with a value of about 0.1, which can be viewed extraordinarily favorably. As shown in the chart above (Fig 3.18), the MSE values were at their lowest between 36 and 12 hours prior to tornado occurrences, however they are exceedingly considerable between t-18 and t+12.

During the t-18 to t-12 time frame, the Mean Absolute Percentage Error (MAPE) achieved its minimum values before decreasing to roughly 1%. During and after the

tornado event, it continued to surge excessively. The error values for Root Mean Square Error (RMSE) are at a minimum until t-18, a considerable time after the tornado occurrence. Here, the time span t-18 - t+12 is the interval in which the margin of error is the greatest. Root Mean Square Logarithmic Error (RMSLE) has similar tendencies to RMSE.

Table 3.2 : Performance statistics of accuracy metrics according to the EMEDO-Oper=-0.75 during the period of tornadic storm (including local minimum time & tornado time) for all events in Turkiye. Values indicate Mean Bias Error (MBE), Mean Absolute Error (MAE), Mean Squared Error (MSE), Root Mean Square Error (RMSE), Root Mean Square Logarithmic Error (RMSLE), Mean Percentage Error (MPE), and Mean Absolute Percentage Error (MAPE), which are statistically significant positive correlations at 95% confidence level.

| | t-42 | t-36 | t-30 | t-24 | t-18 | t-12 | t-6 | t | t+6 | t+12 | t+18 | t+24 | t+30 |
|--------------|-------|-------|-------|-------|-------|-------|-------|-------|-------|-------|-------|-------|-------|
| MAE | 0.96 | 0.8 | 0.84 | 1.31 | 1.69 | 2.39 | 2.31 | 2.26 | 1.97 | 1.56 | 0.99 | 0.9 | 0.89 |
| MBE | 0.14 | -0.08 | -0.44 | -1.03 | -1.52 | -2.2 | -2.1 | -2 | -1.66 | -0.93 | -0.26 | 0.01 | 0.13 |
| MPE | 6.61 | -3.66 | 3.05 | 3.37 | 1.14 | 0.1 | -3.66 | 3.72 | 2.6 | 0.58 | -6.28 | 20.8 | 8.96 |
| MSE | 2.38 | 2.09 | 1.58 | 2.93 | 6.17 | 13.85 | 14.82 | 15.08 | 11.79 | 5.92 | 1.95 | 1.43 | 1.14 |
| MAPE | 14.21 | 7.24 | 5.22 | 4.1 | 1.22 | 0.85 | 4.57 | 4.25 | 3.41 | 6.98 | 65.95 | 22.84 | 12.31 |
| RMSE | 1.54 | 1.45 | 1.26 | 1.71 | 2.48 | 3.72 | 3.85 | 3.88 | 3.43 | 2.43 | 1.4 | 1.2 | 1.07 |
| RMSLE | -0.57 | -0.49 | -0.48 | -0.62 | -0.74 | -0.89 | -0.88 | -0.86 | -0.8 | -0.72 | -0.56 | -0.53 | -0.5 |

By averaging the correlations between 14 tornado occurrences for the t-42 - t-6 and t-30 - t-12 time frames, it is aimed to evaluate whether the EMEDO Operational Index is meaningful for all events within the determined local minimum occurrence period. As shown in Table 3.3., the success rate in the correlation values for the Spearman variation is evidently between 0.80 and 1 and is calculated as a very significant connection with a high correlation, whereas the Pearson variation typically ranges between 0.60 and 0.80 and can be explained as a strong correlation association. Based on Pearson correlation, the period t-30 to t-12 exhibited a high correlation, and based on Spearman correlation, the period t-42 to t-6 likewise exhibited a high correlation. Each correlation technique takes a distinct approach to raw data, which is one of the reasons why the scores vary. To clarify, Pearson correlation is a useful metric for normally distributed random variables and linear relationship. However, Spearman

rank correlation often describes the skewed link and monotonic connection between datasets. Therefore, while there is a monotonic relationship over a broad span of time, t-30 - t-12 represents a linear relationship.

Another objective is to determine if each occurrence provides the right environmental conditions for the creation of tornadic storms in the boundary layer and upper-level troposphere. As seen in Fig. 1.35, it generally interacts with the sea in the Eastern Mediterranean atmosphere and modifies the trough's synoptic characteristics, despite the fact that the majority of ULL systems influence Turkiye in distinct ways. In this manner, it can have a significant impact on coastal provinces in different time zones and months, particularly during the winter.

Table 3.3 : Correlation statistics of cumulative minimum of EMEDO-Oper indices during the period of tornadic storm (including local minimum time & tornado time) for all events in Turkiye. Values indicate Correlation coefficient (CC), Coefficient of Determination (CD), adjusted version of Coefficient of Determination (CD_{adj}), which are statistically significant positive correlations at 95% confidence level.

| Time | CC | | CD | | CD _{adj} | |
|-------------|---------|----------|---------|----------|-------------------|----------|
| | Pearson | Spearman | Pearson | Spearman | Pearson | Spearman |
| t-30 – t-12 | 0.83 | 0.91 | 0.69 | 0.82 | 0.66 | 0.81 |
| t-42 – t-6 | 0.86 | 0.95 | 0.75 | 0.89 | 0.73 | 0.89 |

3.4 Verification

In this process, an investigation into that severe weather analysis will be carried out employing only EMEDO-Oper for the purposes of operation. Because of this, the five tornadoes that occurred along the western coast of Turkiye in 2022 are detailed in the following sections.

After statistically validating the EMEDO index, five genuine instances from 2022 were chosen to evaluate the index's performance. The 14 tornado incidents that occurred in Turkiye over the course of the previous six years were evaluated meteorologically and statistically in order to provide insight into the EMEDO Index's application. If a local minimum happens, the two distinct time spans "t-42 to t-6" and "t-30 to t-12" in highly correlated events must indicate the probable occurrence period of the tornado.

In the tornado event of January 9, the EMEDO-Oper value declined to -0.6 around 12 hours and 20 minutes before the tornado occurred, with other EMEDO variants exhibiting a similar trend. However, after the occurrence, the variations continued to oscillate in a highly distributed and irregular manner. In the March 2 tornado incident, all EMEDO variations were distributed in a balanced manner. The exception in this case is that it took a considerable amount of time for the local minimum value to be reached, that is, to surpass the value of -7, and the index remained in the negative phase for a substantial amount of time until it reached the turning point. During this phase of negative growth, the EMEDO-Max variation and the EMEDO-3 variation followed distinct patterns. On April 19th, notably harmonious patterns appeared during the tornado. This is due to the fact that the ULL crosses directly above the EMEDO_i west polar region. A negative EMEDO phase was detected, which was significant in comparison to other occurrences. The EMEDO value of the 15 October case is remarkably low, but its development is extremely abrupt. The time required to move from the positive phase to the negative phase and attain the local minimum value is only 12 hours. A second tornado was detected 12 hours after the minimum for the region. EMEDO-Max and EMEDO-3 split themselves from other members and followed the same path. According to the plot on November 7, the tornado that hit roughly 27 hours after the local minimum happened in a condition where the EMEDO-Oper member was negative yet weak. Before all members reached the local minimum, there was a minor upward fluctuation in the EMEDO-2 member and a downward fluctuation in the EMEDO-Max member, but the EMEDO-Oper variation steadily collected strength in the negative phase for about 24 hours and reached the local minimum mode. However, after the occurrence, the EMEDO-Oper variation remained in a slightly positive phase.

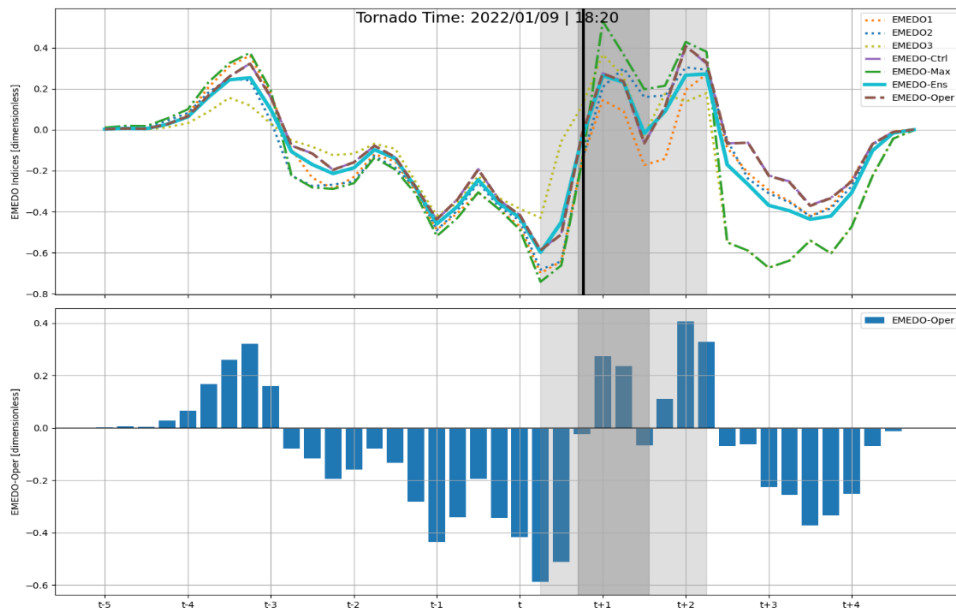


Figure 3.19 : During the 72 hours preceding the tornado (the horizontal axis), all versions of EMEDO_i (top) and EMEDO-Oper (bottom) were analysed for 09.01.2022 event (the vertical axis). The lightly colored regions reflect the sixth to forty-second hours following the local minimum peak of the EMEDO-Oper index. The opaque inner regions indicate the 12th to 30th hours following the local minimum peak of the same index. The vertical black line depicts the instant the tornado occurred.

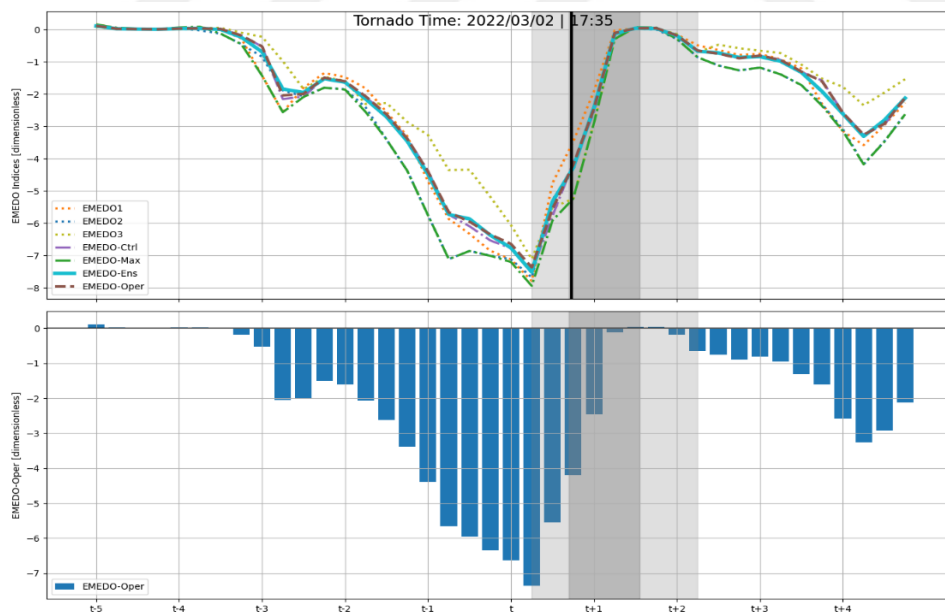


Figure 3.20 : During the 72 hours preceding the tornado (the horizontal axis), all versions of EMEDO_i (top) and EMEDO-Oper (bottom) were analysed for 02.03.2022 event (the vertical axis). The lightly colored regions reflect the sixth to forty-second hours following the local minimum peak of the EMEDO-Oper index. The opaque inner regions indicate the 12th to 30th hours following the local minimum peak of the same index. The vertical black line depicts the instant the tornado occurred.

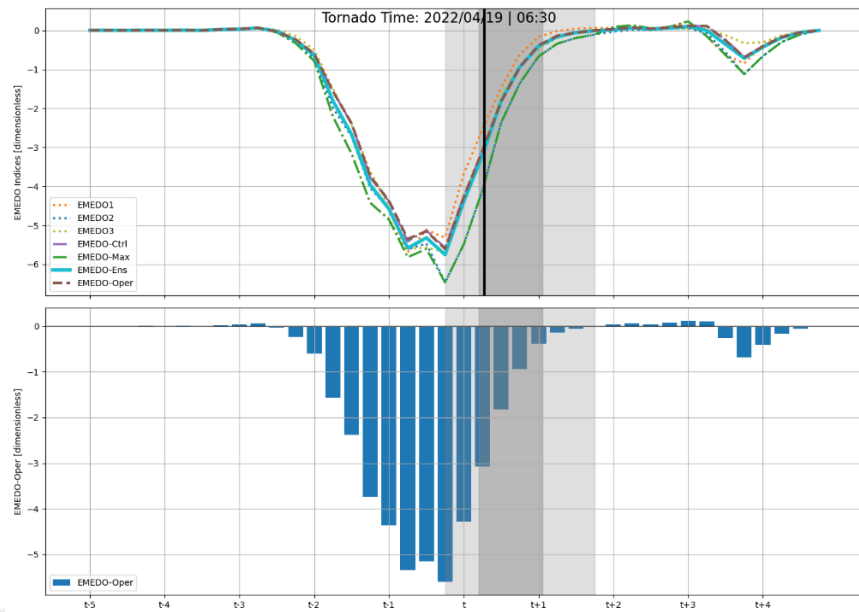


Figure 3.21 : During the 72 hours preceding the tornado (the horizontal axis), all versions of EMEDO_i (top) and EMEDO-Oper (bottom) were analysed for 19.04.2022 event (the vertical axis). The lightly colored regions reflect the sixth to forty-second hours following the local minimum peak of the EMEDO-Oper index. The opaque inner regions indicate the 12th to 30th hours following the local minimum peak of the same index. The vertical black line depicts the instant the tornado occurred.

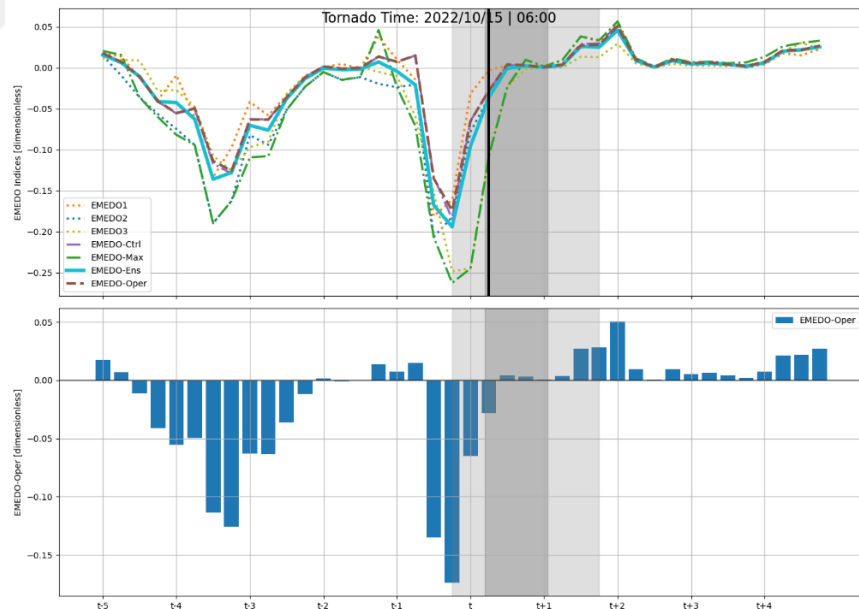


Figure 3.22 : During the 72 hours preceding the tornado (the horizontal axis), all versions of EMEDO_i (top) and EMEDO-Oper (bottom) were analysed for 15.10.2022 event (the vertical axis). The lightly colored regions reflect the sixth to forty-second hours following the local minimum peak of the EMEDO-Oper index. The opaque inner regions indicate the 12th to 30th hours following the local minimum peak of the same index. The vertical black line depicts the instant the tornado occurred.

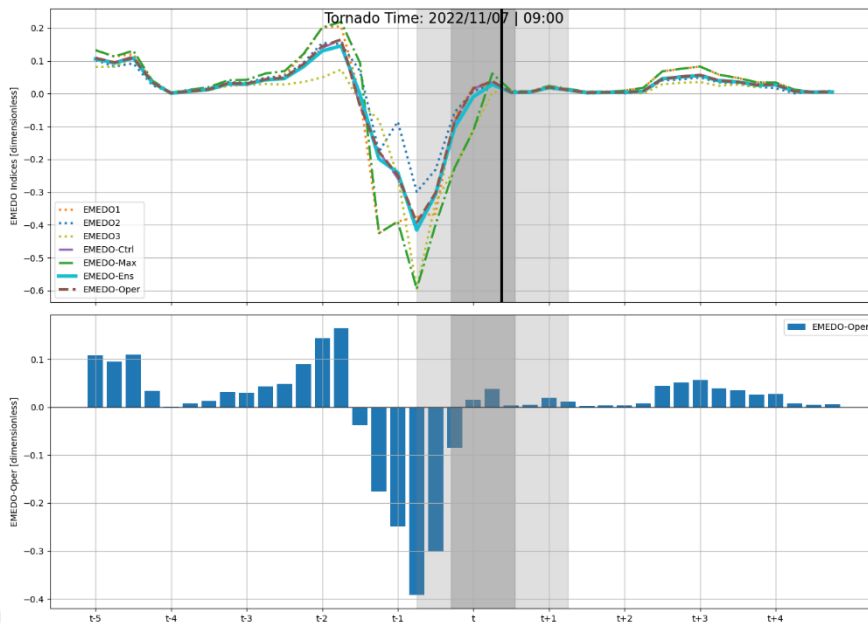


Figure 3.23 : During the 72 hours preceding the tornado (the horizontal axis), all versions of EMEDO_i (top) and EMEDO-Oper (bottom) were analysed for 07.11.2022 event (the vertical axis). The lightly colored regions reflect the sixth to forty-second hours following the local minimum peak of the EMEDO-Oper index. The opaque inner regions indicate the 12th to 30th hours following the local minimum peak of the same index. The vertical black line depicts the instant the tornado occurred.

Prior to the tornado, it was noticed that the EMEDO index values had a falling trend in all events, as predicted, but after the tornado it rebounded to a neutral phase. Based on a prediction to be made at the local minimum, the formation of the tornado is predicted to occur within the following 6 to 42 hours, or as it approaches the neutral phase. Also, as previously discussed, although the -0.75 threshold value is statistically reliable with a minimum margin of error, it is not reliable for newly-occurring case scenarios.

In light of this information, it appears that forecasts of tornado occurrence time intervals based on the EMEDO index would be consistent for all events when evaluated in terms of the relationship between a declining and an increasing trend, regardless of the magnitude of index value.

4. CONCLUSION

Numerous oscillation indices are created and used with the goal of analyzing standardized variations in atmospheric pressure. While the other oscillation indices in the Mediterranean Basin, MOi and WeMOi etc., served as inspiration, the EMEDO_i focuses on the early forecast of tornadic storms in Turkiye and contains more vertical thickness information through the vertical layer.

Apart from these, numerous composite parameters that incorporate measures of tornadoes have been developed, such as STP, SCP, Significant Hail Parameter (SHIP), and so forth. However, these are useful to identify tornadic storm environments for a specific location based on probabilistic forecasts, which are currently utilized by national weather services and private companies. The fact that high sea water temperature anomalies around Mediterranean increase the number of tornadoes and waterspouts in non-mesocyclonic structure indicates that formulas such as STP and SCP cannot perpetually be pioneer guides. Understanding and progressing mesoscale model studies becomes important at this point in order to predict tornado formation and dynamical concepts. Due to this reason, high-resolution modeling is a must a few days in advance for mesocyclonic supercell thunderstorms capable of producing F2+ tornadoes. Unfortunately, to predict where and when tornadoes may occur, the computational costs of constantly operating high-resolution numerical weather prediction models are hard to afford financially, even for these institutes. Moreover, if the spatial and temporal resolution of the modeling is insufficient, these composite parameters make it unlikely where the tornado will occur.

The formation of a front on the Eastern Mediterranean is crucial for these devastating tornadic storms and the sweep mechanism in upper-level towards Turkiye by this front should support the environmental conditions of these storms. This is because for occurring a tornadic storm activity, there is a contribution of sweeping mechanism at jet-streak level in order to allow updraft air to move upward as a necessity of conservation of air mass law in the atmosphere (Equation of Continuity). High level jet streaks can be identified thanks to isobaric temperatures and isobaric geopotential

height levels. To reduce the impacts of severe convective storms and tornadoes in the scope of climate change adaptation strategies, Eastern Mediterranean Oscillation Index (EMEDO_i) has been developed in order to be able to detect the presence of ULLs and frontogenesis approach is employed for selected tornadic storm events in Türkiye. EMEDO_i has 7 different its variations (members). These members have been developed to detect differences depending on the entry directions of cyclones and storms affecting Türkiye from the west of the country. In line with the GDAS data analysis, values of geopotential height are derived for the requirements of EMEDO_i in a limited area.

As can be seen, SCS activities increase in Türkiye during the first few days of sudden ascents from the negative phase to the neutral phase. It is not obviously seems that the stronger the tendency due to the change of this phase, the greater the damage of the storms. Accordingly, the formation of a front in the Eastern Mediterranean is crucial, and the sweep mechanisms of Türkiye by this front support the environmental conditions of these storms. Just before the imminent occurrence of the tornado events, it is revealed that geopotential thickness difference values decrease at P1-3 and C points covering Italy, Greece, and Albania. At the same time, across the poles, the difference between isohypse values increases due to the high temperature gradient of 300 hPa.

As the spread of all members of EMEDO_i expanded with forecast time, it took on different values than EMEDO-Ens or EMEDO-Oper, making it more difficult to explain the consequences of modifying or determining nonmesocyclonic waterspouts and mesocyclonic supercell tornado structures. Consequently, it may also be claimed that the amplitude of the EMEDO perturbations may have been either small or too large for a severe weather warning, and that the EMEDO spatial variability (noisy patterns) may have diminished the signal.

The key results of the study are as follows:

- 86% of the events in the train list demonstrated that the EMEDO-Oper index was in negative phase at the time a tornado was reported, regardless of whether the events involved by a supercell mesoscale convective storm or a frontal movement. At the time of the tornado, the values of consisting of a small portion of the train cluster can only qualify as neutral phase. However, a

turning point may take place at the local lowest point of the negative phase just before or around the hours that tornado events happen. This includes non-mesocyclonic waterspouts that are induced by the sea.

- Each tornado incident in the western region of Turkiye occurred at a different time of day, but the daytime is more favourable.
- The greater the negative EMEDO phase, the deeper the geopotential gradient between the trough over Italy, Greece and Albania and the ridge in the vicinity of Isreal; as a result, the environmental conditions in the Eastern Mediterranean are more favorable for the formation of a frontogenesis. Besides, the strength of fronts were generally observed as strong classification which is defined as more than 8K per 110km. In a few cases of events which are reported as waterspout, the strength of the fronts can be considered moderate classification (4K/110km).
- The amount of time needed to reach the local minimum perpetually varies depending on the event. This timescale is estimated to be 31.3 hours on average based on the tornadic storm environment in the train cluster; however, when the tornado activity in 2022 is taken into account, this time frame is estimated to be 33.2 hours instead.
- Between 6 hours and 42 hours after the EMEDO-Oper index reaches its local minimum, a tornado can be expected with a 79% probability in western Turkiye. More specifically, the probability for this period is predicted to be 63% between 12 hours and 30 hours after the local minimum has been determined. Once the local minimum has been reached, the remaining events typically occur within the next couple of hours.
- Based on the EMEDO-Oper values of the analyzed events, the majority of the events had index values below -0.75. It is therefore possible to expect a risky period in Turkiye with a 79% probability after an EMEDO-Oper index value drops below -0.75 and the local minimum point needs to be determined.
- When local minimum values are reached, a tornado is likely to occur after the tendency to move to the neutral phase. For instance, as can be seen in the event of January 09, 2022, there were three local minimum attempts toward neutral phase. There have been reports of tornadoes in other provinces that were not included in the sample list in related dates.

Moreover, one of the challenges for the study was the temporal resolution of analysis data. Although interpolating analysis data seems like a solution, 1-hour forecast data, which is preferred for ecologic models in operational use today, will be more useful to follow the EMEDO index.

Another limitation was that the narrow presence of photos of tornadic storms in media. Although the tornado events that have been analyzed are the ones that have taken place in the last years and have photographs, as much as possible, more photographs are needed to understand the structure of the tornado. It would be beneficial to determine whether they are mesocyclonic or not. This is because, although too many small and harmless (non-mesocyclonic) waterspouts have been reported, the tornado events reported within the scope of this study are considered independent of mesocyclonic features. The reason for this is that the development process of each frontal or convective precipitation system should be examined through radar/satellite data tracking and whether the storm structure is mesocyclonic or not. Sometimes these meteorological systems intensify as they approach Turkey and can take on a supercellular structure. As stated in Study's purpose of shedding light, the EMEDO index can be a guide, however, these systems should be analyzed by modeling them operationally with high resolution for the limited period determined by EMEDO.

The further research step would be using EMEDO_i to detect an ULL that is expected to influence Turkey. According to the researches, it is argued that polar arctic or Icelandic cold strikes will affect Eastern Europe more frequently as a result of the widening of high pressure belts around subtropics within the scope of climate change. According to the researches made by some articles, in parallel, the Azores high pressure center gaining a more stable and vertically moving structure to become AR and BLO+ through the high latitudes in the north. This may make the indicators of EMEDO negative phases more frequent in the future. If it would be delved deeper into the subject by utilizing Weather Research and Forecasting Model (WRF), which is one of the prominent models on mesoscale numerical weather prediction, the major aspects of numerically simulating a tornado and its formation might be reviewed. In this way, the dynamics of tornado formation and structure based on both observations and laboratory and numerical weather prediction modeling experiments could be described in detail.

These storms contain secondary circulation and front inclination with the advection in the cold front transition should be thoroughly examined. In this way, it is possible to predict the convective trigger mechanisms and weather phases and ultimately have a forecasting approach for them. Besides, vertical layers should be resolved and elaborately modeled to obtain the features of thunderstorms such as storm motion speed/direction, critical angle, convection energy and relative winds. These opportunities contribute to geospatial point-based tornado forecasts however operating the model of high-resolution numerical weather prediction computational costs very huge amount for the institutes and national weather services. Consequently, there is a need to examine severe weather events in the Eastern Mediterranean region, including Turkiye and to reveal the clues that the events will take place a few days in advance. At this point, there is a necessity for a new index showing that the Mediterranean atmospheric conditions expected to influence the Eastern will trigger the formation of severe convective storms.

Besides, a more convincing relationship analysis could be improved in the near future, using the point reporting of the tornado events and the probability of triggering negative EMEDO index. At this point, Brier scores can provide information about how accurate a forecast was because a brier score is a way to verify the accuracy of a probability forecast. A forecast probability can refer to a specific event, such as there is a 25% probability of it occurs a tornado in the next 24 hours. In addition to that, Brier Skill Score also can be considered as a follow-up analysis. Although this index is not only considered within the scope of tornadic storms, but also it is estimated that it can be used for most extreme weather events (blizzards, hailstorms, wind damages, and so forth). In particular, institutions may have the opportunity to examine in more detail with the help of this index in terms of hailstorms, snowstorms or any other severe weather events affecting Turkiye all the year round.

To sum up, the thesis discussed how the ULL transport conditions into the Eastern Mediterranean are influenced in associated with lower and upper level geopotential height changes over the Euro-Mediterranean sector. The findings may contribute to studies for numerical weather prediction modeling in terms of low-level moisture, instability, lifting trigger mechanism and wind shear transport sensitivity into the Euro-Mediterranean, and its relation with the tornadic storm activities over the Eastern Mediterranean region.



REFERENCES

- Ahrens, C.D.** (2001) *Essentials of Meteorology: An Invitation to the Atmosphere*. Thomson Brooks/Cole, CA, USA.
- AON** (2020) *Weather, Climate & Catastrophe Insight. 2021 Annual Report*. AON.
- Bernatz R.** (2021) | Luther College. https://www.faculty.luther.edu/~bernatzr/Courses/Sci123/comet/radar/severe_signatures/
- Bluestein, H. B.** 1993: *Observations and Theory of Weather Systems. Vol. 2, Synoptic-Dynamic Meteorology in Midlatitudes*. Oxford University Press, 608 pp.
- Bluestein, H. B.** (2013). Severe convective storms and tornadoes. *Springer*, 10, 978-3.
- Cassou, C.** (2008). Intraseasonal interaction between the Madden–Julian oscillation and the North Atlantic Oscillation. *Nature*, 455(7212), 523-527.
- Cassou, C.** (2010). Euro-Atlantic regimes and their teleconnections. In *Proceedings: ECMWF Seminar on Predictability in the European and Atlantic regions* (pp. 6-9).
- CNRS.** (2021). *Europe's climate in 2050* [Video]. Youtube. www.youtube.com/watch?v=n9Ej5E47TNI
- Cook, A. R., & Schaefer, J. T.** (2008). *The relation of El Niño–Southern Oscillation (ENSO) to winter tornado outbreaks*. *Monthly Weather Review*, 136(8), 3121-3137.
- Commonwealth of Australia, Bureau of Meteorology.** (n.d.). [*Determining Thunderstorm Classification*]. Luther College. http://www.faculty.luther.edu/~bernatzr/Courses/Sci123/comet/radar/severe_signatures/navmenu.php_printname_print_midlevel_mesocyclone.htm_page_2.0.0.htm
- Davies, J. M.** (1993). *Hourly helicity, instability, and EHI in forecasting supercell tornadoes*. In *Preprints, 17th Conf. on Severe Local Storms*, St. Louis, MO, 1993 (pp. 107-111). Amer. Meteor. Soc.
- Doswell, C. A.** (2001). Severe convective storms—An overview. *Severe convective storms*, 1-26.
- Doswell III, C. A.** (2007). Small sample size and data quality issues illustrated using tornado occurrence data. *E-Journal of Severe Storms Meteorology*, 2(5), 1-16.
- Edwards, Roger** (2006). *The Online Tornado FAQ*. Storm Prediction Center, National Oceanic and Atmospheric Administration.
- ESTOFEX.** (n.d.) Vertical wind shear and convective modes. https://www.estofex.org/guide/1_4_5.html

- ESWD.** (2021). *European Severe Weather Database*. <https://www.essl.org/cms/severe-weather-season-2019-summary/>
- ESWD.** (2022). *European Severe Weather Database*. <https://eswd.eu/cgi-bin/eswd.cgi>
- Fujita, T. T.** (1971). Proposed characterization of tornadoes and hurricanes by area and intensity (No. NASA-CR-125545).
- Goulet, L.** (2015). Bow Echoes: Conceptual Schemes and European Relevance. The European Forecaster, URL <http://www.euroforecaster.org/newsletter20/meteofr2>.
- Groenemeijer, P., & Kühne, T.** (2014). A climatology of tornadoes in Europe: Results from the European Severe Weather Database. *Monthly Weather Review*, 142(12), 4775-4790.
- Hart, J.A., and W. Korotky.** 1991: *The SHARP workstation v1.50 users guide*. National Weather Service, NOAA, US. Dept. of Commerce, 30 pp. [Available from NWS Eastern Region Headquarters, 630 Johnson Ave., Bohemia, NY 11716.]
- Howard, B. C.** (2015). How Tornadoes Form and Why They're so Unpredictable. National Geographic News. National Geographic.
- Huth, J. E.** (2013). *The lost art of finding our way*. Harvard University Press.
- IPCC, 2021:** *Climate Change 2021: The Physical Science Basis*. Contribution of Working Group I to the Sixth Assessment Report of the Intergovernmental Panel on Climate Change [Masson-Delmotte, V., P. Zhai, A. Pirani, S.L. Connors, C. Péan, S. Berger, N. Caud, Y. Chen, L. Goldfarb, M.I. Gomis, M. Huang, K. Leitzell, E. Lonnoy, J.B.R. Matthews, T.K. Maycock, T. Waterfield, O. Yelekçi, R. Yu, and B. Zhou (eds.)]. Cambridge University Press, Cambridge, United Kingdom and New York, NY, USA, In press, doi:10.1017/9781009157896.
- Kahraman, A., & Markowski, P. M.** (2014). Tornado climatology of Türkiye. *Monthly Weather Review*, 142(6), 2345-2352.
- Kahraman, A., Kadioglu, M., & Markowski, P. M.** (2017). Severe convective storm environments in Türkiye. *Monthly Weather Review*, 145(12), 4711-4725.
- Kahraman, A., Ural, D., & Önoğ, B.** (2020). Future changes in Euro-Mediterranean daytime severe thunderstorm environments based on an RCP8.5 Med-CORDEX simulation. *Atmosphere*, 11(8), 822.
- Kahraman, A.** (2021). Synoptic climatology of supercell-type tornado and very large hail days in Türkiye. *Weather*, 76(4), 129-134.
- Krider, E. Philip** (2020, October 29). thunderstorm. Encyclopedia Britannica. <https://www.britannica.com/science/thunderstorm>
- Lackmann, G.** (2011). *Midlatitude synoptic meteorology*. American Meteorological Society.
- Lin, Y. L.** (2007). *Mesoscale dynamics* (Vol. 630). Cambridge: Cambridge University Press.

- Markowski, P., & Richardson, Y.** (2011). *Mesoscale meteorology in midlatitudes* (Vol. 2). John Wiley & Sons.
- Mentes, S.** (2020). Atmospheric Fronts and Idealized Cyclone Model [PowerPoint slides]. Istanbul Technical University.
- NOAA.** (2021, November 12) Air Masses | U.S. Department of Commerce, https://www.noaa.gov/jetstream/synoptic_intro/air-masses
- Orf, L., Wilhelmson, R., Lee, B., Finley, C., & Houston, A.** (2017). Evolution of a long-track violent tornado within a simulated supercell. *Bulletin of the American Meteorological Society*, 98(1), 45-68.
- Pennsylvania State University.** (n.d.). Cold Fronts. METEO 3, *Introductory Meteorology* Retrieved October 19, 2021, from https://www.e-education.psu.edu/meteo3/17_p5.html
- Pučík, T., Groenemeiger, P., & Tsonevsky, I.** (2021). *Vertical wind shear and convective storms*. European Centre for Medium-Range Weather Forecasts.
- Rasmussen, E. N., & Blanchard, D. O.** (1998). A baseline climatology of sounding-derived supercell and tornado forecast parameters. *Weather and forecasting*, 13(4), 1148-1164.
- Schumacher, R. S., & Rasmussen, K. L.** (2020). The formation, character and changing nature of mesoscale convective systems. *Nature Reviews Earth & Environment*, 1(6), 300-314.
- Steenburgh, J.** (n.d.). QG Theory and Applications: Synoptic–Dynamic Meteorology [PowerPoint presentation]. University of Utah. https://www.inscc.utah.edu/~steenburgh/classes/5110/lecture_notes/Q-vectors.pdf
- Storm Prediction Center.** (2009). Enhanced F Scale for Tornado Damage. <https://www.spc.noaa.gov/efscale/ef-scale.html>
- Storm Prediction Center.** (2021). Storm Prediction Center WCM Data. <https://www.spc.noaa.gov/wcm/data/>
- Stull, R.** (2015). Practical Meteorology: An Algebra-based Survey of Atmospheric Science. *The University of British Columbia Vancouver, Canada*.
- Sutter, D.** (2017, May 03). Tornadoes are costly, even when they don't occur. <https://altoday.com/archives/16653-daniel-sutter-tornadoes-costly-even-dont-occur>
- Thompson, R. L., Edwards, R., & Hart, J. A.** (2002). J3. 2 Evaluation and Interpretation of the Supercell Composite and Significant Tornado Parameters at the Storm Prediction Center.
- Thompson, R. L., Edwards, R., & Mead, C. M.** (2004, October). An update to the supercell composite and significant tornado parameters. In Preprints, 22nd Conf. on Severe Local Storms, Hyannis, MA, Amer. Meteor. Soc. P (Vol. 8).
- Grieser, J., & Haines, P.** (2020). Tornado risk climatology in Europe. *Atmosphere*, 11(7), 768.

- Walters Sr, K. R., Vojtesak, M. J., Martin, K. P., Myles, G., & Gilford, M. T.** (1991). SWANEA (Southwest Asia-Northeast Africa) A Climatological Study. Volume 3. The Near East Mountains. Air Force Environmental Technical Applications Center Scott AFB IL.
- Watch Chris Chase** (2019, October 25) *How to Read Weather Radar* [Video]. Youtube. <https://youtube.com/watch?v=AeX2IMUfddQ>
- WeatherX.** (2022). A tornado forecast by Cassandra Forecasting Model valid for August 3, 2022, 11:00 UTC. WeatherX Dashboard. Medium of publication ("Web"). Date of access (3 Aug 2022). <<https://weatherx.de>>.
- Weingart, J. [Twister Hunter].** (2016, September 21) *The Anatomy of the Life of a Supercell* [Video]. Youtube. www.youtube.com/watch?v=7W_s32dDgHY
- WMO** (2021). Atlas of Mortality and Economic Losses from Weather, Climate and Water Extremes (1970–2019) (WMO-No. 1267)

APPENDICES

Appendix A: Photos of Tornado Events in Table 2.3

Appendix B: Plots of a Hailstorm Event over Istanbul with Similar Methods

Appendix C: Alternative Synoptic Climatology Map of Tornadoes for Europe



Appendix A



Figure A. 1 : 17.01.2016



Figure A. 2 : 03.03.2016



Figure A. 3 : 13.11.2017



Figure A. 4 : 21.11.2018



Figure A. 5 : 24.01.2019



Figure A. 6 : 26.01.2019



Figure A. 7 : 08.10.2020



Figure A. 8 : 07.12.2021



Figure A. 9 : 19.12.2021



Figure A. 10 : 07.11.2022



Figure A. 11 : 15.10.2022



Figure A. 12 : 19.04.2022

Appendix B

Table B. 1 : Selected hail event in Turkiye and its features (ESWD, 2021) .

| Date | Time (UTC) | Latitude/ Longitude | Intensity | Path Length (km) | Path Width (m) | Funnel Cloud | Area | Province |
|------------|------------|---------------------|-----------|------------------|----------------|--------------|-----------|----------|
| 27.07.2017 | 14:55 | 41.01 N, 28.95 E | 8cm | \$600M | 10+ | yes | Bosphorus | Istanbul |

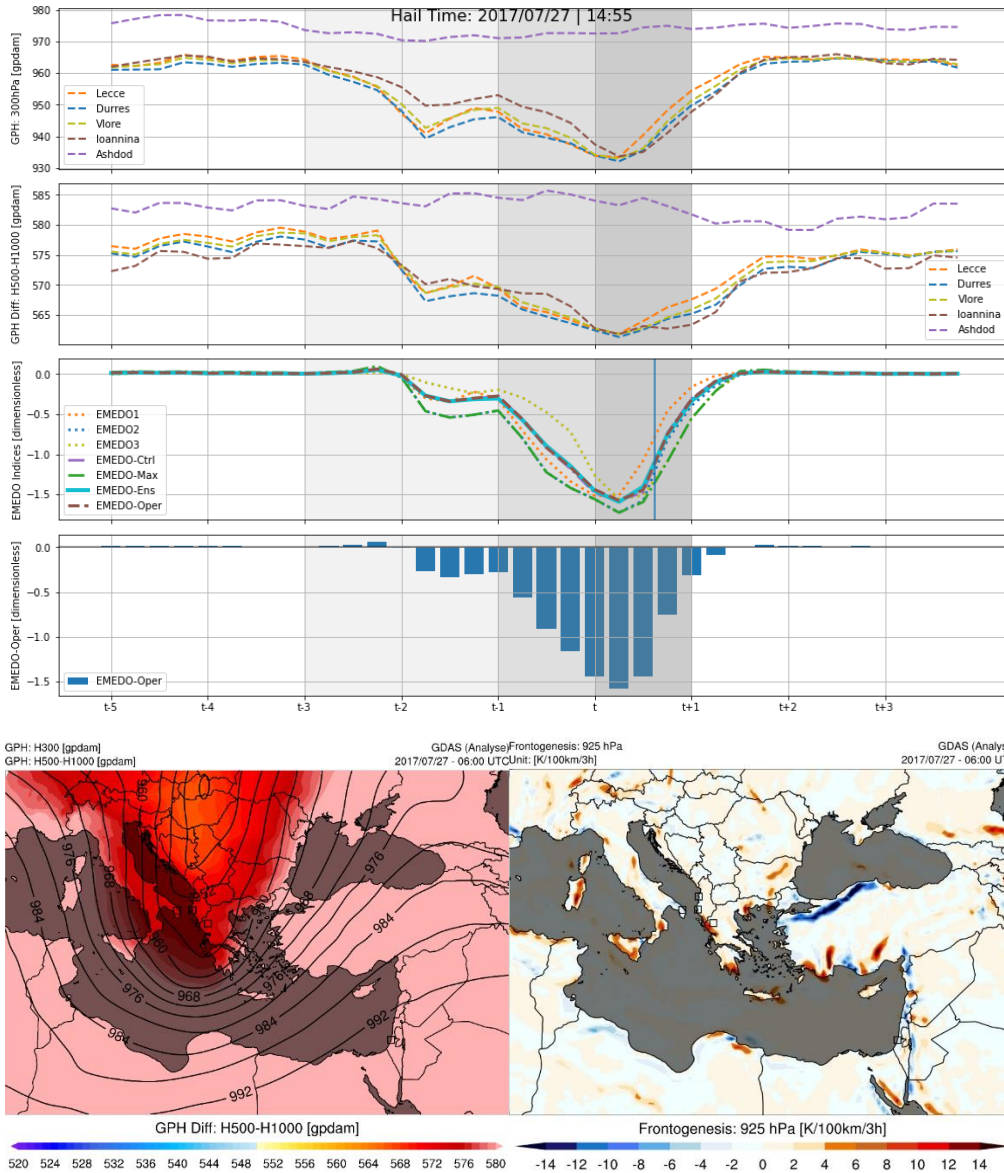


Figure B. 1 : Geopotential height [gpdam] at 300 hPa (isohypses) and geopotential height [gpdam] difference between 500hPa and 1000hPa (shaded color contours) 27.07.2017 – 12 UTC

Appendix C

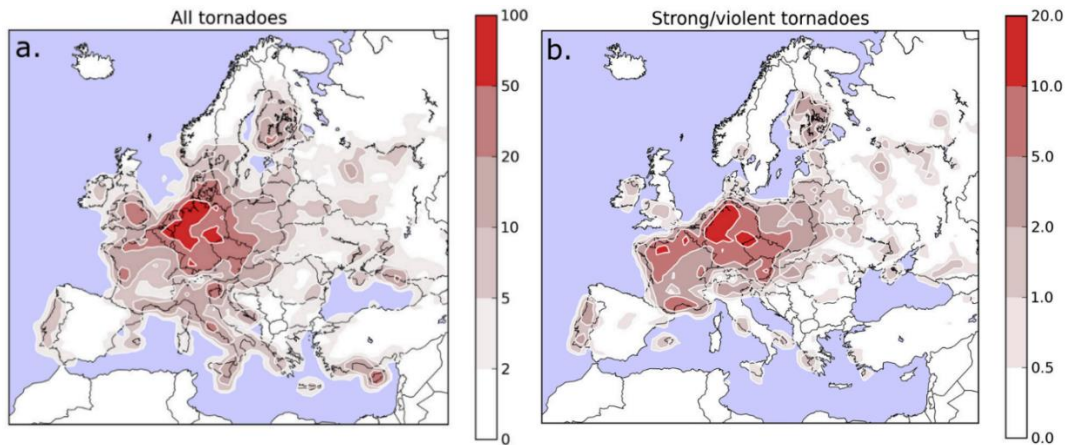


Figure C. 1 : Number of tornado events and (b) strong–violent (F2 and stronger) tornado events per 10000 km². The density was computed by dividing the number of events within (a) 100 and (b) 200 km of a point by the surface area of a circle with the respective radius (Groenemeijer & Kühne, 2014).



CURRICULUM VITAE

Name Surname : Ömer Kutay MIHLIARDIÇ

EDUCATION :

- **B.Sc.** : 2019, Istanbul Technical University, Faculty of Aeronautics and Astronautics, Meteorological Engineering
- **M.Sc.** : 2022, Istanbul Technical University, Graduate School, Atmospheric Sciences

PROFESSIONAL EXPERIENCE:

- 2021-2022, Project assistant | Institute of Meteorology und Climatology, Leibniz University Hannover
- 2019-2020, Co-Founder of an initiative “Experimental Analysis and Prediction of Storms” | ITU Technopark Innovation Center
- 2017-2019, Intern Meteorologist | CNN Turk, Turkish State Meteorological Service, General Directorate of State Hydraulic Works

CERTIFICATES AND REWARDS:

- 2020, Backyard Meteorology, The Science of Weather | Department of Physics, Harvard University
- 2020, Wind Energy | Technical University of Denmark (DTU)
- 2020, Best Weather Forecaster | 1st place within the faculty competition at Istanbul Technical University
- 2019, High Honor Alumni | based on cumulative GPA among BSc graduates at Istanbul Technical University
- 2018, WRF-ARW Modelling | Faculty of Aeronautics and Astronautics, Istanbul Technical University
- 2017, Fundamentals of Numerical Weather Prediction, Limitations of High Resolution NWP Models, Climate Change and Extreme Weather, Severe Convective Weather, Instrumentation and Measurement of Wind, NWP Essentials: Physics of Precipitation and Clouds | Meted/UCAR (online)